SISSA
Scuola Internazionale Superiore di Studi Avanzati

Neuroscience Area – PhD course in

Neurobiology

The role of TMEM16B in odorant adaptation of mouse olfactory sensory neurons and the co-expression of TMEM16F and ACE2 in supporting cells of the human olfactory epithelium

Candidate:
Giorgia Guarneri

Advisors:
Prof. Anna Menini
Prof. Simone Pifferi

Academic Year 2020-2021

Scuola Internazionale di Studi Avanzati

Trieste



The role of TMEM16B in odorant adaptation of mouse olfactory sensory neurons and the co-expression of TMEM16F and ACE2 in supporting cells of the human olfactory epithelium

Thesis submitted for the degree of "Doctor Philosophiae"

Academic Year 2020/2021

CANDIDATE

Giorgia Guarneri

SUPERVISORS

Prof. Anna Menini

Prof. Simone Pifferi

Table of Contents

List of abbreviations 7
Abstract 10
1. Introduction 12
1.1 The sense of smell 12
1.2 The olfactory systems 13
1.3 Main olfactory epithelium 14
1.3.1. Olfactory sensory neurons 15
1.3.2. Supporting cells 18
1.3.3. Basal cells 19
1.3.4. Microvillous cells 19
1.3.5. Bowman's glands 20
1.4 Olfactory bulb and olfactory cortex 20
1.5 Vomeronasal organ 23
1.6 Olfactory transduction 24
1.6.1. Odorant receptors 26
1.6.2. G-protein 29
1.6.3. CNG channels 30
1.6.4. Calcium-activated chloride channels 31
1.6.5. Adaptation 32
1.7 TMEM16 gene family 36
1.7.1 TMEM16A 44
1.7.2 TMEM16B 45
1.8. SARS –CoV2 and olfactory system 47
1.8.1. Expression of SARS-CoV-2 entry genes in human and mice OE 49
1.8.2. Cellular mechanisms behind the loss of smell in COVID-19 patients 53
1.8.3. The role of TMEM16F in SARS-CoV-2 spike induced syncytia 58
2. Aims 60
3. Materials and Methods 61
3.1 Animals and ethical approval 62
3.2 Electro-olfactogram recordings 62
3.3 Preparation of acute slices of mouse olfactory epithelium 64

3.4 Electrophysiological recordings from OSNs and stimuli presentation 65
3.5 Data analysis 67
4. Results 68
4.1 TMEM16B mediates large transduction current and contribute to the OSN spontaneous activity 68
4.2 Odorant response in *Tmem16b* KO OSNs 73
4.3 Olfactory adaptation in WT and *Tmem16b* KO mice 76
5. Conclusions and discussion 81
5.1 Physiological role of TMEM16B in olfactory sensory neurons 81
5.2 The role of TMEM16B in olfactory adaptation 82
6. Manuscript under revision 85
6.1 Supporting cells of human olfactory epithelium co-express the lipid scramblase TMEM16F and ACE2 and may cause smell loss by SARS-CoV-2 Spike-induced syncytia. 85
7. References 119

List of abbreviations

ACIII: adenylate cyclase – type III

ACE2: angiotensin-converting enzyme 2

Am: Amygdala

ANO1: anoctamin 1 (see TMEM16A)

ANO2: anoctamin 2 (see TMEM16B)

AOB: accessory olfactory bulb

AON: anterior olfactory nucleus

AP: alarm pheromones

ATP: adenosine triphosphate

BG(s): Bowman's glands

CaCC(s): calcium activated chloride channel(s)

CaM: calmodulin

cAMP: cyclic adenosine monophosphate

CNG: cyclic nucleotide gated ion channel

CNGA2: Cyclic Nucleotide Gated Channel Subunit Alpha 2

CNGA4: Cyclic Nucleotide Gated Channel Subunit Alpha 4

CNGB1b: Cyclic nucleotide-gated channel subunit beta 1b

CO: carbon monoxide

COVID-19: coronavirus disease 2019

ENaC: amiloride-sensitive sodium channel

Ent: entorhinal cortex

EPL: external plexiform layer

GBC(s): global basal cell(s)

GCL: granule cell layer

GG: Grueneberg ganglion

GL: glomerular layer

cGMP: cyclic guanosine monophosphate

Golf and Gαolf: olfactory-specific guanosine triphosphate (GTP)-binding protein

GPCR(s): G-protein-coupled receptor(s)

HBC(s): horizontal basal cell(s)

IPL: internal plexiform layer

KO: knockout

MCL: mitral cell layer

MOE: main olfactory epithelium

MOB: main olfactory bulb

NC: nasal cavity

NCKX4: potassium-dependent Na+/Ca2+ exchanger 4

OB: olfactory bulb

OE: olfactory epithelium

OM: olfactory mucosa

OMP: olfactory marker protein

OR(s): odorant receptor(s)

OSN(s): olfactory sensory neuron(s)

OT: olfactory tubercle

PDE(s): phosphodiesterase(s)

PDE1C: Calcium/calmodulin-dependent 3',5'-cyclic nucleotide phosphodiesterase 1C

PDE4A: cAMP-specific 3',5'-cyclic phosphodiesterase 4A

Pir: Piriform cortex

PLC: phospholipase C

RE: respiratory epithelium

S: Spike protein

SARS-CoV-2 virus: severe acute respiratory syndrome coronavirus 2

SC(s): supporting cell(s)

SO: septal organ

TMEM16 family: transmembrane proteins with unknown function 16

TMEM16A: calcium-activated chloride channel belonging to the TMEM16 family

TMEM16B: calcium-activated chloride channel belonging to the TMEM16 family

TMEM16F: calcium-activated scramblase and ion channel belonging to the TMEM16 family

TMPRSS2: transmembrane protease, serine 2

VNO: vomeronasal organ

Abstract

The sense of smell is one of the five main senses and represents for humans and for animals an incredible source of information, enabling them to locate food, mating partners and to avoid eating toxic substances. The detection of odorants starts with their binding to receptors on olfactory sensory neurons (OSNs), located in the olfactory epithelium in the nasal cavity. The OSNs are bipolar neurons presenting a round soma, an unbranched axon that projects to the olfactory bulb and a single dendrite ending with a knob from which immotile cilia protrude. Cilia contain the molecular elements for olfactory transduction. The binding of an odorant molecule to specific odorant receptors (ORs) triggers a transduction cascade that converts the chemical signal into an electrical one that is sent and processed by the central nervous system. The olfactory transduction cascade is mediated by the activation of adenylyl cyclase III that produces cAMP that in turn activates the cyclic nucleotide-gated (CNG) channels. Both Na^+ and Ca^{2+} enter the cilia through CNG channels and the increase of Ca^{2+} activates the Cl^- channel TMEM16B providing an amplification of the primary CNG current response.

In the first part of this thesis we investigated the role of TMEM16B in odorant-induced adaptation in OSNs using electrophysiological methods and a loss of function approach. We confirmed that TMEM16B is responsible for the amplification of CNG-mediated current and for controlling the spontaneous OSN firing frequency. Surprisingly, using electro-olfactograms (EOGs), we found that the odorant-induced response is bigger in *Tmem16b* knock-out (KO) than in wild-type (WT) mice. Moreover, the lack of *Tmem16b* alters the kinetics of the response with a faster rising phase and shorter recovery time. Using a double pulse protocol, we found that the recovery from odorant-induced adaptation is faster in *Tmem16b* KO than in WT mice. We also found that the exposure to an adapting odor pulse fails to shift the dose-response curve in *Tmem16b* KO. Moreover, we used the loose-patch configuration to record from individual OSNs. By measuring the odorant-induced action potential firing using a double pulse protocol, we determined that OSNs from *Tmem16b* KO mice recover from adaptation faster than those from WT mice, confirming that TMEM16B plays a role in adaptation.

In the second part of this work, we performed immunohistochemistry on the human olfactory epithelium obtained from biopsies performed at the Section of Otolaryngology of the Department of Medical, Surgical and Health Science of the University of Trieste to investigate possible effects induced by the virus SARS-CoV-2 on the olfactory epithelium. Indeed, at the beginning of 2020 the new SARS-CoV-2 virus spread over the world generating the Coronavirus disease 2019 (COVID-19). Since the first months of the pandemic it was clear that infected people developed chemosensory disorders that sometimes were the only symptom.

The SARS-CoV-2 virus can enter the cells through the interaction between the Spike protein on the virus capsid and the ACE2 receptor located on the surface of the target cells. Syncytia were formed in the lungs of patients who died after COVID-19. During the infection the cells that express SARS-CoV-2 Spike protein can form syncytia (characterized by a large cytoplasm containing multiple nuclei) with other cells that express ACE2 receptors and the calcium-dependent ion channel and scramblase TMEM16F has been proposed to be involved in syncytia formation. In this work we investigated whether the molecular machinery for generation of syncytia is expressed in cells of the human olfactory epithelium. We performed immunohistochemistry in nasal tissue from human biopsies and analyzed a single cell RNAseq dataset from human nasal epithelium. We found that ACE2 and TMEM16F are expressed in human supporting cells but not in OSNs. We discuss possible interaction between SARS-CoV-2 Spike protein and ACE2 producing the activation of TMEM16F leading to the possible formation of syncytia in the human olfactory epithelium.

1. Introduction

1.1 The sense of smell

Chemosensation, the detection of chemicals in the environment, is fundamental for the survival of the individual and more broadly of the species (Mombaerts, 2004a). The processing of peripheral chemosensory cues permits to locate food, conspecifics, predators and mating partners. Chemosensory systems are distinguished from the other senses by the qualitative heterogeneity of the stimuli that can be detected (Mombaerts, 2004b). In mammals, three chemosensory sensory systems, the olfactory, taste and trigeminal systems are dedicated to chemosensation.

The taste system detects tastants, molecules which provide information about the quality, quantity and safety of food and come into contact with the mouth while the trigeminal chemosensory system allows the detection of irritating or noxious molecules that come into contact with skin or mucous membranes of nose, mouth and eyes.

The olfactory system detects airborne molecules called odorants. In general, detected odors can give highly faithful and informative representation of the environment and odor detection can strongly influence feeding behaviors, social interactions and reproduction.

Odor perception is initiated with the detection of odorant molecules by the main olfactory epithelium (MOE) situated in the nasal cavity (Ma, 2007). In rodents there are two major olfactory apparatuses in the nasal cavity: the main olfactory epithelium (MOE) and the vomeronasal organ (VNO). The MOE is considered a detector for general odors and the VNO is mostly associated with the detection of social cues (such as pheromones). The nasal cavity also includes two segregated clusters of neurons forming the septal organ of Masera and the Grueneberg ganglion. The septal organ of Masera is involved in the detection of pheromones and is located in the basal region of the septal bone and in the anterior part of the main olfactory epithelium (Giannetti *et al.*, 1995; Munger, Leinders-Zufall and Zufall, 2009). The Grueneberg ganglion comprises neurons that are sensitive to cold temperature and play an important role in the detection of alarm pheromones

(AP) and is located in the rostro dorsal part of the nasal cavity (Brechbühl, Moine and Broillet, 2013; Figure 1).

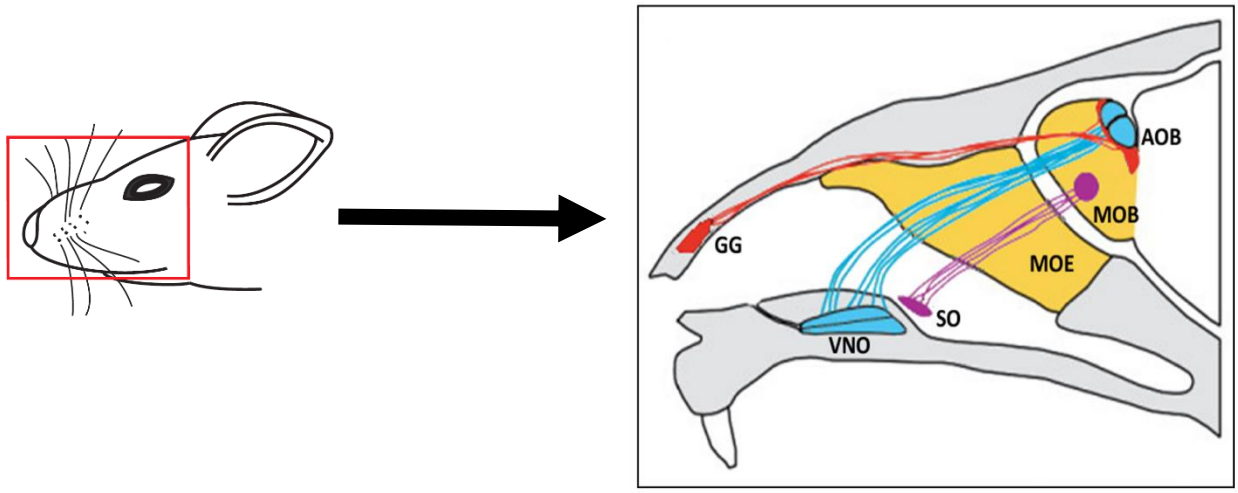


Figure 1: Olfactory systems.
Sagittal view of the mouse nose shows the localization of the multiple subsystems of olfactory system: main olfactory epithelium (MOE), the vomeronasal organ (VNO), the Grueneberg ganglion (GG), and the septal organ (SO). Odorants enter the nasal cavity and reach the MOE or the VNO. Sensory neurons of the MOE, SO and GG project to the main olfactory bulb (MOB) and the sensory neurons of the VNO project to the accessory olfactory bulb (AOB) (Modified from Munger *et al.,* 2009 and Ferrero and Liberles, 2010).

1.2 The olfactory systems

The olfactory system is the most studied component of the chemosensory triad and the most "ancient" sensory system. It processes the information about the identity, the concentration and quality of thousands of volatile chemicals commonly associated with the sense of smell. The odorants dissolved in the air enter the nasal cavity during the breathing cycle and can be detected by the different organs that compose the olfactory system (Wachowiak, 2011; Mainland *et al.*, 2014). The olfactory system includes the MOE, the main olfactory bulb (MOB) and the higher olfactory centers that receive direct or indirect information from the main olfactory epithelium. The odorants are detected by the OSNs located in the olfactory epithelium (Munger, Leinders-Zufall and Zufall, 2009).

1.3 Main olfactory epithelium

In rodents the nasal cavity has two main functions related to both the respiratory and olfactory system. It is responsible for heating, humidifying, filtering and correctly directing the inspired air. Rodents, unlike other species, can only breathe through the nose and this is due to an intimate opposition between the epiglottis and soft palate (Alvites *et al.*, 2018). The nasal cavity however also permits odorants to reach the OSNs. The nasal cavity is covered by different types of epithelia. The squamous epithelium is stratified with abundant hair follicles and is localized in the nasal vestibule. The transitional epithelium is a cuboid or columnar epithelium with no hair follicles and is located between squamous and respiratory epithelium primarily in the nasal valve. The respiratory epithelium covers more than 45 % of the nasal cavity surface and consists of ciliated columnar cells, goblet cells secreting mucus and basal stem cells. The olfactory epithelium and the underlying lamina propria form the olfactory mucosa (OM). The OM contains the specialized sensory organ for the detection of odorants (Chen *et al.*, 2014). From an histologically point of view the OM is characterized by the presence of Bowman's glands, OSNs and a pseudostratified columnar epithelium with twice the thickness of the respiratory epithelium (Alvites *et al.*, 2018).

The MOE is a columnar pseudostratified neuroepithelium localized in the upper regions of the nasal cavity lining the cartilaginous turbinates and septum (Ma, 2007). The nasal cavity extends from the nostrils to the nasopharynx and is divided into two identical and symmetrical chambers by the nasal septum (Figure 2A). The nasopharynx represents the airway posterior to the termination of the nasal septum and close to the termination of the soft palate. The principal difference among animals regarding the MOE is the percentage of the nasal airway that is covered by OE. In rodents, the nasal airway represents the higher percentage of the cavity covered by OE when compared to monkeys or humans (Harkema, Carey and Wagner, 2006).
The MOE includes four types of cells: OSNs, sustentacular cells, basal cells and microvillous cells. In physiological conditions the MOE contains both mature and immature OSNs (Chen *et al.*, 2014). The basal cells are divided into globose basal cells (GBCs) and horizontal basal cells (HBCs) depending on their localization, shape and function (Graziadei, 1973). The cell bodies of these different type of cells are organized in separate layers as shown in the Figure 2B.

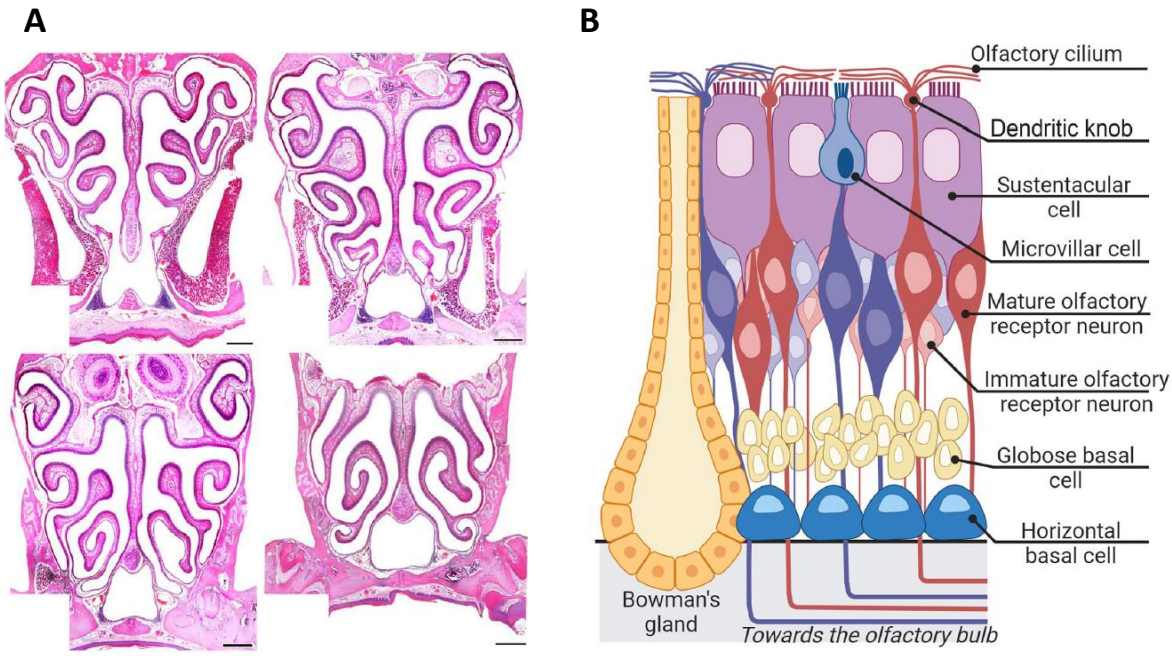


Figure 2: Histological organization of olfactory epithelium.
A: Coronal section of the mouse nasal cavity stained with haematoxylin-eosin at four levels along the anterior-posterior axis Scale bars: 500µm (from Barrios *et al*., 2014). B: Schematic diagram showing different cell types present in the olfactory epithelium (from Dibattista *et al*., 2021).

1.3.1. Olfactory sensory neurons

The OSNs are the most abundant cell type in the OE. They detect odorants present in the air and send projections to the central nervous system to transfer the chemosensory information from the surrounding environment.

The cell bodies of OSNs are located in the central layer of the OE. Anatomically, the OSN is a bipolar cell with a small soma, an unmyelinated axon and a single apical dendrite terminating in multiple cilia (Schild and Restrepo, 1998; Figure 3). The axons of OSNs form a set of intraepithelial bundles, going through the basal lamina and then associate in large fascicles at the level of the cribriform plate and terminating in the olfactory bulb (OB).

The apical surface of OSNs terminates with an enlargement called knob (diameter 2-3 µm) from which several cilia, called olfactory cilia, extend into a thick layer of mucus produced by Bowman's glands (Pifferi, Menini and Kurahashi, 2010). Mouse cilia are immotile (due to the lack

of dynein) and longer compared to the cilia present in the respiratory epithelium (RE) (Alvites *et al.*, 2018). The number of cilia can vary approximately in a range between 5 and 40 (Morrison and Costanzo, 1990; Schild and Restrepo, 1998). The mucus in the apical region is essential for solubilizing the odorants before the contact with the cilia and ensures the ionic gradients fundamental to sustain the transduction currents (Kleene, 2008). The cilia are the site of odor transduction. At the level of the cilia in fact, odorant receptors (ORs), enzymes and ion channels are used to detect and transduce the presence of odorants in the airflow.

In mouse OSNs, the cilia increase the knob surface approximately 40 times thanks to their peculiar geometry (diameter of a cilium is 100-250 nm and the length is in the range between 5 and 250 µm) facilitating the collision with the odorants (Menco and Jackson, 1997; Schild and Restrepo, 1998; Kleene, 2008).

The olfactory system can discriminate and recognize a large number of odorants because each OSN expresses only one of hundreds of distinct OR-type receptors (see 1.6.1). The expression of specific chemosensory receptor, enzymes and ion channels define the different subpopulation of OSNs.

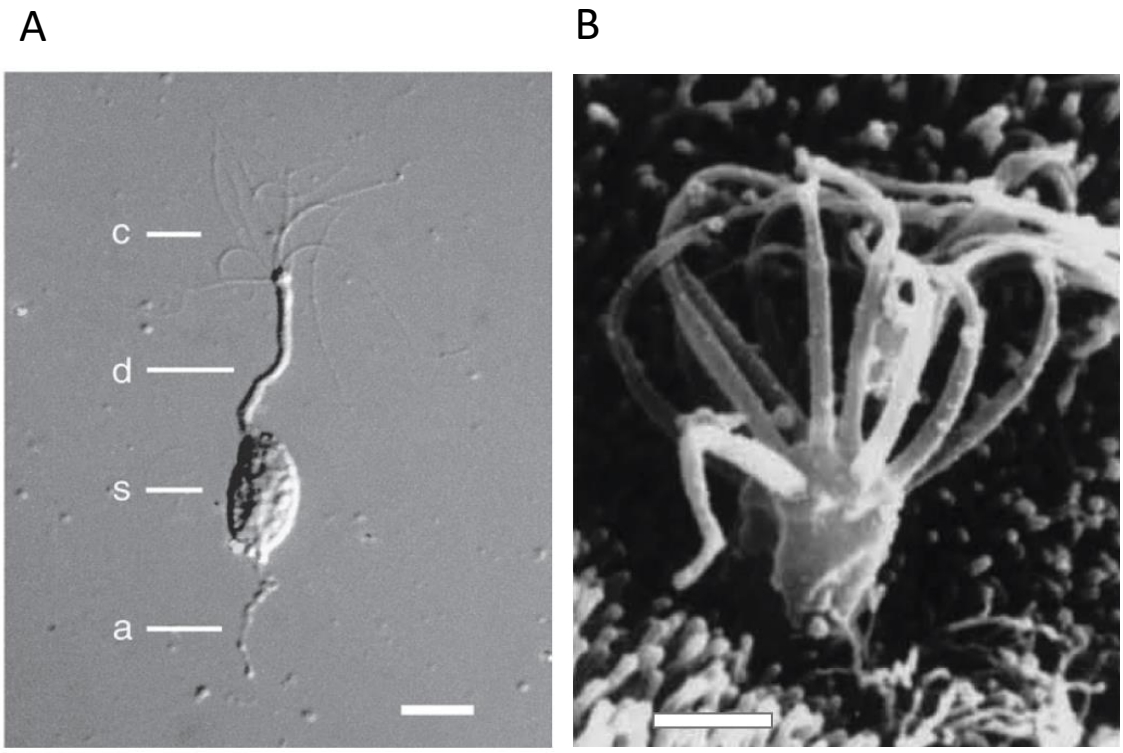


Figure 3. Olfactory sensory neurons.

A: Photograph under phase contrast optics of an isolated frog OSN. The OSN consists of a soma (s), an axon (a) and a dendrite (d) with a knob from which several cilia (c) protrude (scale bar: 10 µm, image from Kleen, 2008). B: Image obtained by scanning electron microscope of human OE. A dendritic knob with several cilia can be observed (scale bar: 1 µm, image from Morrison and Costanzo, 1990).

1.3.1.1. Passive electrical properties of olfactory sensory neurons

OSNs in mice are characterized by a high resting membrane resistance (>1 GΩ), thus the opening of a single channel inducies a small depolarizing current that can be sufficient to trigger the generation of action potentials (Lynch and Barry, 1989). The resting membrane potentials in mouse OSNs has been measured with different techniques. Maue and Dionne (1987) in cell attached mode estimated a membrane potential in the range from -30 to -80 mV with a mean of -52 ± 17 mV. *Ma et al.*, (1999) in perforated patch technique found a mean value of -55.0 ± 3.5 mV and Lagostena and Menini (2003) in whole-cell configuration measured a value ranging from -45 to -90 mV, with a mean value of -55.4 ± 3.6 mV. Given the high input resistance of OSNs, the

measured membrane resting potentials are probably underestimated and the real resting potential is closer to more negative values between -70 and -90 mV.

1.3.2. Supporting cells

The supporting cells (SCs) are non-neuronal cells, with both epithelial and glial-like function. SCs present an elongated shape that occupies the entire thickness of OE from the surface to the basal lamina. SCs preserve the integrity of the epithelium and provide mechanical and metabolic support to OSNs (Breipohl, Laugwitz and Bornfeld, 1974; Suzuki, Takeda and Farbman, 1996). SCs are also involved in secretion, endocytosis and metabolism of toxicants (Dahl, 1988; Bannister and Dodson, 1992). The apical surface of these cells is covered by long microvilli, which extend into the mucus layer where they intermingle with olfactory cilia (Menco and Morrison, 2003). SCs can influence the chemical interactions between odors and ORs and maintain the water and salt balance (Menco *et al.*, 1998). Interestingly, they express the amiloride-sensitive sodium channel (ENaC) in the microvilli and aquaporin-3 on the lateral membranes (Menco *et al.*, 1998; Menco and Morrison, 2003). SCs play also a role in physiological phagocytosis. Electron micrographs demonstrated that SCs contained apoptotic bodies, cellular debris and phagosome in their cytoplasm (Suzuki, Takeda and Farbman, 1996). The SCs are connected with the OSN through desmosomes (Menco and Morrison, 2003) and among themselves through gap junctions (Rash *et al.*, 2005; Vogalis, Hegg and Lucero, 2005).

1.3.3. Basal cells

The basal cells can be divided into two types, HBCs and GBCs. The human basal cells have a diameter of 4-7 µm and have a round soma (Menco and Morrison, 2003). They are responsible for the regeneration of OSNs during all the lifespan of the animal (Graziadei and Graziadei, 1979). The process of neurogenesis regularly regenerates the entire OSN population, also in humans (Hahn *et al.*, 2005). The HBCs are located near the basal lamina and contain keratins. The HBC are the reserve stem cells activated upon tissue damage (Leung, Coulombe and Reed, 2007). The GBCs are smaller, located above the HBCs, do not contain keratin and their cytoplasm is more electron lucent. The GBCs are primarily responsible for regenerating OSNs during normal epithelial turnover. In rodents, GBCs have a high turnover rate and can be replaced by the HBCs (Schwob *et al.*, 2016).

1.3.4. Microvillous cells

Microvillous cell are a minor cell population in the olfactory epithelium. Microvillous cells were described for the first time by Moran *et al*., (1982) and represent a different population, morphologically distinct, of chemoreceptor cells in the olfactory mucosa. Montani and colleagues (2006) suggest that microvillous cells are involved in coordinating cell death and regeneration of OSNs. Still today the role of the microvillous cells has not yet been definitively elucidated. The apical part of these cells presents short microvilli that project into the mucus layer lining the nasal cavity. The basal part has a cytoplasmic process that seems like an axon that travels from the epithelium toward the lamina propria. The cell body of these cells contains bundles of microfilaments, mitochondria, smooth endoplasmic reticulum, a Golgi complex, free ribosome and occasional cisternae of the rough endoplasmic reticulum (Jafek, 1982; Escada, Lima and Da Silva, 2009).

1.3.5. Bowman's glands

The Bowman's glands (BGs) are present in the olfactory mucosa of the majority of vertebrates (fishes excluded). The BGs are composed of serous and stem cells and in humans have a diameter of 20-40 µm (Menco and Morrison, 2003). The ducts of the BGs cross the basal lamina and the MOE and reach the luminal surface. The central lumen of these glands is surrounded by serous cells, with spherical nucleus and short stubby microvilli. The myoepithelial cells surround the acini and contain actin filaments. The Bowman's glands are tasked together with the SCs (especially in low vertebrates) to create the microenvironment necessary for sensory transduction. The ionic composition of the mucus produced by BGs and by SCs confers the correct ionic gradients necessary for the transduction currents involved in odor detection (Harkema *et al*., 2006). The mucus layer is important for the olfactory acuity, when the mucus layer becomes thicker, as during a cold, it decreases significantly the OSNs ability to response to odorant stimulation. The mucus acts also as a filter for the inhaled air, the odorants that enter the nasal cavity during the breathing cycle must be solubilized in the mucus before reaching the cilia of OSNs (Menco and Morrison, 2003).

1.4 Olfactory bulb and olfactory cortex

The olfactory bulb is the first portion of the brain involved in processing of odor information (Munger, Leinders-Zufall and Zufall, 2009). In mice, the OB is localized above the cribriform plate anteriorly to the frontal lobe of the brain. Axons of the MOE pass through pores in the cribriform plate and innervate the OB. The OB is organized into multiple layers, with different types of neurons found in each layer. Based on the layer in which their cell bodies are located the neurons in the olfactory bulb are categorized into juxtaglomerular (JG) cells in the glomerular layer, tufted cells in the external plexiform layer, mitral cells in the mitral cell layer and granule cells in the granule cell layer. The JG cells include three morphologically distinct cell types, the periglomerular (PG) cells, external tufted (ET) cells, and superficial short-axon (sSA) cells (Figure 4; Nagayama, Homma and Imamura, 2014).

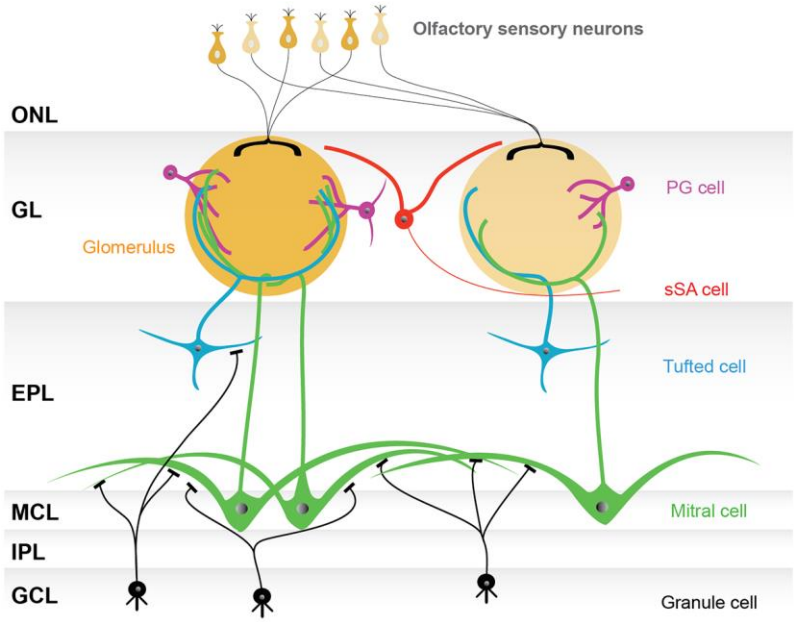


Figure 4: Olfactory bulb network. OSNs that express the same OR are randomly distributed in one of the four zones of the OE but their axons coalesce into the same glomeruli in the OB. Within a glomerulus, OSN axons make synapses with the dendrites of mitral or tufted cells which project their axons to the olfactory cortex (GL: glomerular layer, EPL: external plexiform layer, MCL: mitral cell layer, IPL: internal plexiform layer, GCL: granule cell layer (image from Nagayama, Homma and Imamura, 2014).

Axon of OSNs that express the same OR gene project and merge in GL to form a medial and a lateral glomerulus, generating two mirror image maps within each olfactory bulb (Mombaerts *et al.*, 1996). The axonal convergence to glomeruli was determined by Vassar *et al*., (1993) in rat and by Ressler *et al.,* (1993) in mouse through RNA in situ hybridization and finally demonstrated using genetic-based neuronal tracing by Mombaerts *et al*., (1996). Bozza et collaborators (2002) demonstrated that the expression of a specific OR directs the formation of glomeruli from functionally similar olfactory afferents. They replaced the OR at a genetic locus with another OR gene and demonstrated that it changed OSN odorant responsiveness and shifts the localization of axonal convergence in the OB. They also demonstrated that a given OR imparts the same odorant selectivity when expressed in different epithelial zoned from distinct OR loci.

Glomeruli are the functional unit of the olfactory bulb, where OSN axon terminals make synaptic contacts with the dendrites of second order neurons. Odorants elicit distributed and

reproducible spatiotemporal patterns of glomerular activation (Imai, 2014). A single glomerulus integrates afferent signals and sends odor information into the deeper layers to mitral and tufted cells (Mombaerts *et al.*, 1996).

All the glomeruli are not wired simultaneously but emerge over a period of a few days perinatally, and once formed are maintained during the lifespan to preserve the olfactory perception and the glomerular organization (Mombaerts, 2006). The combination of the converging axons of OSNs expressing the same OR to a glomerulus first and the synaptic integration at the level of mitral and tufted cells as the second step are important features in maximizing the discriminatory power of the olfactory system (Imai, 2014).

From the OB, the projecting neurons form the lateral olfactory tract and project to the primary olfactory cortex, the anterior olfactory nucleus (AON), the olfactory tubercle (OT), the piriform cortex (Pir) and the entorhinal cortex (Ent). The OB projects also to the limbic system, including the nucleus of the lateral olfactory tract, the anterior cortical nucleus and the posterolateral cortical nucleus of amygdala (Am), involved in the emotional aspects associated with odors (Haberly, 2001; Lledo, Gheusi and Vincent, 2005; Imai, 2014). The olfactory system also transmits the chemosensory information to the hypothalamus that mediates behaviors such as feeding, aggression and reproduction (Figure 5; Boehm, Zou and Buck, 2005; Mandiyan, Coats and Shah, 2005; Yoon, Enquist and Dulac, 2005; Wang *et al.*, 2006).

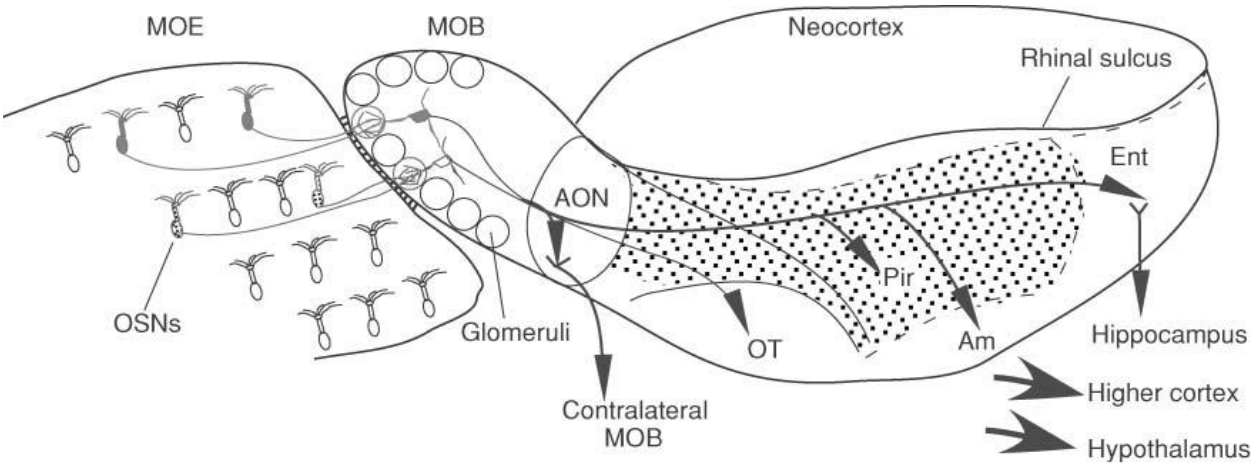


Figure 5: The main olfactory system and the brain.
The drawing of the rodent brain is rotated upward by 45° to offer the ventrolateral view. The second order neurons (mitral or tufted cells) sends their axons via the lateral olfactory tract and project to the anterior olfactory nucleus (AON), the olfactory tubercle (OT), the piriform cortex (Pir, dotted area) and entorhinal area (Ent). Olfactory information arrives to the higher cortex and to the hypothalamus (from Ma, 2007).

1.5 Vomeronasal organ

The vomeronasal organ (VNO) is a peripheral sensory organ of the accessory olfactory system present in the nasal cavity, at the base of the nasal septum, of many mammals (Meredith, 2001). The VNO is distinct from the nasal cavity in some amphibians, reptiles and non-primate mammals and is absent in marine mammals, bats, old world monkeys and great apes (Swaney and Keverne, 2009). The VNO is involved in the detection of pheromones, substances (do not belong to a specific chemical class) released by animals which trigger behavior and physiological changes of other individuals of the same species (Wyatt, 2014).

The vomeronasal organ is a bilateral tubular structure encapsulated by a protective layer of cartilage and located in the anterior part of the nasal cavity. The VNO has an elongated shape with a long central lumen full of fluids in direct contact with the nasal cavity or oral cavity. The VNO is composed by two epithelia, the non-sensory and the sensory epithelium. The non-sensory epithelium is composed by venous sinuses, smooth muscles and unmyelinated nerve fibers. The sensory epithelium is a crescent-shaped pseudostratified epithelium composed mainly by

vomeronasal sensory neurons (VSNs), SCs and basal cells. We can distinguish three regions in the neuroepithelium: the SCs and the dendrites of the VSNs are localized in the apical part close to the lumen, nuclei of SCs are found in a central region and soma of apical and basal VSNs are localized in a basal region (Mendoza, 1993).

VSNs are the main component of the vomeronasal sensory epithelium. In rodents, VSNs can be classified in apical and basal based on the location of their nuclei in the vomeronasal organ. The apical neurons are located near the luminal surface of the epithelium and express the G-protein αi2 subunit, PDE4A, and receptors of V1R or formyl peptide receptor family (Lau and Cherry, 2000). Basal neurons are located close to the basal lamina, express the G-protein αo subunit and receptors of V2R or formyl peptide receptor family (Berghard, Buck and Cy, 1996; Ryba and Tirindelli, 1997; Leinders-Zufall *et al.*, 2004; Mohrhardt *et al.*, 2018). VSNs are bipolar neurons that project an axon towards the accessory olfactory bulb where axon terminals form glomeruli, while towards the luminal side project a dendrite from which numerous microvilli protrude in the lumen. The microvilli are involved in the vomeronasal signal transduction, they take contact with pheromones embedded in the VNO's mucus. Ligand binding triggers the activation of the transduction machinery that activates a phospholipase C (PLC)-dependent second messenger transduction cascade that produces an increase in the intracellular calcium concentration and action potential firing (Mohrhardt *et al.*, 2018).

1.6 Olfactory transduction

The molecular machinery for olfactory transduction is localized in the cilia of OSNs. The interaction of odor molecules with ORs triggers a cascade of events that convert the chemical stimulus into an electrical one. ORs are members of the G-protein coupled receptors (GPCRs) family and trigger a transduction cascade mediated by $G\alpha_{olf}$ (Jones and Reed, 1989). The $G\alpha_{olf}$ subunit, activated in response to an odorant, detaches from Gβ and Gγ subunits and increases the activity of the adenylyl cyclase type III enzyme (ACIII) that converts adenosine triphosphate (ATP) into cyclic adenosine monophosphate (cAMP). Subsequently, cAMP binds to cyclic nucleotide-gated (CNG) channels inducing their opening and allowing cations (mainly Na^+ and

Ca^{2+}) to enter the ciliary lumen and depolarize the cell (Nakamura and Gold, 1987; Firestein, Zufall and Shepherd, 1991). The increased of levels of ciliary Ca^{2+} induced by the opening of CNG channel leads to the activation of Ca^{2+}-activated Cl^- channels (CaCCs) mediated by TMEM16B, inducing an outflow of chloride that enhances the depolarization of the cell (Boccaccio and Menini, 2007; Stephan *et al.*, 2009; Reisert and Zhao, 2011; Dibattista *et al.*, 2017; Figure 6). The depolarizing role of the Cl^- current through the TMEM16B channel is determined by the peculiar equilibrium potential of Cl^- (E_{Cl}). Reuter and colleagues (1998) performing energy dispersive X-ray micro analysis on cryosection of rat OE measured Cl^- concentrations of 69 mM inside the apical part of the OSN and 55 mM in the mucus, giving an equilibrium potential for Cl^- of + 6mV. Moreover, Nakamura and colleagues (1997) estimated the Cl^- concentration in the intact OE of mice and rats using 2 photon fluorescence lifetime imaging of the Cl^- sensitive dye MQAE. They found a maximal concentration of 70 mM within the dendritic knob decreasing to 50 mM along the dendrite in the presence of high extracellular Cl^- concentration. The Cl^- concentration in the mucus is maintained by $Na^+/Ca^{2+}/2Cl^-$ co-transporter NKCC1 and $Cl^-/HCO3^-$ exchanger SLC4A1 (Reisert *et al.*, 2005; Nickell, Kleene and Kleene, 2007; Hengl *et al.*, 2010).

The termination of the responses is regulated by the cleavage of cAMP mediated by a phosphodiesterase enzyme (PDE). Two distinct phosphodiesterase have been identified in mammalian OSNs: calcium/calmodulin dependent 3',5' cyclic nucleotide phosphodiesterase (PDE1C) and cAMP-specific 3',5'-cyclic phosphodiesterase 4A (PDE4A). PDE1C protein is mainly expressed in the cilia of OSNs and the PDE4A protein is expressed in the cell but is absent from the cilia (Yan *et al.*, 1995; Cygnar and Zhao, 2009). Cygnar and Zhao (2009) demonstrated that only the diffusion of cAMP from the cilia into the knob is sufficient to a rapid response termination suggesting the cooperation between these two PDE isoforms.

Another important player in the termination of the olfactory response is the decrease of the intracellular Ca^{2+} concentration. The closure kinetics of the CaCCs are determined by the rate of ciliary Ca^{2+} removal. Stephan and collaborators (2012) demonstrated that the K^+ dependent Na^+/Ca^{2+} exchanger 4 (NCKX4) expressed in the cilia of OSNs is fundamental for Ca^{2+} extrusion from ciliary lumen, controlling the termination of the odorant response. Also, Ca^{2+} buffering by

mitochondria in the dendritic knob are important for the clearance of Ca^{2+} during odorant stimulation (Fluegge *et al.*, 2012)

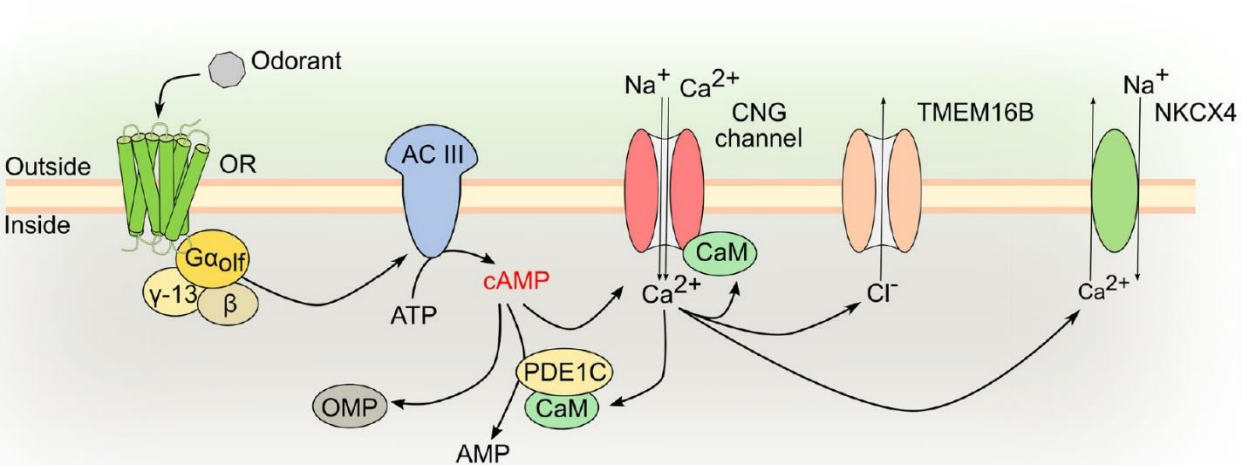


Figure 6: The olfactory transduction.
The olfactory transduction begins with odorant binding to a OR. After the binding of an odorant molecule the OR change conformation and induce the activation of the G-protein. $G\alpha_{olf}$ induces the enzymatic activity of adenylyl cyclase 3 (ACIII) leading to an increase in intraciliary levels of cAMP. cAMP opens CNG channel allowing the Na^+ and Ca^{2+} influx. These events are sufficient to depolarize the OSN. The increase Ca^{2+} concentration inside the cilia activates the Ca^{2+} activated Cl^- channel TMEM16B inducing an efflux of Cl^- inducing a further depolarization of the cell. The termination of the response is mediated by Ca^{2+} that binds calmodulin (CaM) reducing the sensitivity of CNG channels to cAMP and by the activity of the phosphodiesterase PDE1C. The Ca^{2+} is also extruded by the exchanger NKCX4 (modified from Boccaccio *et al.*, 2021).

1.6.1. Odorant receptors

The initial detection of odor stimuli is mediated by ORs. ORs are 7 transmembrane G-protein coupled receptors (GPCRs) characterized by an extracellular N-terminal and an intracellular C-terminal domains, three extracellular loops alternate with three intracellular loops to form the seven membrane spanning helices (Figure 7; Buck and Axel, 1991; Probst *et al.*, 1992)

OR genes share many characteristics with other GPCRs, for example a coding region lacking introns (Mombaerts, 1999), a structure with seven α-helical membrane spanning domains, and

many conserved short sequences (Pilpel and Lancet, 1999). However, ORs have certain specific characteristics, such as an unusually long second extracellular loop and an extra pair of conserved cysteines in this loop (Firestein, 2001).

ORs can recognize different odorants that vary in size, shape, functional groups and charge thanks to their extremely variability in their amino acid sequence. In the third, fourth and fifth transmembrane regions there is a hypervariability where the sequences show particularly strong divergence. This is the region that forms the ligand binding pocket for odorant molecules (Kini and Firestein, 2001; Menini, Lagostena and Boccaccio, 2004). Krautwurst and colleagues (1998) demonstrated that a single amino acid change in one transmembrane domain of an OR can alter its odorant specificity.

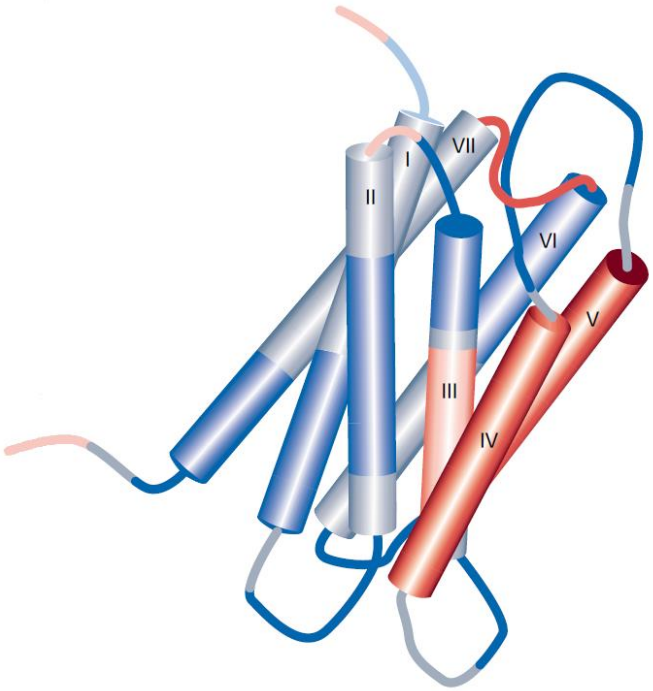


Figure 7: Odorant receptor.
A schematic view of the proposed three-dimensional structure of the odorant receptor. In this model the conserved regions are shows in blue and the variable regions are shows in red. The variable regions form the ligand binding region (from Firestein *et al*., 2001).

After the first cloning in 1991 in rats, nowadays more than 1000 functional ORs have been identified in mouse genome and around 400 In humans (Buck and Axel, 1991; Zhang and Firestein, 2002; Adipietro, Mainland and Matsunami, 2012). The genes encoding ORs can be classified as Class I (fish-like) and Class II (tetrapod-specific). Class I ORs are specific for recognizing water soluble odorants and Class II for the airborne odorants (Ronnett and Moon, 2002).

Only one OR is expressed in a single OSN (Mombaerts, 1999; Buck, 2000). OSNs present a monoallelic expression: only one of the two alleles of a specific OR is expressed (Chess *et al.*, 1994; Ishii *et al.*, 2001). Four spatially segregated zone of genes expression are present in the olfactory epithelium. In every zone OSNs that express the same OR are distributed randomly (Menini *et al*., 2004; Mombaerts, 2004a), moreover the OSNs that express a specific OR are exclusively present into one of the four zones of the OE (Ressler, Sullivan and Buck, 1993; Vassar, Ngai and Axel, 1993). Even if there are 1000 ORs, to detect the enormous range of odors a combinatorial strategy is necessary: most odor molecules are recognized by the activation of more than one receptor and most receptors are activated by several odors. One receptor can recognize different features of the odorants, in fact the recognition of an odorant molecule depends on which receptors are activated and to what extent (Figure 8; Malnic *et al.*, 1999; Buck, 2000; Firestein, 2001).

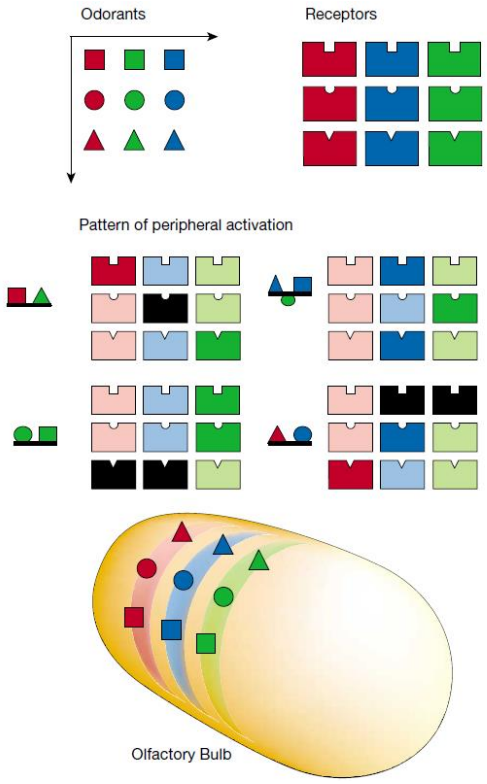


Figure 8: The combinatorial strategy of odorant discrimination.
The olfactory system can detect and discriminate among hundreds of thousands of odorants thanks to the combinatorial approach. One OR can be activated by different types of odorants and one odorant can activate at the same time different ORs (from Firestein, 2001).

1.6.2. G-protein

Biochemical and electrophysiological studies demonstrated that odorants generate responses in OSNs via an adenylyl cyclase cascade mediated by a G-protein (Menco *et al.*, 1992; Belluscio *et al.*, 1998). In OSNs two G_{α} isoform, G_s and G_{olf}, are able to activate adenylyl cyclase and contribute to odor-evoked signalling, but G_{olf} is the most abundant (Jones and Reed, 1989). Belluscio and colleagues (1998) demonstrate that mice lacking G_{olf} show a remarkable reduction in the electrophysiological response of the OSNs to different odorants. The mutant mice have also problems to feed and most of them die a few days after birth, the rare surviving homozygous mutant mice exhibit hyperactive locomotor behaviour. They demonstrated that the subunit G_{olf}

is required in olfactory sensory transduction and may function also in neurons in the central nervous system.

1.6.3. CNG channels

cAMP is the most important messenger in the initial phase of odorant detection. During the initial phase of response, the concentration of cAMP in the cilia increases. cAMP binds and opens the cyclic nucleotide-gated (CNG) channel and each CNG channel has four cAMP binding sites (Zheng and Zagotta, 2004). The binding of 2 cAMP molecules is necessary to open the channel and the binding of the second cAMP molecule leads the channel to its maximum open probability (Nache *et al.*, 2005). CNG channels are non-selective cation channels (Kaupp and Seifert, 2002). In OSNs, the opening of CNG channels causes an influx of Na^+ and Ca^{2+} inducing the depolarization of the neurons.

The olfactory CNG channels are tetramers and are composed by three types of subunits: CNGA2, CNGA4 and CNGB1b. The subunits of the CNG channel in OSNs surface membrane have a recurrent composition involving 2CNGA2: 1CNGA4: 1GNGB1b (Zheng and Zagotta, 2004). CNGA4 and CNGB1b are considered auxiliary subunit since when expressed alone they cannot form functional channels. They are mostly involved in conferring to the heteromeric channels a higher Ca^{2+} selectivity, higher sensitivity to cAMP and the negative regulation by Ca^{2+}-calmodulin (CaM) (Boccaccio, Menini and Pifferi, 2021).

Each CNG subunit has six transmembrane domains, with a pore-forming loop between the fifth and sixth domain, an intracellular N and C terminal regions, and a cyclic nucleotide-binding domain at the C terminus. These channels are mildly sensitive to membrane voltage (Kaupp and Seifert, 2002; Pifferi, Boccaccio and Menini, 2006).

The CNG channels are important for odor detection and for OSNs adaptation. Brunet and colleagues (1996) demonstrated using electro-olfactogram (EOG) recordings that CNGA2 knockout (KO) mice fail to respond to a wide variety of odor stimuli and have a small response to other. Mice without a functional CNG channel usually struggle to survive because they have

problems with feeding behavior during nursing and weaning. Furthermore, KO mice for CNGA4 or CNG1b present a different adaptation to odorants and a defective in trafficking of other CNG subunits to the cilia (Brunet, Gold and Ngai, 1996; Munger, 2001; Michalakis *et al.*, 2006). After their activation, these channels show a Ca^{2+}-dependent negative feedback mechanism that is important in mediating olfactory adaptation (Kurahashi and Menini, 1997; Ronnett and Moon, 2002).

Recent work suggests a possible role of olfactory marker protein (OMP) in the termination of the response, OMP works as a cAMP-buffer, is localized in the vicinity of CNG channels and controls the cAMP dynamics contributing to the odorant response kinetics (Nakashima *et al.*, 2020).

1.6.4. Calcium-activated chloride channels

The activation of the CNG channels increases the concentration of Ca^{2+} in the ciliary cytoplasm and opens the CaCCs (Kleene and Gesteland, 1991; Lowe and Gold, 1993). In rats, the CaCCs is 8 times more abundant than the CNG channel (Reisert *et al.*, 2003). Different studies, first in amphibia and then in mammals and fish demonstrated an unusually high intracellular Cl^- concentration in OSNs (Reuter *et al.*, 1998; Kaneko, Nakamura and Lindemann, 2001; Kaneko *et al.*, 2004; Hengl *et al.*, 2010). The high concentration of Cl^- present within OSNs makes the outflow of Cl^- an amplification step, accounting for up to 80 to 90 % of the odorant-induced depolarizing current (Kleene, 1997; Boccaccio and Menini, 2007; Stephan *et al.*, 2009; Li *et al.*, 2018).

It has been proposed that in amphibians CaCCs are important to preserve the olfactory transduction efficacy even in a variable extracellular ionic environment (the fresh water enters the nasal cavity and dilutes the nasal mucus). In fact, thanks to the presence of CaCCs both cationic and anionic currents are present in olfactory transduction (Kurahashi and Yau, 1993). When CaCCs were found also in rat OSNs, the hypothesis was that these channels have a role as an amplifier of olfactory transduction and allow the detection of very low odorant concentration (Lowe and Gold, 1993). In fact, the Cl^- efflux boosting the local depolarization increases the

chances to detect odor molecules even at low concentration and with few interactions on ORs (Frings, 2009; Li *et al.*, 2018).

The molecular identity of the CaCCs have been controversial for a long time. It is clear now that just two members of TMEM16 (anoctamin) gene family, TMEM16A and TMEM16B encode for CaCCs (Yang *et al.*, 2008; Pifferi, Dibattista and Menini, 2009; Stephan *et al.*, 2009). This was confirmed by studies in knockout animals which showed a reduction in CaCC activity (Rock and Harfe, 2008; Billig *et al.*, 2011).

1.6.5. Adaptation

The olfactory system can adjust its response allowing the cell to work over a broad range of stimuli intensities (Torre *et al.*, 1995). This modulatory process, defined as adaptation, is fundamental in order to guarantee the correct functioning of the olfactory system.

Adaptation prevents the saturation of the cellular transduction machinery and allows for high sensitivity during continuous or repetitive odor stimulation and is associated with a shift of the dose response curve to higher odorant concentrations compared with the control state. Adaptation is a type of neuronal plasticity, and it is time dependent and reversible (Reisert and Matthews, 1999). A typical protocol to investigate the adaptation is a double-pulse protocol. When a brief odor stimulus is repeated with a small interstimulus interval, an attenuated response is obtained during the second stimulation. The increase of the interstimulus interval (usually in seconds) permits the full recover of the amplitude associated to the second response (Figure 9).

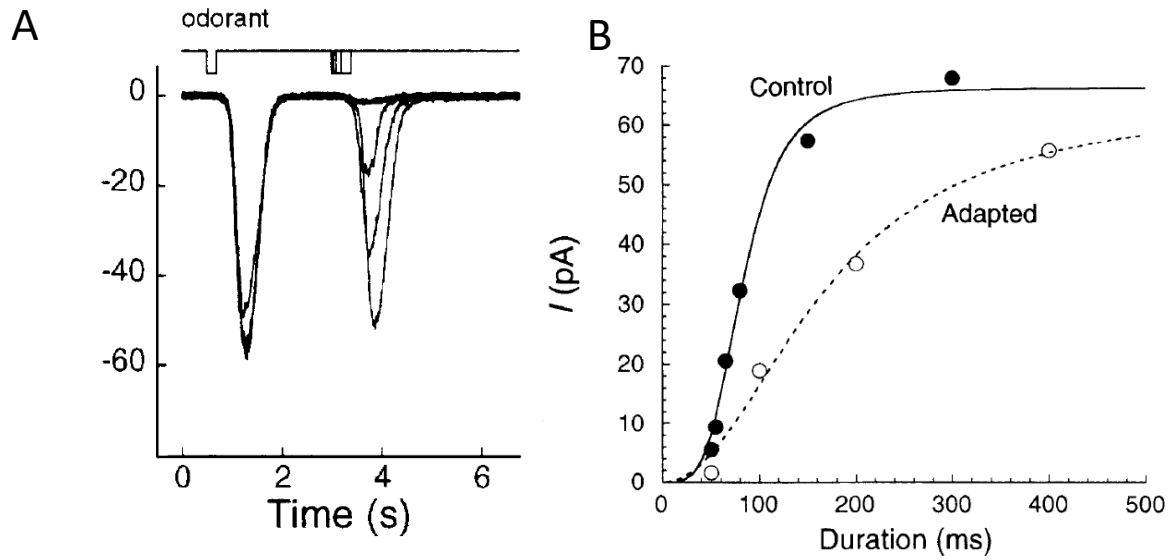


Figure 9: Odorant induced adaptation.

A: Whole-cell recording from a newt OSN stimulated with a double pulse protocol. The conditioning odorant pulse was kept constant while the second pulse (applied after 2.5 seconds) was changed in duration. In order to obtain a response with the same amplitude it was necessary to increase the duration of the stimulus. B: The amplitude of the response under control (filled circles) and adapted (open circles) conditions is plotted versus the duration of the interstimulus interval. The adaptation causes the shift of the dose response curve to higher odorant concentrations compared with the control state (From Kurahashi and Menini, 1997).

The mechanism of adaptation is strictly dependent on Ca^{2+} concentration in the cilia which works as a feedback signal. The adaptation mechanism can be abolished by reducing the intracellular Ca^{2+} concentration. Kurahashi and Menini (1997) demonstrated that Ca^{2+} inside the cell is responsible for the current reduction. When double pulse protocols are performed in a solution with low intracellular Ca^{2+} concentration the amplitude of the responses are overlapping. This adaptive mechanism can be recruited also by mimicking the odor response using the photolysis of caged cAMP. The use of caged cAMP permits to bypass the early stages of odorant transduction and to produce a rapid increase of cAMP concentration. This experiment strongly suggests that the principal mechanism for olfactory adaptation happens downstream of the adenylyl cyclase (Figure 10).

The elevated intracellular concentration of Ca^{2+} and the calcium binding protein calmodulin (CaM) reduces the sensitivity of the CNG channels to cAMP (Trudeau and Zagotta, 2003; Pifferi, Boccaccio and Menini, 2006; Song *et al.*, 2008; Reisert and Zhao, 2011).

The Ca^{2+}/CaM can bind the CNG channel on different sites. Two CaM-binding sites have been reported on the N and C terminal domains of auxiliary subunits CNGB1b and CNG4A respectively (Reisert and Zhao, 2011). Another target in CNGA2 subunit is represented by a basic amphiphilic alfa helix motif near the N terminus (Bradley, Reuter and Frings, 2001). Among all these CaM-binding domains, it has been shown that only the site in B1b and A4 are fundamental for Ca^{2+}/CaM- mediated adaptation (Bradley *et al.*, 2004; Song *et al.*, 2008).

Despite multiple experiments suggested the preponderant role of calcium concentration in the modulatory mechanism behind adaptation, the enhanced activity of the phosphodiesterase (PDE) has been questioned as a possible factor participating to this mechanism. An increased hydrolysis of cAMP in fact could achieve a similar result.

To investigate this possibility Boccaccio and colleagues (2006) performed double pulse experiments with caged 8-Br-cAMP, a compound that works as an agonist of the CNG channel resistant to PDE hydrolysis. In these experiments the reduction of the amplitude of the response after the second pulse has been confirmed indicating that the PDE1C does not play a relevant role in adaptation to a repetitive stimulus. Later, Cygnar and Zhao (2009) confirmed that cAMP degradation by PDE1C is not a rate limiting factor for the termination of the response. They showed that in KO mice for PDE1C the decay of the response was not prolonged and that a reduced sensitivity and reduced adaptation occurred after repeated stimulation.

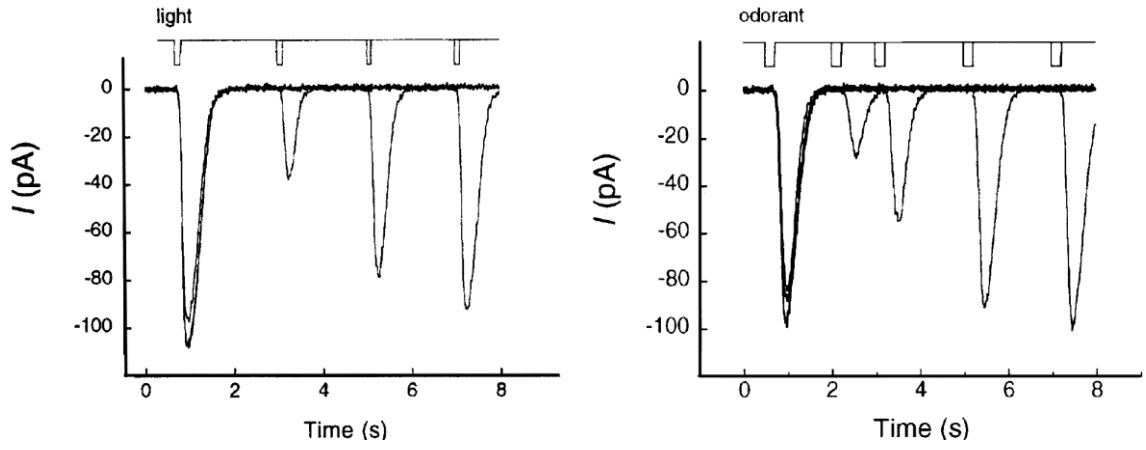


Figure 10: Mechanisms of odor-induced adaption.

The pattern of the response in experiments with photolysis of caged cAMP was very similar to the reduction measured with double odorant pulses. This result indicates that adaptation takes place after the production of cAMP (from Kurahashi and Menini, 1997).

The adaptation occurs also after a sustained odor pulse with a decline of the OSN response, a phenomenon called also desensitization. The desensitization is a Ca^{2+}-mediated process and similar to adaptation is strongly reduced by removing the Ca^{2+} in the internal solution (Zufall, Shepherd and Firestein, 1991). In a mouse model in which the CNGB1b subunits lacks the N-terminal CaM-binding domain a reduced response decline during prolonged odorant exposure has been measured. This suggests that Ca^{2+}/CaM desensitization of the CNG channel contributes also to the adaptation during a sustained odor pulse (Song *et al.*, 2008). The recovery from desensitization is slower compared to adaptation (occurring for brief pulse of odors), this suggest that the decrease of the ciliary Ca^{2+} signal alone is not sufficient for the recovery from desensitization. The desensitization is correlated with a rapid loss of responsiveness of GPCRs and caused by the uncoupling of receptors from heterotrimeric G-proteins in response to receptor phosphorylation, the internalization of cell surface receptors to the cytosol and a reduced protein synthesis of the receptor. The period of time for these processes ranges from seconds (for phosphorylation) to minutes (for the endocytosis) and hours (for the downregulation) (Kato and Touhara, 2009)

In olfactory sensory system we can find also long-lasting adaptation. This type of adaptation operates on the time scale of minutes and, at least in salamander OSNs was dependent on the carbon monoxide (CO)/cGMP second messenger system. The long-lasting adaptation is promoted by the release of CO that induces the stimulation of soluble guanylyl cyclase (sGC) and the subsequent cGMP formation. The long-lasting adaptation was completely abolished by inhibitors of CO synthesis (Zufall and Leinders-zufall, 1997; Zufall and Leinders-Zufall, 2000).

1.7 TMEM16 gene family

TMEM16 proteins are a family of “transmembrane proteins with unknown function 16”. This class of membrane proteins is only present in eukaryotic genomes and consists of 10 members, named with the letters from A to K (excluding I). These proteins are also name Anoctamin or Ano numbered from 1 to 10 (Figure 11) (Milenkovic *et al.*, 2010; Brunner *et al.*, 2014).

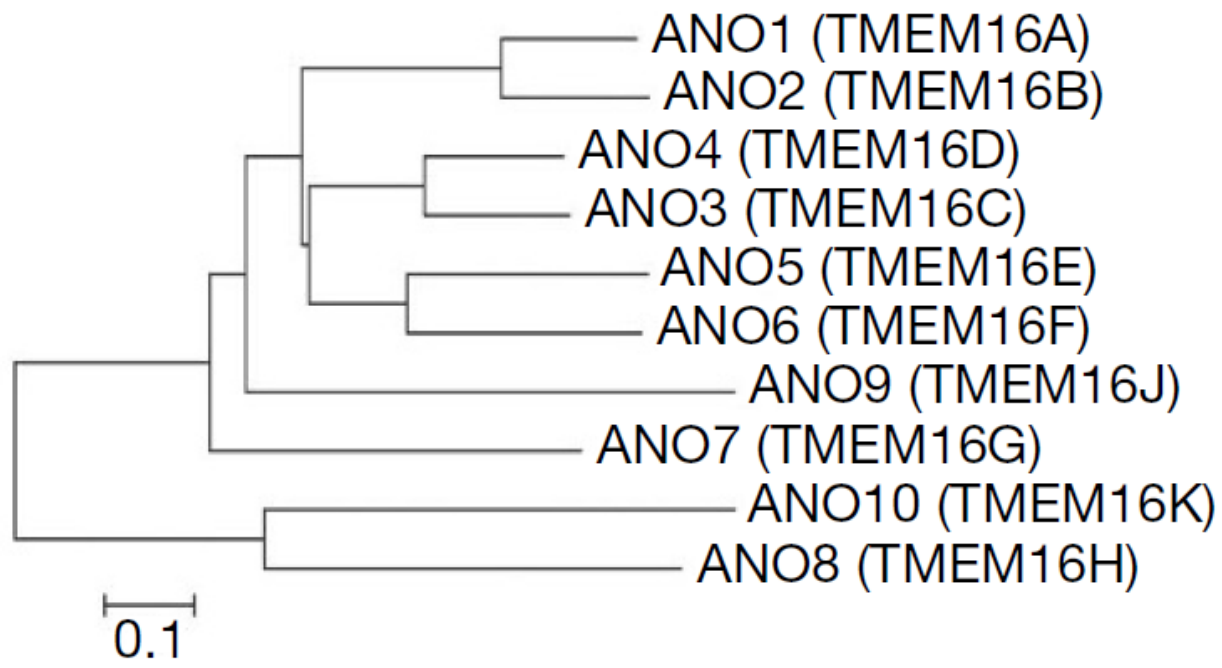


Figure 11: Anoctamin / TMEM16 protein family.
Phylogenetic tree representing the human Anoctamin- TMEM16 family. Scale bar, 0.1 nucleotide substitutions per site (from Yang *et al.*, 2008).

The name anoctamin was proposed because the first characterized TMEM16 protein, TMEM16A, is anion selective and bioinformatic analysis predicted that TMEM16A have eight transmembrane domains. However, in 2017 Paulino and colleagues through cryo-electron microscopy revealed a structure with ten transmembrane domains (Figure 12a) and not all these proteins are channels selective for anions (Hartzell *et al.*, 2009; Brunner *et al.*, 2014; Falzone *et al.*, 2018; Malvezzi *et al.*, 2018). For these reasons we prefer to refer to this protein family with the TMEM16 nomenclature.

In 2008, three different and independent laboratories reported that TMEM16A encoded for Calcium Activated Chloride Channels (CaCCs) (Caputo *et al.*, 2008; Schroeder *et al.*, 2008; Yang *et al.*, 2008). In the same year, Schroeder et al. and later other groups showed that also TMEM16B encoded for a CaCCs (Pifferi, Dibattista and Menini, 2009; Stephan *et al.*, 2009; Stöhr *et al.*, 2009). In 2010, Suzuki and colleagues demonstrated that TMEM16F encoded for a Ca^{2+}-dependent

scramblase, allowing the transport of phospholipids between the two-membrane leaflets along their electrochemical gradients. Proteins of the TMEM16 family share a conserved structure: they are homodimers with 10 transmembrane spanning helical domains connected by loop regions of different length and intracellular N and C terminals. The α helices and β strands of the amino-terminal domain are organized in a ferredoxin like fold. Each homodimer presents a hydrophilic cavity spanning the membrane. The shape of this cavity resembles an hourglass, with a small extracellular and a large intracellular vestibule bridged by a narrow neck region of about 20 Å long (Dang *et al.*, 2017; Paulino *et al.*, 2017). In this cavity the Ca^{2+}-binding site is localized, where each subunit can bind two Ca^{2+} ions (Brunner *et al.*, 2014). Paulino and colleagues showed that TMEM16A channels present two different structures in the presence or absence of Ca^{2+}. Ca^{2+} ions interact with the intracellular region in the transmembrane α helices 6 and transmembrane α helices 7 and activating the channel. In the absence of Ca^{2+} the lower part of transmembrane α helices 6 is pushed away from transmembrane α helices 7. The structures of the protein with Ca^{2+} bound and with Ca^{2+} unbound are very similar in the most part of the protein except for changes in the region close to the Ca^{2+}-binding sites (Figure 12).

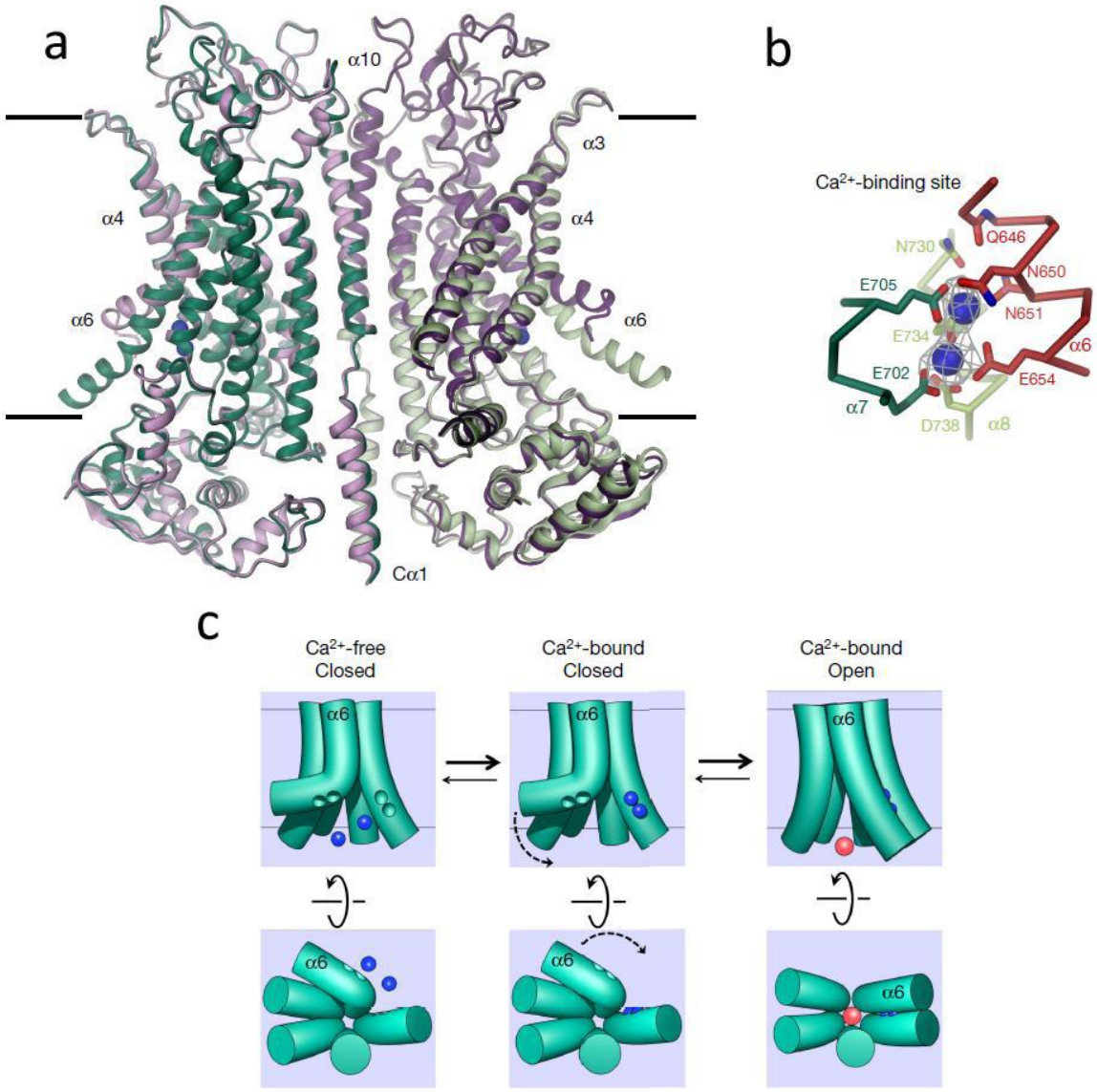


Figure 12: Structures and activation mechanism of the TMEM16A channel.

A: Ribbon representation of a superposition of the Ca^{2+} bound (green) and free Ca^{2+} free (violet) structures of mouse TMEM16A. The extracellular side is at the top of the image. B: Structure of the Ca^{2+} binding site with cryo-EM density of the two Ca^{2+} ions superimposed as a mesh. C: Schematic representation of the activation of TMEM16A. Top panels are viewed from within the membrane, bottom panels from the intracellular side. Green cylinders, pore-lining helices; blue spheres, calcium ions; red spheres, chloride ions (from Paulino *et al*., 2017).

TMEM16A and TMEM16B are close paralogues and they have 60% identity at the amino acid level. The most conserved regions are the transmembrane domain (70-90% overlapping) and the more divergent are the N- and C- termini (48% and 35% identity respectively) (Milenkovic *et al.*, 2010). Both TMEM16A and TMEM16B function as Ca^{2+}-activated Cl^- channels (Pedemonte and Galietta, 2014; Falzone *et al.*, 2018) and have similar biophysical properties, but TMEM16B channel is characterized by a 10-fold lower Ca^{2+} affinity. 300-600 nM range of cytosolic Ca^{2+} concentration can activate TMEM16A whereas TMEM16B channels required micromolar concentrations (Figure 13). Another difference is that TMEM16B Cl^- currents are characterized by activation and deactivation kinetics much faster than the one evoked from TMEM16A (Scudieri *et al.*, 2013).

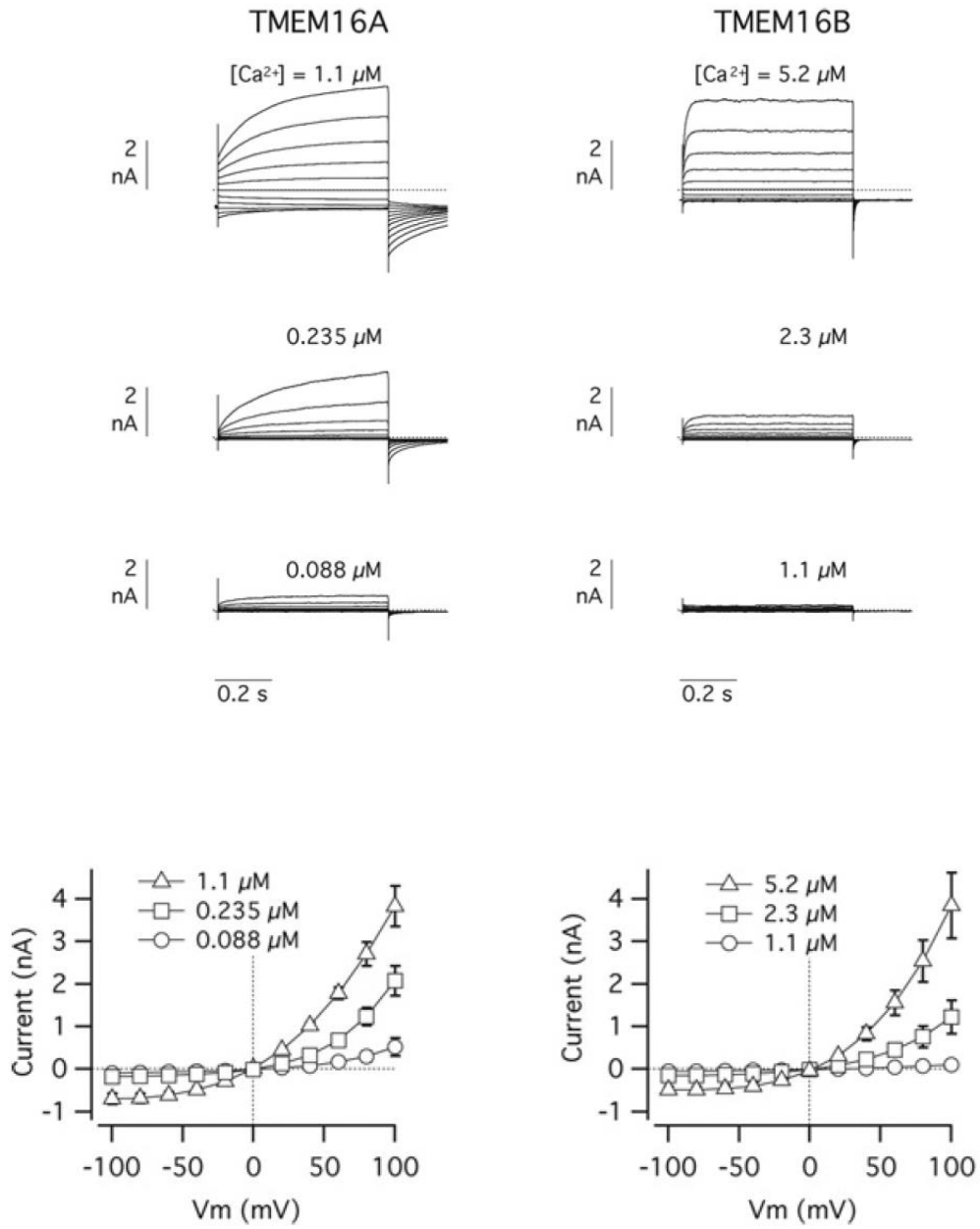


Figure 13: Properties of TMEM16A and TMEM16B as channels.

Representative whole-cell membrane currents recorded at different intracellular Ca^{2+} concentration in HEK cells transfected with TMEM16A and TMEM16B. The voltage steps protocols ranging from -100 mV to 100 mV with a holding potential of -60 mV (from Scudieri *et al.*, 2013).

TMEM16A and TMEM16B are gated both by voltage and intracellular Ca^{2+} concentration. The calcium sensitivity depends on the membrane voltage, the affinity for Ca^{2+} increases at higher values of the membrane potential (Huang, Wong and Jan, 2012; Pedemonte and Galietta, 2014). The current voltage relationship is linear at high intracellular calcium concentration and show outward rectification at low intracellular calcium concentration (Figure 14). TMEM16A is also activated in the absence of Ca^{2+} at high membrane voltage (Xiao *et al*., 2011).

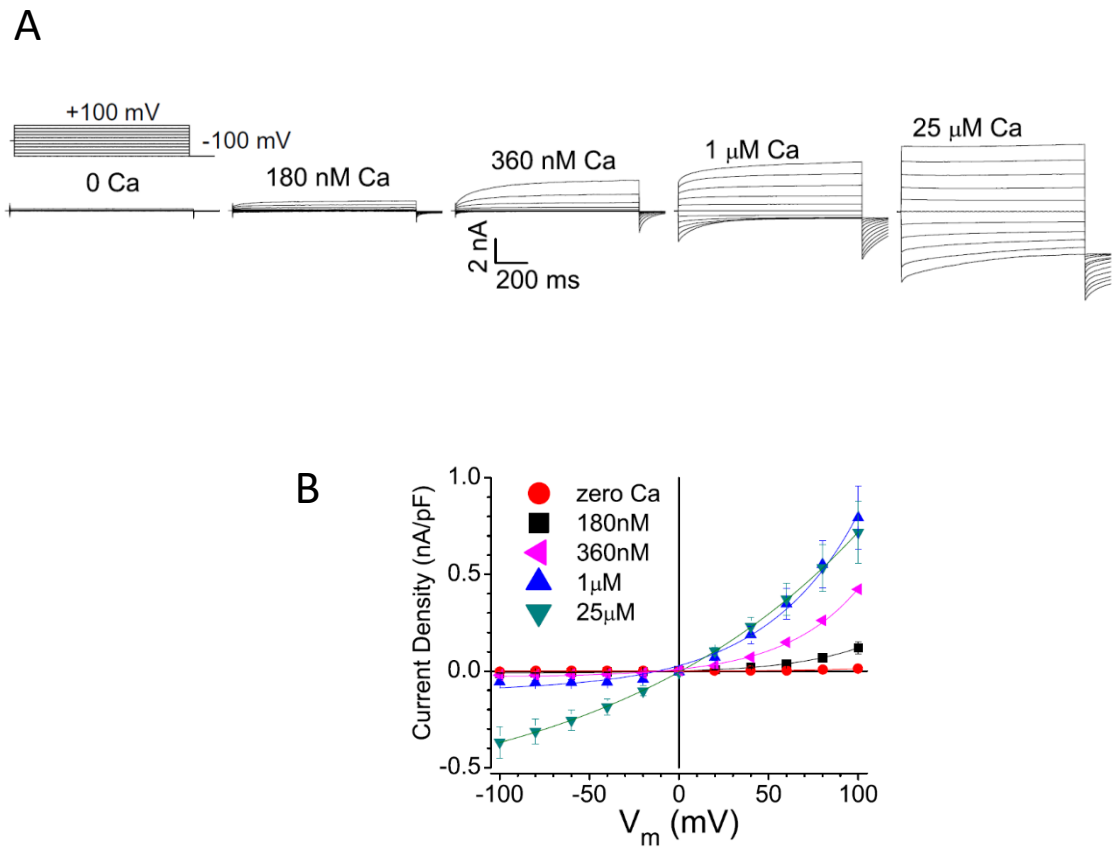


Figure 14: TMEM16A mediated currents are modulated by intracellular Ca^{2+} and membrane potential
A: Representative recordings from different HEK-293 cells transfected with mouse TMEM16A at different concentrations of free Ca^{2+}. B: The voltage steps protocol ranging from -100 to 100 mV with a holding potential of 0 mV elicited TMEM16A currents with different IV relationships in the presence of different amounts of free intracellular Ca^{2+} (from Xiao *et al*., 2011).

Both TMEM16A and TMEM16B have a very small single channel conductance around 3.5 pS for TMEM16A and near 1 pS for TMEM16B (Pifferi, Dibattista and Menini, 2009; Adomaviciene *et al.*, 2013) Other divalent cations such as Ba^{2+}, Sr^{2+}, and Ni^{2+} can activate TMEM16A and TMEM16B channels while Zn^{2+} has an inhibitory effect (Stephan *et al.*, 2009; Ni, Kuan and Chen, 2014). TMEM16A and TMEM16B are also permeable to large anions, their ion permeability follows the selective sequence: $SCN^- > I^- > NO_3^- > Br^- > Cl^- > F^-$ (Betto *et al.*, 2014; Pedemonte and Galietta, 2014).

Suzuki and colleagues (2010) first showed that TMEM16F encoded for a Ca^{2+}-dependent scramblase and subsequent studies indicated that also TMEM16C, D, E, G, H and J can mediate lipid scrambling (Suzuki *et al.*, 2013; Gyobu *et al.*, 2017; Di Zanni *et al.*, 2018; Boccaccio *et al.*, 2019). Among the TMEM16 channel/scramblase TMEM16F is one of the most highly expressed members in several tissues and cell types (Schreiber *et al.*, 2010; Falzone *et al.*, 2018). TMEM16F facilitates the exchange of phosphatidylserine from the inner to the outer leaflet of the membrane. In humans, TMEM16F mutations cause Scott syndrome, a defective Ca^{2+}-dependent exposure of phosphatidylserine in activated platelets (Suzuki *et al.*, 2010). Also in mice a deletion of TMEM16F induce a Scott syndrome phenotype (Baig *et al.*, 2016).

1.7.1 TMEM16A

TMEM16A is expressed in secretory cells, in smooth muscle cells and in the olfactory system, in particularly, in microvilli of vomeronasal sensory neurons (Huang *et al.*, 2009; Billig *et al.*, 2011; Dauner *et al.*, 2012; Dibattista *et al.*, 2012; Maurya and Menini, 2014).

Maurya and Menini (2014) followed the developmental distribution of the channel reporting the temporal and cellular expression of TMEM16A in the olfactory system. The channel is mainly expressed at E12.5 in the apical part of the olfactory epithelium and from E16.5 was found only in the region of the OE near the transition zone with the respiratory epithelium. In the respiratory epithelium TMEM16A is expressed in the microvilli of SCs indicating a regulatory role on the chloride ionic composition of the olfactory mucus (Figure 15; Maurya and Menini, 2014).

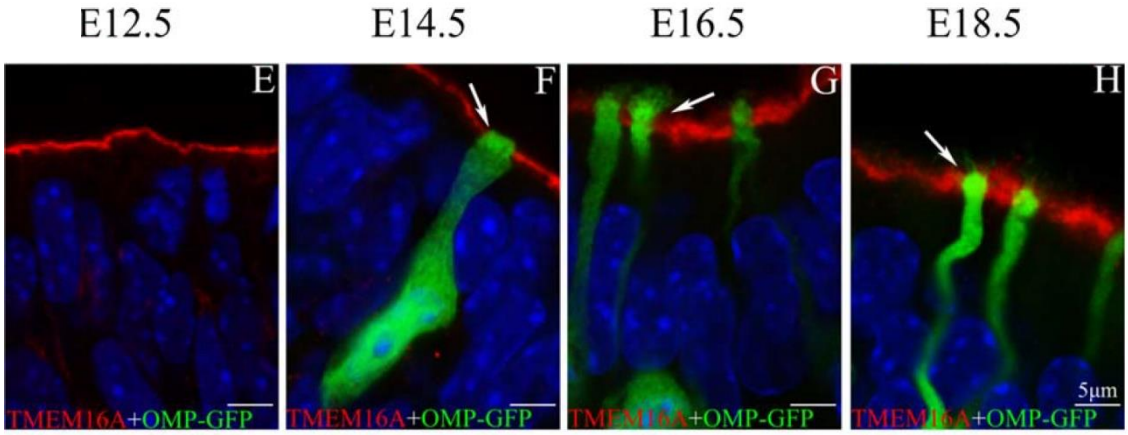


Figure 15: Expression of TMEM16A in the olfactory epithelium.
Confocal images of coronal sections of olfactory epithelium from OMP-GFP mice at E12.5, E14.5 E16.5 and E18.5 immunostained for TMEM16A (red). TMEM16A was expressed from E12.5 and is localized at the surface of OE in a different cell type from mature OSNs expressing OMP (from Maurya and Menini, 2013).

TMEM16A is involved in many physiological functions including neuronal signalling, smooth muscle contraction, airway and exocrine gland secretion, and rhythmic movements of the gastrointestinal system (Pedemonte and Galietta, 2014). *Tmem16a* KO mice mimics the cystic fibrosis disease phenotype: the animals show an accumulation of mucus and impairment of mucociliary transport in the airways (Pedemonte and Galietta, 2014).

1.7.2 TMEM16B

TMEM16B is expressed at the level of the synaptic terminals of photoreceptors of the mouse retina (Stöhr *et al.*, 2009; Dauner *et al.*, 2012), in dendrites of hippocampal pyramidal neurons (Huang *et al.*, 2012), in thalamocortical neurons (Ha *et al.*, 2016), and in many other neuronal cell types (Zhang *et al.*, 2017; Li *et al.*, 2019; Wang *et al.*, 2019). In the olfactory system it is expressed in the cilia of OSNs and in the microvilli of vomeronasal sensory neurons (Stöhr *et al.*, 2009; Billig *et al.*, 2011; Dauner *et al.*, 2012). In the olfactory system TMEM16B is expressed from embryonic

day 14.5 in the cilia of mature OSNs, indicating the involvement of these channel in olfactory transduction (Figure 16; Maurya and Menini, 2014).

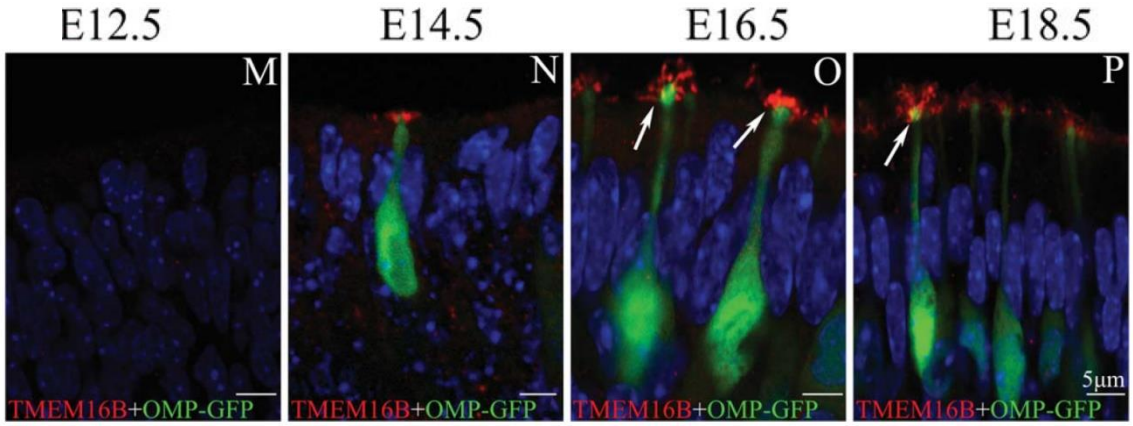


Figure 16: Expression of TMEM16B in the olfactory epithelium.
Confocal images of coronal sections of olfactory epithelium OMP-GFP mice at E12.5, E14.5 E16.5 and E18.5 immunostained for TMEM16B (red). TMEM16B was expressed from E14.5 in the cilia and knobs of mature OSNs (from Maurya and Menini, 2013).

TMEM16B expressed in OSNs presents two alternative splice variants at exon 4, generating TMEM16B variants either with or without exon 4. The exon 4 encodes a 33 amino acid segment within the cytoplasmic N terminus. The exon 4 sequence is required to form functional channels and the N terminal sequences affect Ca^{2+} sensitivity (Ponissery Saidu *et al.*, 2013). Billig and colleagues (2011) generated the first mouse model KO for *Tmem16b* and performed electrophysiological experiments in whole-cell configuration on dissociated OSNs. They demonstrated that the current mediated by CNG channels was still present, but the CaCCs was absent. This work also hypothesized that TMEM16B is dispensable for olfaction since the KO mice showed no impairment in the ability to detect odorants. Some years later, Pietra and colleagues (2016) using the same mouse model found that in *Tmem16b* KO the identification of new odors is not completely impaired, but the animals require more time to locate a food reward compared to the WT mice. When the animals already know the odor, they can perform the test equally to WT.

Functionally, TMEM16B can influence the firing behavior of OSN. Isolated OSNs from *Tmem16b* KO mice showed an increased number of APs and a prolonged duration of AP train in response to a stimulus. In KO mice the spontaneous firing activity is significantly reduced. This aberrant activity present in the KO animals could be responsible for supernumerary glomeruli observed in KO mice. In fact the correct targeting of OSNs axons to their glomeruli and the establishment and maintenance of the correct olfactory sensory maps in the OB is dependent on the spontaneous OSN spiking activity (Yu *et al.*, 2004; Lodovichi and Belluscio, 2012; Lorenzon *et al.*, 2015).

In 2017 Neureither and colleagues showed that the signal amplification mediated by TMEM16B is responsible for the correct detection and memorization of novel low intensity odors, but when the odor is familiar the detection is independent from this amplification mechanism. Probably in the KO mice the olfactory epithelium operates with reduced sensitivity and temporal resolution, causing a compromised integration of odorant stimuli. Thus the odor information is too blurred and is not possible to use it as a template for a correct spatial discrimination of odorants and localization of objects.

The prolonged responses observed by Pietra *et al*., (2016) can probably contribute to the reduced temporal resolution occurring during short interstimulus interval odor pulses found in the EOG recordings from Neureither and colleagues (Neureither *et al.*, 2017).

1.8. SARS–CoV2 and olfactory system

In December 2019 a new virus from the Coronaviridea family, severe acute respiratory syndrome coronavirus 2 (SARS-CoV-2) emerged and spread out across the planet. SARS-CoV-2 causes the COVID-19 (coronavirus disease 2019) syndrome, which includes fever, fatigue, headache, respiratory symptoms such cough, ageusia and anosmia. The major complication of the disease is represented by an abnormal activation of the inflammatory response which deteriorates lung function inducing alveolar oedema. SARS-CoV-2 is a positive sense single strand RNA virus. Its genome count is about 30kbp RNA and encode for sixteen nonstructural proteins, four structural proteins and eight accessory proteins (Wu *et al.*, 2020).

The infiltration of the virus into different cell types leads to the manifestation of the symptoms with different severity (Klingenstein *et al.*, 2021). The age and health condition of the infected person (hypertension, diabetes and cardiovascular disease) are considered important factors in the development and in the outcome of the disease (Jian *et al.*, 2020).

In COVID-19 patients anosmia has been reported as a common symptom in which nasal inflammation or coryzal symptoms are commonly absent. Usually, a typical post-viral anosmia, associated with a direct damage of the OSNs, is present as a major symptom during and after the infection and can take months to fully recover. This suggests that SARS-CoV-2 infects the cells through a mechanism distinct from those used by other more common viruses (Brann *et al.*, 2020).

The main gate for the virus entrance is the nose and nasopharynx. SARS-CoV-2 enters the cells in a way that depends on the Spike (S) protein which is present on the virus capsid. The Spike protein binds the angiotensin-converting enzyme-2 (ACE2) located on the surface of the target cell. ACE2 was characterized as the main entrance receptor for SARS-CoV-2 (Inhibitor *et al.*, 2020; Letko, Marzi and Munster, 2020). To enter the cells, the virus needs two further players: the transmembrane protease TMPRSS2 and the proprotein convertase furin. Furin cleaves the Spike protein at the S1/S2 site and TMPRSS2 at the S2’ site. These cleaves activate the viral S protein and allow the virus-cell fusion and cell entry (Figure 17; Bestle *et al.*, 2020).

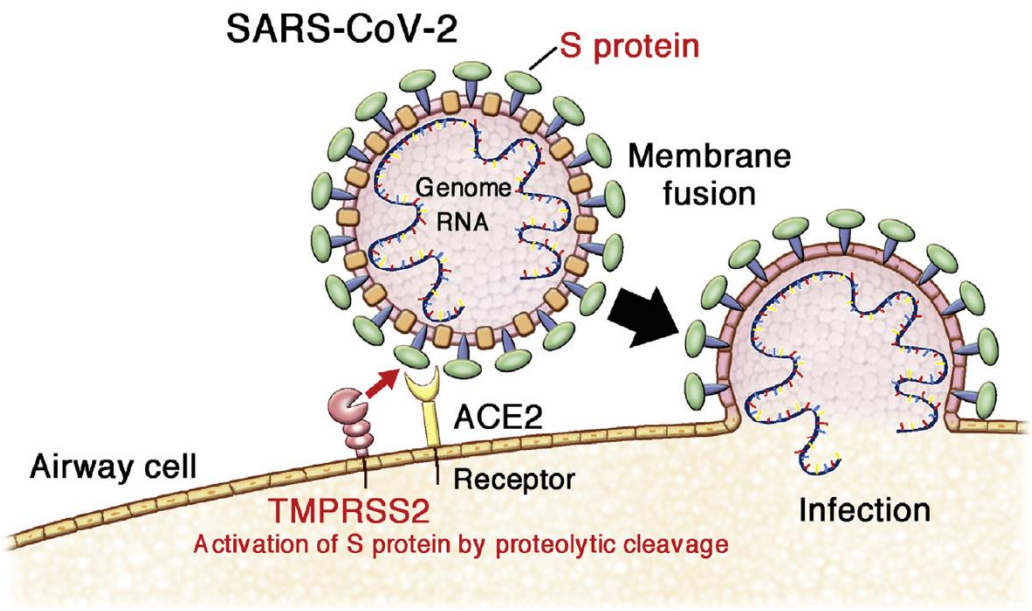


Figure 17 Interaction between SARS-CoV-2 and human airway cells
SARS-CoV-2 binds to ACE2 expressed on human airway cells. TMPRSS2 activates the spike protein and allow the virus cell fusion and the entry of virus (from Jian *et al*., 2020).

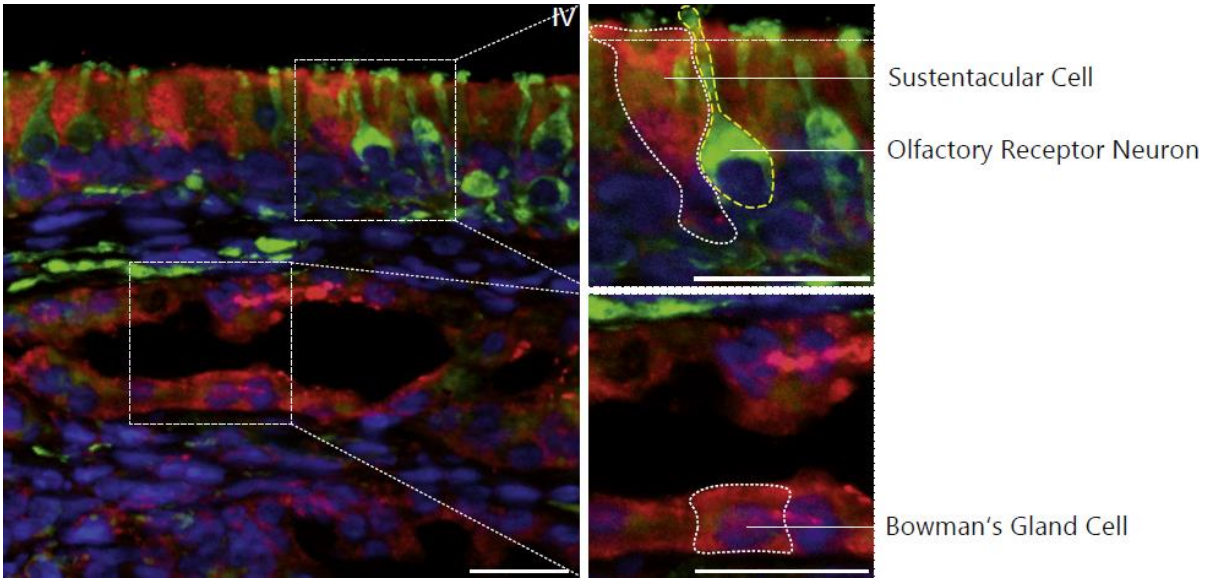
1.8.1. Expression of SARS-CoV-2 entry genes in human and mouse OE

Since COVID 19 infection is related with respiratory symptoms, like dry cough, anosmia and sore throat, the main target of SARS-CoV-2 virus are the respiratory cells, specifically the cells expressing the ACE2 receptor and TMPRSS2, since these proteins have strong virus binding capacity (Zou *et al.*, 2020). Different work tries to identify the direct target of SARS-CoV-2 infection in term of cell susceptibility (mainly the cells that express ACE2 and TMPRSS2) in order to understand the mechanism through which COVID-19 alters smell perception.

Focusing on the upper respiratory tract, Klingenstein and colleagues used immunofluorescence stainings from tissue obtained from human body donors to show that the proteins ACE2 and TMPRSS2 are expressed in the SCs cells and Bowman glands of the olfactory epithelium but not in the primary sensory neurons. In the respiratory epithelium, ACE2 is expressed in the basal cell layer and in the apical part of the respiratory epithelial cells (Figure 18; Klingenstein *et al.*, 2021). The expression of ACE2 in SCs was also observed by Fodoulian *et*

al., (2020) and Brann *et al*., (2020). Brann also detected the expression of ACE2 in HBCs (Figure 19).

A



B

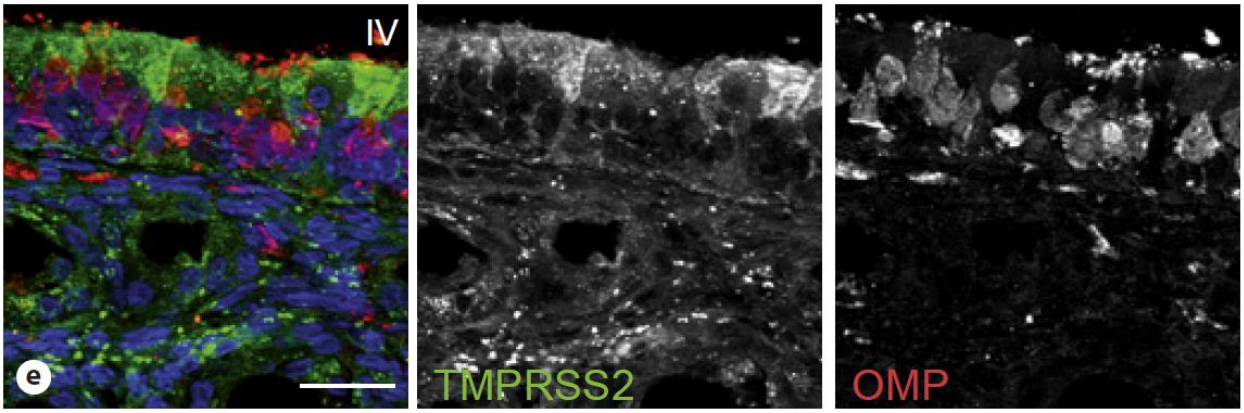


Figure 18: Immunofluorescence staining of coronavirus cell entry–related genes in the human olfactory epithelium.

A: ACE2 was showed in red, OMP in green. ACE2 staining is exclusively located to the region of the SCs, not in basal cells or co-localized with OMP. B: TMPRSS2 was showed in green and OMP in red. TMPRSS2 is mainly expressed in the SCs and shows a minor expression in Bowman glands, no appearance in basal cells or in OMP-positive mature OSNs. Nuclei are shown in blue. Scale bar 20 µm (from Klingenstein *et al*., 2020)

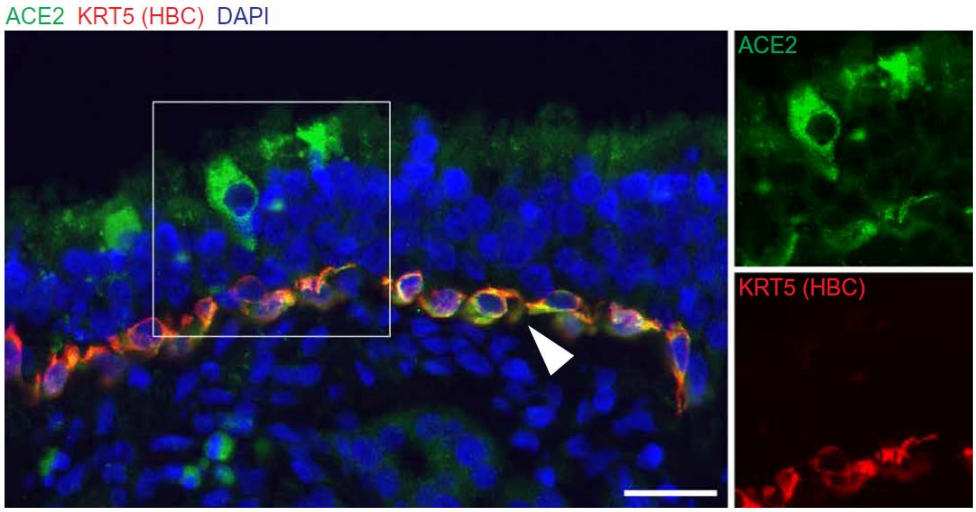


Figure 19: Immunofluorescence staining of coronavirus cell entry–related genes in the olfactory epithelium. Human olfactory mucosal biopsy marked with antibody against ACE2 (showed in green) and against KRT5 a marker for HBCs (showed in red) and nuclei (showed in blue). Scale bar 25 µm. ACE2 staining was detected in SCs and in HBCs (from Brann *et al*., 2020).

To understand in which type of cells ACE2 and TMPRSS2 are expressed in humans different research groups performed RNA seq techniques. Ziegler *et al*., (2020) found that the human nasal airway epithelium expresses ACE2 and TMPRSS2 in secretory goblet cells. This distribution has been confirmed also by Hikmet *et al*., (2020) and Sungnak *et al.,* (2020). Other studies reported the expression of ACE2 in ciliated cells (Hikmet *et al.*, 2020; Sungnak *et al.*, 2020; Ziegler *et al.*, 2020). The expression of ACE2 and TMPRSS2 was also reported in SCs by Fodoulian *et al.,* (2020) and Brann *et al.,* (2020). Fodoulian also confirmed that OSNs do not expressed ACE2 but showed low levels of TMPRSS2 expressions.

The expression of SARS-CoV-2 entry genes has also been studied in mice. Fodoulian *et al.,* (2020) investigated the expression of ACE2 and TMPRSS2 in tissue performing immunofluorescence experiments. They found a strong labeling of ACE2 in the respiratory epithelium and in the SCs located in the dorsal part of the nasal cavity. The signal of ACE2 was reported at the very luminal border of the SCs. TMPRSS2 immunoreactive cells also overlapped the SCs. This expression of ACE2 patter was also confirmed by Brann and colleagues (2020).

RNA seq experiments performed on olfactory epithelia confirmed the expression of ACE2 and TMPRSS2 in the olfactory epithelium mainly in non-neuronal cells (Kanageswaran *et al.*, 2015; Saraiva *et al.*, 2015; Bilinska *et al.*, 2020).

1.8.2. Cellular mechanisms behind the loss of smell in COVID-19 patients

The loss of smell, anosmia, is a common symptom of COVID-19, and usually occurs in the early stage of the disease sometimes as the only symptom (Meng *et al.*, 2020). The cellular mechanism for this dysfunction is not totally clear. The impairment of olfaction is associated with local inflammation of the olfactory epithelium or by the damage of the OSNs.

Immediately after the onset of the pandemic it became clear that SCs (that express high levels of ACE2 and TMPRSS2) but not OSNs are the cells susceptible to the infection in the OE. There are very few and sporadic cases in which OSNs were infected, making it implausible that these rare events would give rise anosmia (de Melo *et al.*, 2021; Meinhardt *et al.*, 2021).
Also it is important to highlight that SARS-CoV-2 reaches the leptomeningeal layers of the olfactory bulb but does not infect olfactory bulb neurons. SARS-CoV-2 does not appear to be a neurotropic virus (Khan *et al.*, 2021).

In the olfactory system, the SCs are exposed to the external environment and have also a protective role. The expression of enzymes from the cytochrome P450 family in this cell subtype underline that these cells also protect OSNs from volatile chemicals. The SCs allow the turnover of the odorant binding protein-odor complexes since they incorporate this complex after the initiation of signal transduction in the cilia of OSNs (Strotmann and Breer, 2011). Moreover, the SCs have a metabolic role, providing glucose to the cilia of OSNs, essential to provide the energy for the olfactory transduction mechanism (Bilinska and Butowt, 2020; Klingenstein *et al.*, 2021). The infection of the SCs, since they cover multiple functions leads to an impaired olfactory perception even if the infection does not affect directly the OSNs. This happens because the SCs are functionally and anatomically tightly linked with OSNs (Khan *et al.*, 2021).

There are different hypothesis explaining the mechanism leading to olfactory dysfunction in COVID-19. Bryche and colleagues (2020) (ref) using a hamster model showed the accumulation

of virus in SCs and not in OSNs. In this study, in order to understand the extent of the damage of the OSNs, they examined the anatomical preservation of the OSN cilia layer (in which all the transduction complex is located). They show that after the infection the cilia are lost, the olfactory transduction is not functional, and the olfactory capacity is impaired. The cilia are impaired very early, usually 2 days after the infection (DPI) and start to recovery at 7 DPI and are totally restored after 14 DPI. So, according to this hypothesis the rapid loss of smell is caused by the damage of the cilia structure (Figure 20). The loss of cilia following SARS-CoV-2 infection in hamster was also demonstrated through scanning electron microscope by de Melo *et al.,* 2021 (Figure 21; Bryche *et al.*, 2020; de Melo *et al.*, 2021)

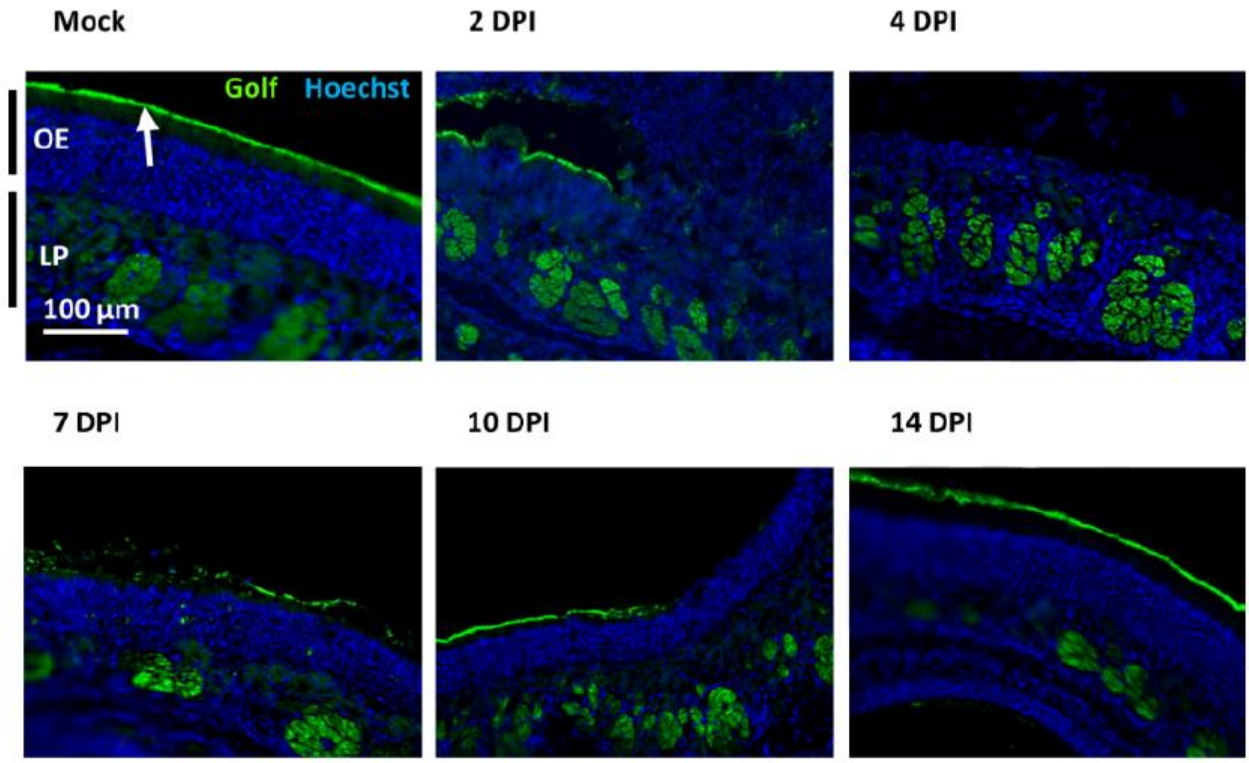


Figure 20: Immunostaining against Golf in hamster olfactory mucosa.

In mock conditions, the OE retains the cilia but in infected animals most of the cilia was eliminated, but completely recover after 14 DPI. G_{olf} is shown in green and nuclei are shown in blue (from Bryche *et al.,* 2020).

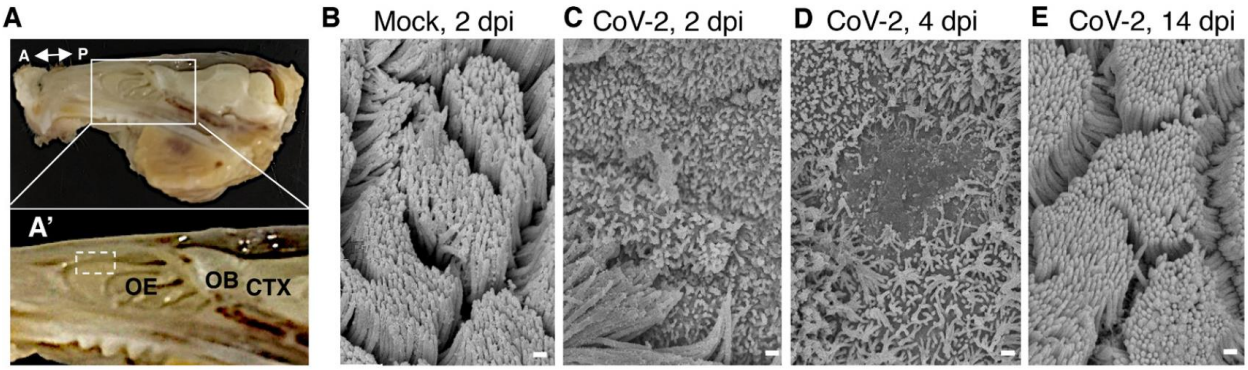


Figure 21: Scanning electron microscope image of hamster olfactory mucosa.

A) Dissected hamster head (B-E) scanning electron microscope imaging showing changes in the olfactory epithelium after SARS-CoV-2 infection. OSN cilia are impaired after SARS-CoV-2 infection. A loss of cilia is observed at 2 and 4 DPI for infected hamster. Scale bars: 1 µm (from de Melo *et al*., 2021).

The infection of SCs seems associated with a huge recruitment of immune cells in the OE and lamina propria, which induce rapid disorganization of the OE structure. Probably the immune response and the mechanism mediating the SC-induced disfunction of the olfactory system. However, the increased inflammatory damage caused by the immune response in the OSNs is not enough to justify the anosmia which is often reported in mild case and asymptomatic patients (Figure 22; Bryche *et al.*, 2020).

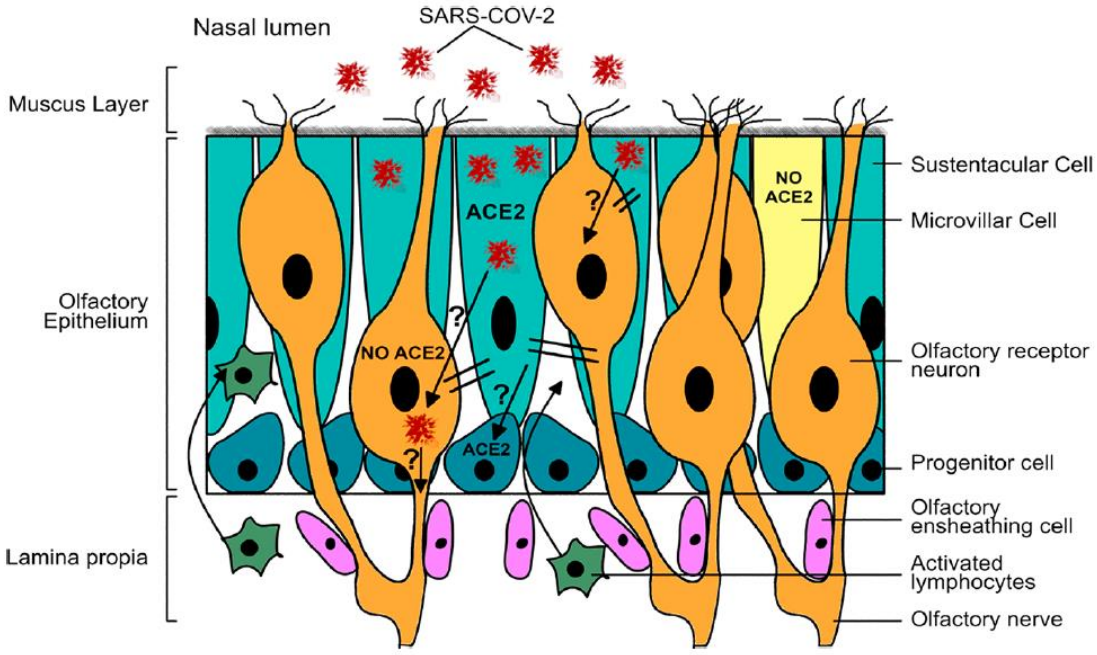


Figure 22: Model for SARS-CoV-2 induced anosmia.

SCs express ACE2 and are infected first, impairment of SCs negatively interferes with OSN function and leading to the inhibition of odor perception. Simultaneously a rapid immune response is induced in a subset of OSNs and in microvillar cells. This induces the migration of activated lymphocytes to the OE and induces the production of proinflammatory cytokines. It is not known whether SARS-CoV-2 bypasses OSNs as these neurons do not express ACE2 but probably a local immune response may participate in the process leading to anosmia in COVID-19 (Bilinska and Butowt, 2021).

Surprisingly, two of the other six human coronavirus SARS-CoV and HCoV-NL63 also use ACE2 for entry but usually do not cause olfactory dysfunction (Van Der Hoek *et al.*, 2004; Hofmann *et al.*, 2005; Fung and Liu, 2019). Often the expression pattern of the receptors can predict which cells can be infected but doesn't indicate that the cells expressing this receptor are the main targets (Weiss, 2020).

In COVID-19 disease usually the perception of smell is restored within 1-2 weeks, the time necessary for the differentiation of progenitor cells into SCs and for the correct placement of mature OSNs in the epithelium. The basal cells, the stem cells of olfactory epithelium, are not affected by COVID-19 and this explain the fast recovery in patients suffering of COVID-19 related anosmia.

1.8.3. The role of TMEM16F in SARS-CoV-2 spike-induced syncytia

In 2021 two different groups analyzed with histological techniques the lungs of patients with COVID-19 and found significant alveolar damage and multinucleated pneumocytes. The multinucleated pneumocytes are condensed cellular structures defined as syncytia and are characterized by a large cytoplasm containing multiple nuclei (from 2 to more than 20) (Figure 23a; Braga *et al.*, 2021; Zhang *et al.*, 2021). In the occurrence of these morphological abnormalities, a causal role has been attributed to the SARS-CoV-2 virus. During the infection, the cells that express SARS-CoV-2 Spike protein on plasma membrane can fuse and form syncytia with other cells that express the respective receptor, ACE2 (Braga *et al*., 2020).

Studies in vitro have demonstrated that the infection and the expression of a codon optimized cDNA of Spike protein from SARS-CoV-2 in Vero cells induces the formation of syncytia recapitulating the SARS-CoV-2 infection (Figure 23b). Interestingly, when Vero cells were transfected with Spike protein from SARS-CoV-1, syncytia do not occur. Comparing the Spike protein from SARS-CoV-1 and SARS-CoV-2 Zhang and colleagues (2021) in SARS-CoV-2 found an insertion of four amino acids (PRRA) before the S1/S2 cleavage site; this aminoacidic sequence is fundamental for the formation of syncytia.

How the syncytia can impact the pathology is not totally understood but there are different hypotheses; the syncytia can facilitate the spreading of the virus through cells that are in contact or the syncytial collapse could induce a virus release and trigger an inflammatory immune response (Rajah *et al.*, 2021).

The spike-mediated cell fusion mechanism and the syncytia occurrence seems to be associated with TMEM16F protein (a calcium-activated scramblase and ion channel). Braga and colleagues screened two libraries of EMA/FDA approved molecules in order to find a drug that inhibit the formation of syncytia. They found Niclosamide, a synthetic salicylanilide approved for tapeworm infection in humans, that even at very low concentration could reduce cell death after viral infection. Niclosamide is also an antagonist of TMEM16F. Decreasing the activity of TMEM16F prevent the externalization of phosphatidylserine on the outer leaflet of the cell plasm membrane (Cappelletto *et al.*, 2021).

The causal role of TMEM16F and the formation of syncytia has been reported in another study. After the infection by SARS-CoV-2 the cells expose on the surface the Spike protein that interacts with ACE2 receptor of the neighboring cells and induces the activation of TMEM16F that leads to the formation of syncytia (Lin *et al.*, 2021). This new TMEM16F-dependent mechanism seems fundamental for the severe outcome of SARS-CoV-2 and underlines the importance of this family of channels in the disease.

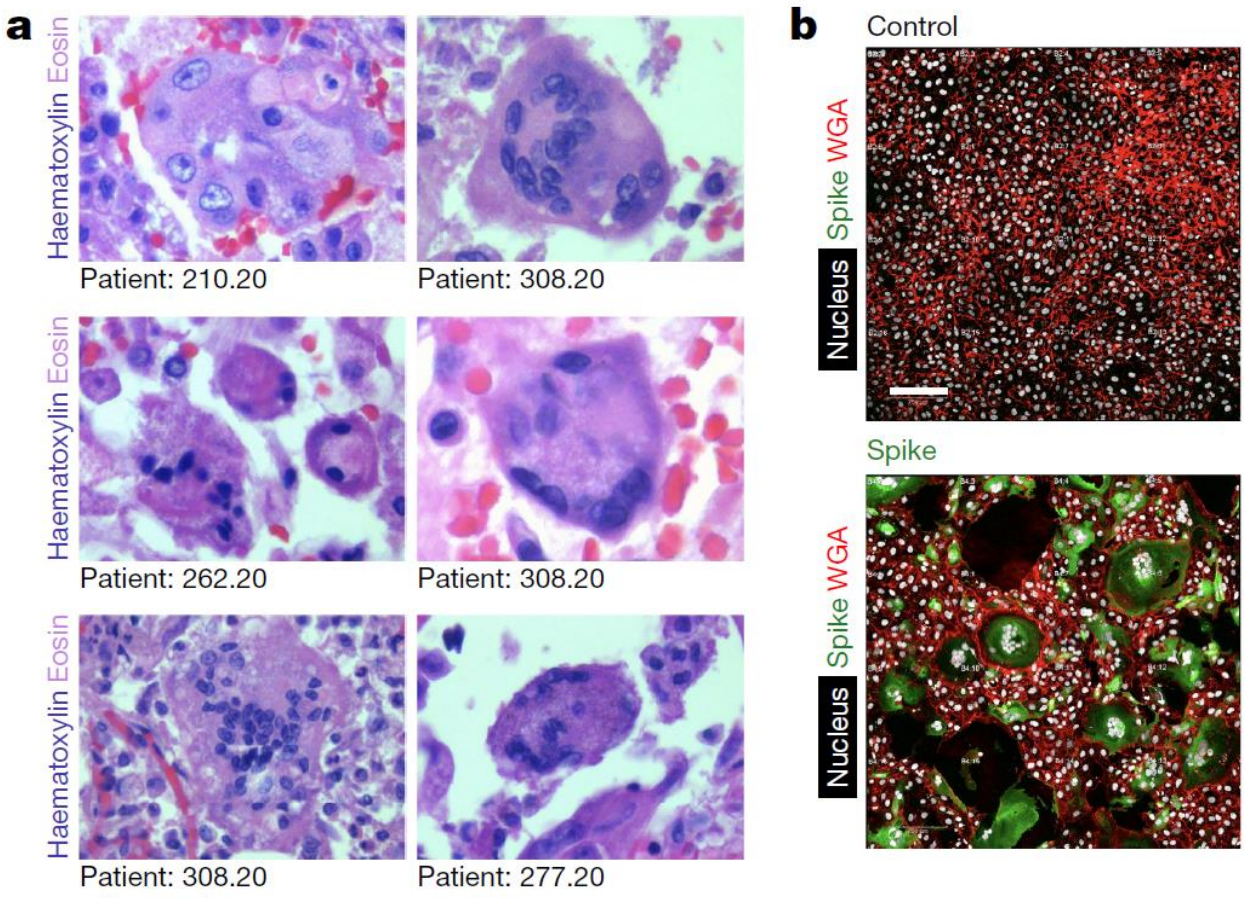


Figure 23: SARS-CoV-2 spike protein induced syncytia.
a) Haematoxylin/eosin staining of lungs of patients that died of COVID-19 showing multinucleated syncytia. b) in vitro experiments show the formation of syncytia after 24h expression of spike in Vero cells. Nuclei are stained in white, spike protein in green, cell contours in red using wheat germ agglutinin (WGA). Scale bar 200 µm (from Braga *et al.*, 2021).

2. Aims

The first part the specific aims of this work are:

- To investigate the role of the Ca^{2+} activated Cl^- channel TMEM16B in odorant-induced responses in olfactory sensory neurons using EOG recordings.
- To study the role of TMEM16B in odorant-induced adaptation in olfactory sensory neurons using the patch-clamp technique in various configurations

In the second part the specific aim of this work was:

- To investigate the expression of several proteins involved in SARS-CoV-2-induced syncytia in human olfactory and respiratory epithelium.

The role of TMEM16B in odorant adaptation of mouse olfactory sensory neurons

3. Materials and Methods

3.1 Animals and ethical approval

Mice were handled in accordance with the Italian Guidelines for the Use of Laboratory Animals and the European Union guidelines on animal research and according to a protocol approved by ethics committee of Scuola Internazionale Superiore di Studi Avanzati (SISSA). Experiments were performed on WT and *Tmem16b* KO mice of either sex. Mice had free access to water and food. For the experiments, mice were sacrificed by anaesthetizing them by CO_2 inhalation followed by decapitation. Adult mice were used for EOG recordings, while P0-P4 post-natal mice were used for patch-clamp recordings The *Tmem16b* KO model was kindly provided by Prof. Lily Jan (University of California, San Francisco, USA, Zhang *et al.*, 2017).

3.2 Electro-olfactogram recordings

The experimental procedure was similar to that described by Zhao *et al*., (1998) and Franceschini *et al*., (2009). After the mouse was sacrificed, the head was cut sagittally and the nasal septum was carefully removed to expose the olfactory turbinates. The turbinate samples were placed on a dissecting microscope located on a vibration-isolating table and shielded from electrical fields by a Faraday cage. The recording electrode was made with borosilicate glass (World Precision Instruments) pulled with a PP-830 puller (Narishige) to obtain a tip diameter of 10-20 µm. The tip of the pipette was filled with Ringer's solution with 0.5% of agar and the pipette was filled with Ringer's solution. Ringer's solution contained (in mM) the following: 140 NaCl, 5 KCl, 2 $CaCl_2$, 1 $MgCl_2$, 10 Hepes, pH 7.4 with NaOH. The recording electrode was mounted in a pipette holder and was carefully put on the turbinate of the olfactory epithelium. The recording electrode touched gently the surface of the olfactory epithelium. The ground electrode was placed in the brain of the mouse. The hydration of the epithelium was guaranteed by a constant stream of humidified and deodorized air over the turbinate. The stimulus pulse was controlled by a Picospritzer controlled valve (Parker Hannifin). For stimulation, a 100 ms pulse of vapor

phase odorant was injected at 10 psi into a continuous stream of humidified air. Vapor phase odorant as the stimulus were generated by placing an odorant solution in a 10 ml glass test tube capped with a rubber stopper. Two 20-gauge needles provided the input and output ports for the odorant-containing vapor above the solution (Figure 24). Each odorant, Isoamyl acetate (IAA) and Heptanal, was prepared every day as 5 M stocks in dimethyl sulfoxide (DMSO) and then diluted with water in order to reach a final concentration from 10^{-5} to 10^{-1} M. The recordings were made from 2 points from the olfactory epithelium, in the anterior region in turbinate II and in the posterior region in turbinate IV. The minimum interval between stimulations, excluding those explicitly indicated, was at least 3 minutes. Experiments were performed at room temperature. The data were collected with an Axopatch 1D amplifier controlled by Clampex 9.2 via Digidata 1322A (Axon Instruments, USA). The signals were recorded at a sampling rate of 1 kHz and low-pass filtered at 20 Hz. All chemicals were purchased from Sigma.

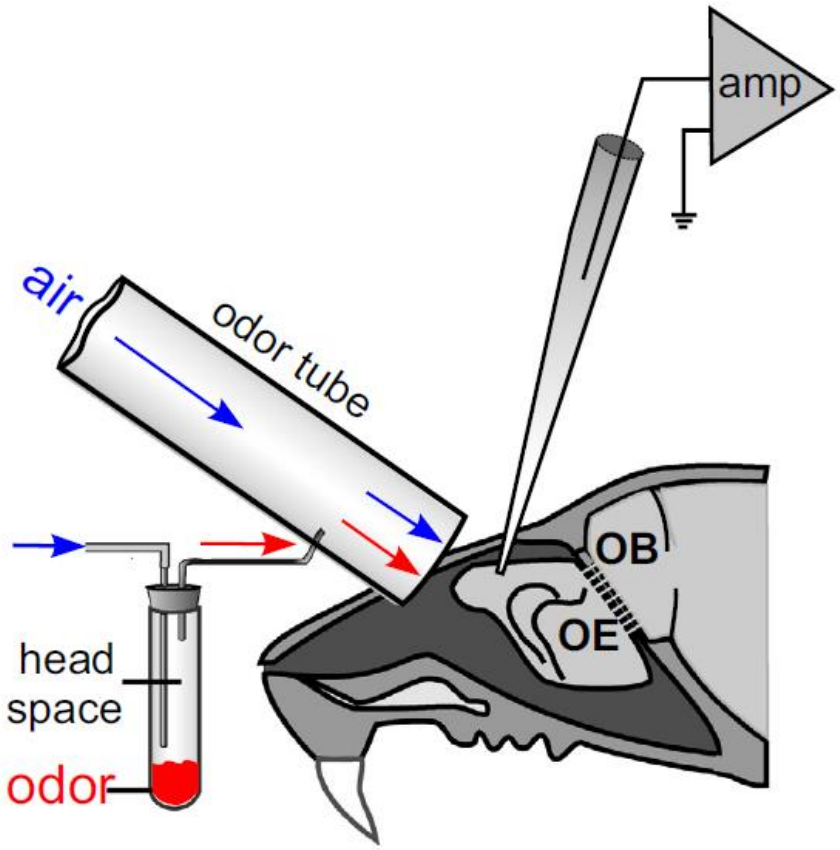


Figure 24: Electroolfactogram recording from mouse olfactory epithelium

The recording electrode was gently placed on the surface of the OE to record the negative change in the voltage when odorant is delivered. A constant stream of humidified air guarantees the hydration of the OE, the air phase odorant is delivered to the OE by injecting pressured air into a vial containing air saturated of odorant (from Neureither *et al.*, 2017).

3.3 Preparation of acute slices of mouse olfactory epithelium

Acute coronal slices of olfactory epithelia of P0-P4 mice were obtained with a method similar to previously described by Henriques *et al.*, (2019) and Agostinelli *et al.*, (2021). Mice at this age are suitable for use since TMEM16B is already express at P0-P4 (Maurya and Menini, 2014; Maurya *et al.*, 2015). After the mouse was sacrificed, the head without the skin was

dissected and embedded in 3% low grade agar prepared in Ringer's solution once the solution had cooled to 38°C. After solidification the agar block was fixes in a glass Petri dish filled by oxygenated Ringer's solution and a vibratome was used to cut the coronal slices of 300 μm thickness (Vibratome 1000 Plus Sectioning System). The slices were kept in cold oxygenated Ringer's solution until use.

3.4 Electrophysiological recordings from OSNs and stimuli presentation

Slices were viewed with an upright microscope (BX51WI, Olympus) equipped with a 40X water immersion objective with an additional 2X auxiliary lens. The recording chamber was continuously perfused with oxygenated Ringer's solution at room temperature. Extracellular solutions were exchanged through an eight-in-one multibarrel perfusion pencil connected to a ValveLink 8.2 pinch valve perfusion system (Automate Scientific). With this perfusion system the solution arrived with a delay of 300/400 ms. The bath was connected with an Ag/AgCl reference electrode through a 3 M KCl agar bridge. OSNs were identified by their morphology. The experiments were performed at room temperature (20-25 °C). Patch pipettes were pulled from borosilicate capillaries (WPI) with a Narishige PC-10 puller.

In the whole-cell voltage clamp configuration experiments the pipette had a resistance of 4-7 MΩ when filled with the intracellular solution. We used an intracellular solution composed of (in mM) 145 KCl, 4 $MgCl_2$, 0.5 EGTA, and 10 HEPES (adjusted to pH 7.2 with KOH) to measure the voltage-gated currents and the passive properties of the OSNs. The voltage-gated current was measured in voltage clamp mode, holding the potential at -90 mV and applying a voltage step protocol from -100 mV to + 40mV with 10 mV increment. In voltage clamp mode, we also evaluated the membrane input resistance. We held the potential of the cell at -90 mV and gave a negative pulse of 20 mV. In these conditions, the voltage-gated currents are not activated (Dibattista *et al.*, 2008). In current clamp mode (without injecting current), we measured the resting membrane potential. With another intracellular solution composed of (in mM) 13 KCl, 132 KGluconate, 4 $MgCl_2$, 0.5 EGTA, and 10 HEPES (adjusted to pH 7.2 with KOH) we isolated the

current mediated CNG channels. With this solution the reversal potential for Cl^- corresponds to the holding potential of -50 mV, in this condition the current is mainly mediated by CNG channels. When we set the holding potential of -90 mV we measured also the current mediated by Ca^{2+} activated Cl^- channels.

Extracellular recordings from the soma of OSNs were obtained in the loose patch configuration using a pipette with a resistance of 3-4 MΩ when filled with Ringer's solution. During the experiments the seal resistances were 30-50 MΩ. Loose patch experiments were made in voltage clamp mode with a holding potential of 0 mV.

The recordings were performed using a MultiClamp 700B amplifier controlled by Clampex 10.6 via Digidata 1550B (Axon Instrument, USA). Data were low pass filtered at 2kHz and sampled at 10kHz.

The cells were stimulated with a mix of odorants composed of heptanal, isoamyl acetate, acetophenone, cineole and eugenol. Each odorant was prepared as a 5 M stock in dimethyl sulfoxide (DMSO) and then on the day of experiments was diluted in Ringer's solution to reach the final concentration of 100 μM. This concentration induces saturating responses from OSNs expressing several types of odorant receptors (Dibattista and Reisert, 2016).

We also stimulated the neurons with 3-isobutyl-1- methylxanthine (IBMX). IBMX is a phosphodiesterase (PDE) inhibitor and it induces an increase of the cAMP concentration. Some OSNs have a relatively adenylyl cyclase high activity and blocking of PDEs causes a rise of cAMP normally hydrolyzed by PDEs. IBMX was prepared weekly and used at the concentration of 1 mM dissolving the powder directly into Ringer's solution without the use of DMSO. At this concentration IBMX elicits responses with kinetics like those induced by odorants (Reisert, Yau and Margolis, 2007).

3.5 Data analysis

IgorPro software (Wavemetrics) was used for data analysis and to make the figures. Data are given as mean ± sem. Normal distribution of the data was tested with Shapiro-Wilk test. The homogeneity of the variance was tested using Levene's test. If the data are normally distributed and with the same variance statistical significance was determined using unpaired homoscedastic Student's t test. If data present a different variance an unpaired different variance Student's t test was used. For not normally distributed data, the Mann-Whitney U-test was used. P values of $p<0.05$ were considered statistically significant. Kolmogorov-Smirnov test was used to compare the cumulative ISI distribution in Figure 7. The loose patch recordings were filtered offline with a high pass filter at 5 Hz to correct for baseline drifts. Spikes were detected using an event detection algorithm setting an arbitrary threshold and then were confirmed by shape examination. To analyze the mean spontaneous firing frequency, we divided the number of spikes by the duration of the recording. The interspike interval (ISI) was calculated by measuring the time between two consecutive spikes. The ISI distribution was obtained by separating the ISIs in bins, as indicated in the figure, and dividing the value of each bin by the total number of ISIs for each cell. The values in the y axes represent the percentage of spikes in each bin and the area under the curve is 100%.

4. Results

4.1 TMEM16B mediates large transduction current and contribute to the OSN spontaneous activity

The Ca^{2+}-activated Cl^- channel TMEM16B is expressed in the cilia of OSNs and mediates up to 90% of the odorant-induced current (Boccaccio and Menini, 2007; Stephan *et al.*, 2009). Here, we investigate the role of TMEM16B in the adaptation mechanism of OSNs using a loss of function approach (Zhang *et al.*, 2017).

We tested whether *Tmem16b* deletion alters passive membrane properties of OSNs. Therefore, we performed whole-cell patch clamp recording on OSNs from acutely-isolated olfactory epithelium slices from P0-P4 mice. The zero-current membrane potential and the input resistance are not significantly affected by the lack of TMEM16B (-76 ± 3 mV and 5.7 ± 1.2 GΩ for WT n=22 and -81 ± 4 mV and 3.3 ± 1.0 GΩ for KO n=10, Figure 1C-D). We also compared the amplitude of voltage-gated currents in OSNs from WT and *Tmem16b* KO mice. Figure 1A shows representative whole-cell currents evoked by voltage step from -100 to +40 mV from a holding potential of -90 mV. We plotted the amplitude of the negative peak of the current after 20 ms from the voltage changes (to avoid to include the capacitive current) and the current at the end of the voltage pulses (Figure 1B). The amplitude of both the inward and outward currents are not significantly different for the two genotypes (-736 ± 93 pA and 832 ± 92 pA for WT n=23 and -710 ± 122 pA and 859 ± 112 pA for KO n=12).

Then we compared the transduction current amplitudes in OSNs from WT and *Tmem16b* KO. We performed whole-cell patch clamp recordings using a pipette solution that sets the equilibrium potential for Cl^- at -50 mV and we stimulated the OSNs with IBMX. At the holding potential of -50 mV, the stimulation with IBMX (1 mM) induces not significantly different small inward currents in OSNs from WT and (-27 ± 6 pA, n=10) *Tmem16b* KO mice (-19 ± 4 pA, n=9, Figure 1E-F). This current is mainly carried through CNG channels. In contrast, changing the holding potential to -90 mV increases the amplitude of the transduction current in WT OSNs while no changes are observed in *Tmem16b* KO OSNs (Figure 1E-F). The ratio of the current at -90 mV

and -50 mV is significantly higher in WT than in *Tmem16b* KO ONSs (3.1 ± 0.6 n=10 for WT; 0.9 ± 0.1 n=9 for KO; Figure 1G).

Previous studies reported that TMEM16B modulates the spontaneous firing frequency (Pietra *et al.*, 2016), therefore we evaluated the spontaneous activity in our *Tmem16b* KO model. We used loose-patch recording to measure the spontaneous action potential generation in OSNs from WT and *Tmem16b* KO mice (Figure 2 A-D). As previously reported, spike activity of OSNs from WT mice showed a high variability and the mean frequency of spike activity ranges from 0.1 to 6.6 Hz (Reisert, 2010; Connelly, Savigner and Ma, 2013; Lorenzon *et al.*, 2015; Pietra *et al.*, 2016). Similar variance is observed also in OSNs from *Tmem16b* KO, however the mean frequency of spontaneous frequency is significantly lower (2.0 ± 0.3 Hz n=29 for WT; 0.4 ± 0.1 Hz n=30 for KO) confirming previous results (Pietra *et al.*, 2016). By analyzing the distribution of interspike interval (ISI) we also found that OSNs from *Tmem16b* KO fire with a significantly higher ISI than WT neurons (Figure 2 F,G).

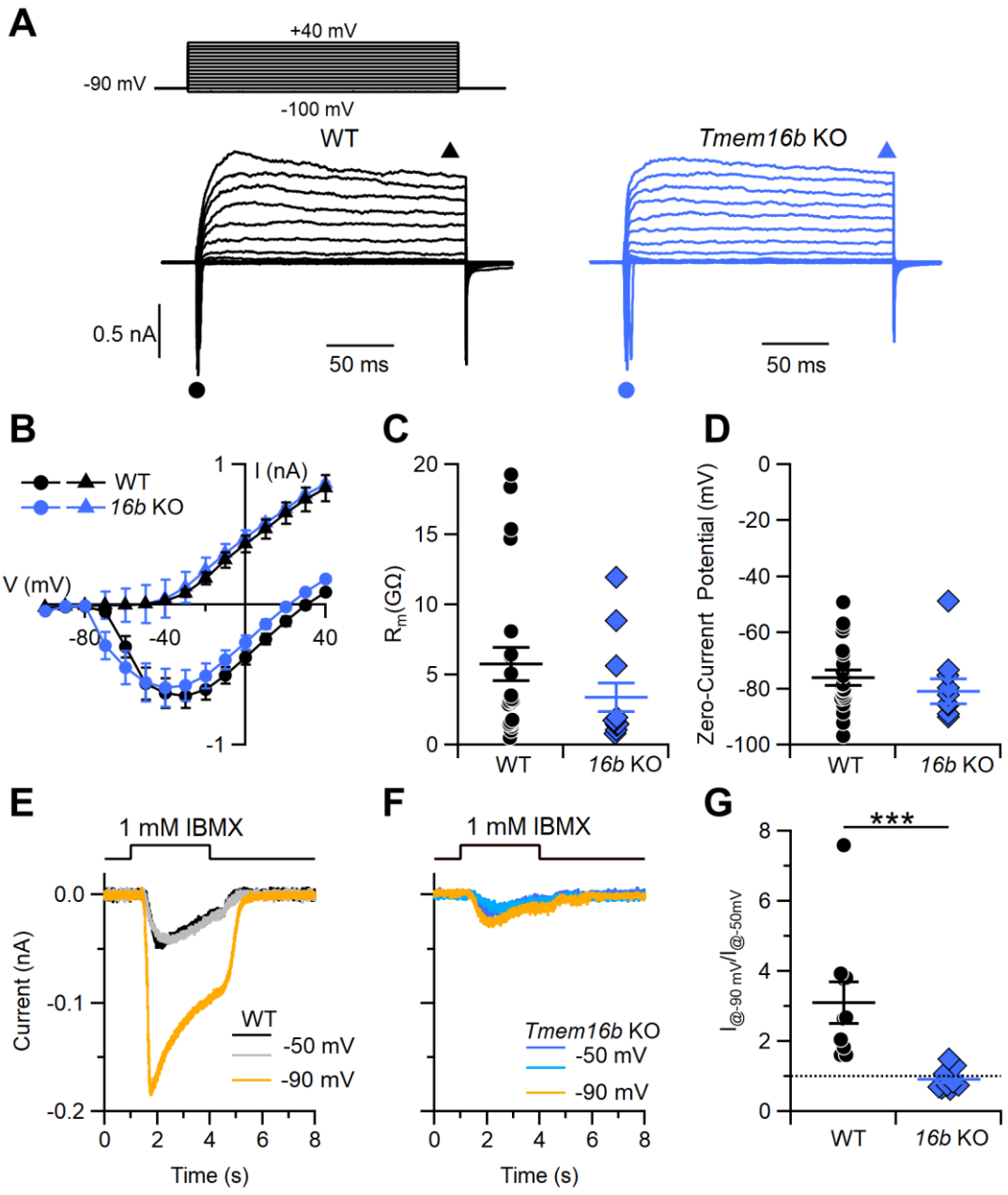

A
+40 mV
-90 mV
-100 mV
WT
Tmem16b KO
0.5 nA
50 ms
50 ms
B
WT
16b KO
I (nA)
V (mV)
1
-1
-80
-40
40
C
R_m(GΩ)
20
15
10
5
0
WT
16b KO
D
Zero-Currenrt Potential (mV)
0
-20
-40
-60
-80
-100
WT
16b KO
E
1 mM IBMX
Current (nA)
0.0
-0.1
-0.2
WT
-50 mV
-90 mV
0
2
4
6
8
Time (s)
F
1 mM IBMX
Tmem16b KO
-50 mV
-90 mV
0
2
4
6
8
Time (s)
G
***
I@-90 mV/I@-50mV
8
6
4
2
0
WT
16b KO

Figure 1 *Tmem16b* deletion abolishes the transduction chloride current without affecting the voltage-gated currents and membrane properties of OSNs. (A) Representative whole-cell recording of OSNs from WT and *Tmem16b* KO mice. Voltage steps of 200-ms duration were given from a holding voltage of -90 mV to voltages between -100 and +40mV in 10-mV steps. **(B)** Average ± sem of the IV relationships of inward currents (circles) and steady-state outward current (triangles) from WT (black, n=23) and Tmem16b KO (blue n=12) Values were taken at the negative peak (between the start of voltage step and 20 ms after voltage change) and at the end of voltage step as indicated by the symbols in A (p=0.73 unpaired t-test for inward current; p=0.64 U-test for outward current). Scatter dot plot with averages ± sem of input membrane resistance (**C**) and zero-current membrane potential (**D**) of WT (n=22) and *Tmem16b* KO (n=10) OSNs (p=0.12, U-test for R_m; p=0.41 unpaired t-test for zero-current potential). Representative whole-cell recordings of OSNs from WT (**E**) and *Tmem16b* KO mice (**F**) stimulated with IBMX (1 mM) at the indicated holding potential. We stimulated the cells holding the potential al -50 mV (black and blu traces), after -90 mV (orange traces) and at the end we repeated the stimulation at -50 mV (grey and cyan traces). (**G**) Scatter dot plot with averages ± sem of ration the IBMX-induced current at -90 mV and at -50 mV (n=10 for WT and n=9 for KO; $p=2.16*10^{-5}$ U-test).

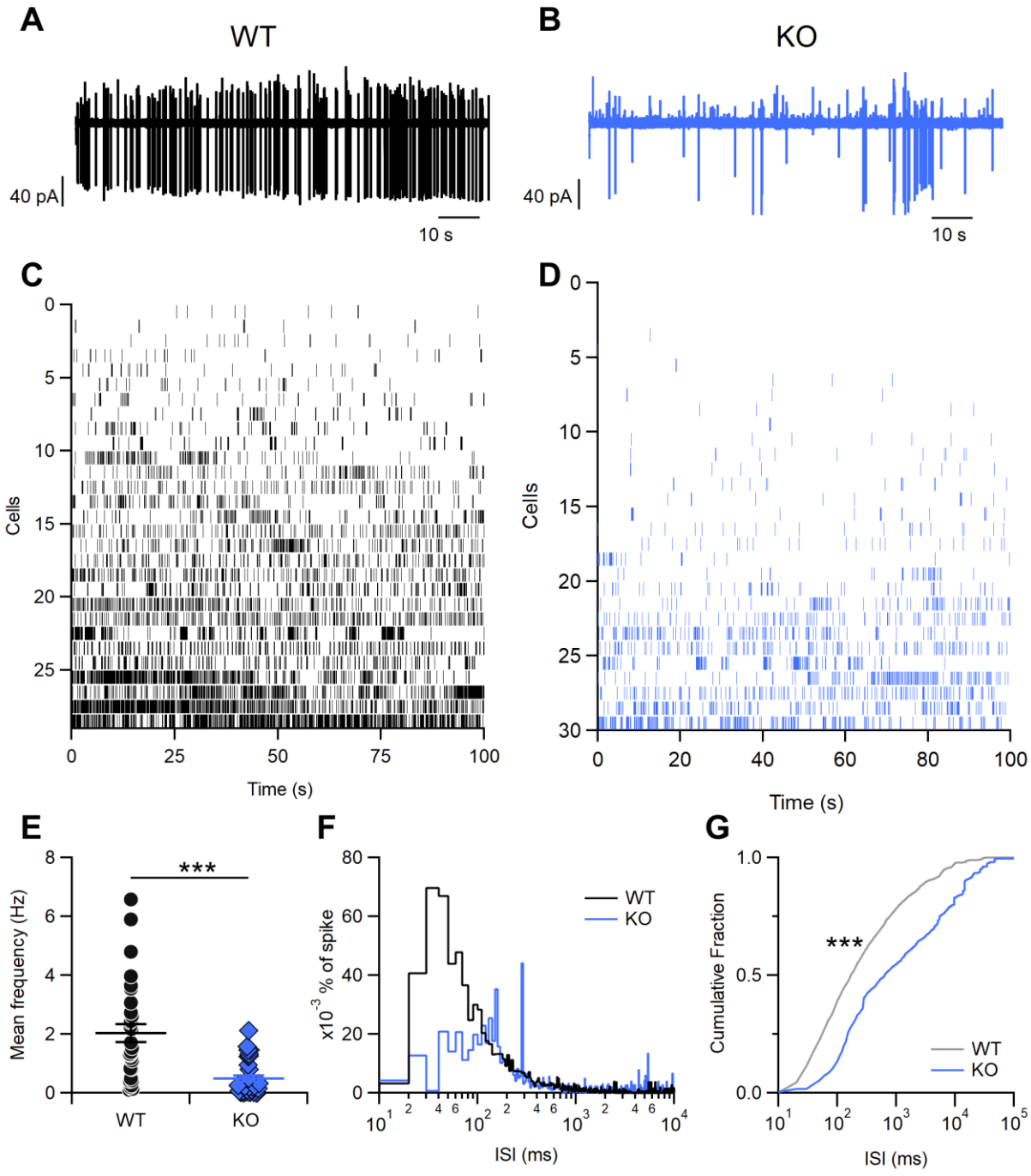


Figure 2 *Tmem16b* deletion alters the spontaneous firing activity in OSNs. Representative loose-patch recording from OSNs from WT (**A**) and *Tmem16b* KO (**B**) mice showing the spontaneous firing activity. Raster plot showing the spontaneous firing activity of various OSNs from WT (**C**) and *Tmem16b* KO (**D**) mice. (**E**) Scatter dot plot with averages ± sem of mean frequency of spontaneous firing activity of OSNs from WT and Tmem16b KO mice (n=29 for WT and n=30 for KO; $p=1.76*10^{-6}$ U-test). ISI distributions (**F**) and cumulative distributions (**G**) of spontaneous firing activity for the neurons shown in **C, D** (bin= 5 ms, ***p < 0.001, Kolmogorov–Smirnov test).

4.2 Odorant response in *Tmem16b* KO OSNs

To investigate how TMEM16B modulates OSN responses we recorded the negative electrical field potential, the electro-olfactogram (EOG) evoked by the stimulation with different types of odorants presented with different concentrations. Using this approach, we can record a summed potential generated by an odorant response in a population of OSNs close to the recording electrode. In order to cover as much as possible of the entire olfactory epithelium, we presented the odorant in two different areas of the OE.

Figure 3 A-B shows representative EOG responses induced by 100 ms long pulses of vapor phase of isoamyl acetate (IAA) solutions with concentration ranging 10^{-5} to 10^{-1} M of OE from WT and *Tmem16b* KO mice. Surprisingly, we found that the odorant response is significantly bigger in KO compared to WT mice both in the anterior and posterior parts of OE (Figure 3C-D). In the anterior part, the EOG amplitude evoked by the vapor phase of 10^{-1} M IAA solution is 7.18 ± 0.98 mV in WT (n=12) and 13.1 ± 2.23 mV in *Tmem16b* KO mice (n=11). Similar results were obtained using heptanal as the stimulus in the posterior part of OE (Figure 3F), whereas in anterior part the EOG amplitude from *Tmem16b* KO tends to be bigger than in WT mice but this difference is not statistically significant (Figure 3E).

We further analyzed the kinetics of the EOG recordings. We measured the latency as the time between the start of the stimulus and the time at which the response reaches 1% of its peak value; the rise time as the interval between the beginning of the response and the time of the peak response; and the time constant of the mono-exponential fit of the recovery phase of the EOG response. We found that rise time and the time constant of the recovery are significantly shorter in OE from *Tmem16b* KO with respect to WT mice (Figure 4). Similar results are obtained upon stimulation with IAA and heptanal both in anterior and posterior portion of OE.

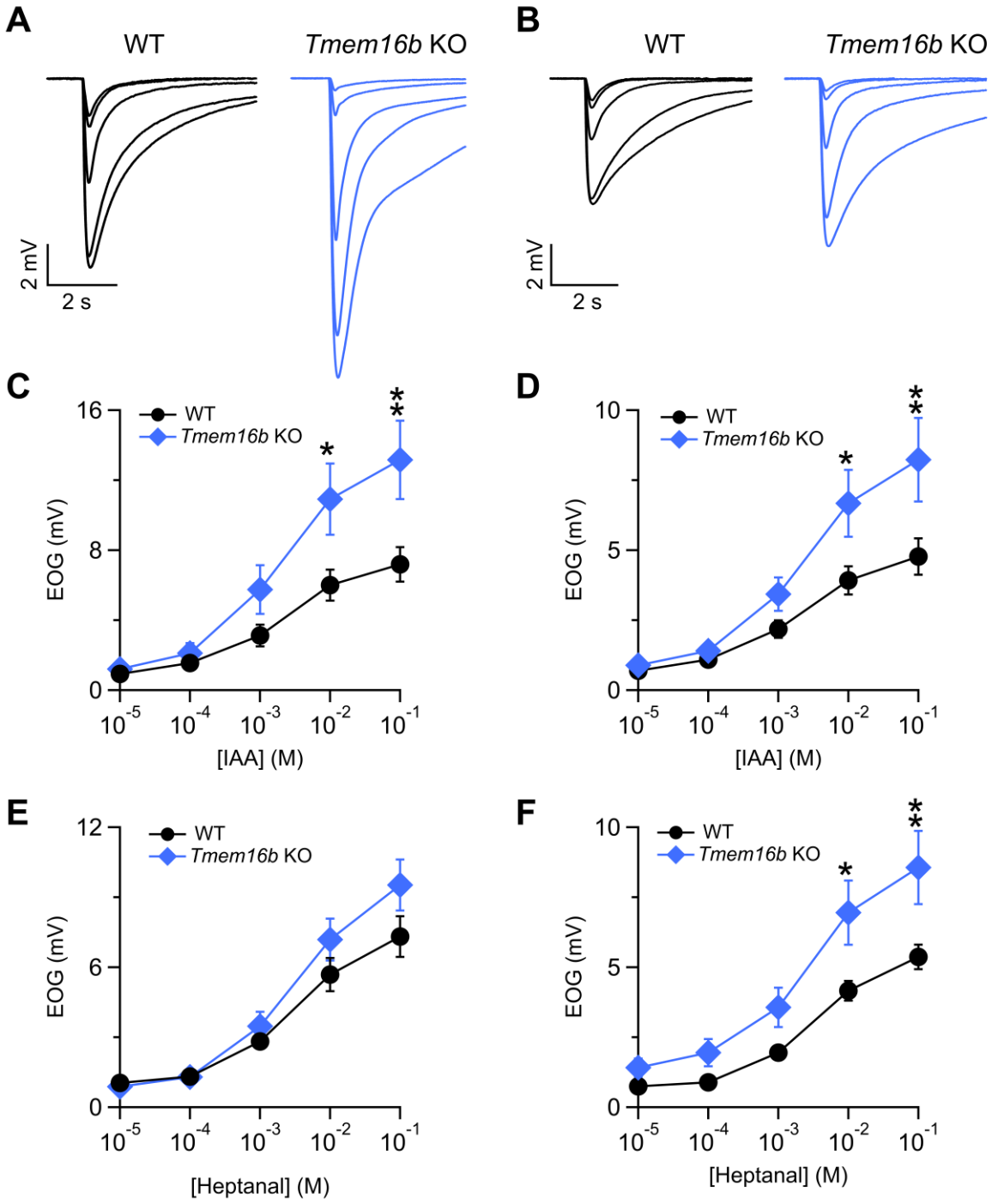

A
WT
Tmem16b KO
2 mV
2 s
B
WT
Tmem16b KO
2 mV
2 s
C
WT
Tmem16b KO
EOG (mV)
[IAA] (M)
D
WT
Tmem16b KO
EOG (mV)
[IAA] (M)
E
WT
Tmem16b KO
EOG (mV)
[Heptanal] (M)
F
WT
Tmem16b KO
EOG (mV)
[Heptanal] (M)

Figure 3: Odorant responses in WT and *Tmem16b* KO mice. Representative EOG recordings from WT (black traces) or *Tmem16b* KO (blue traces) mice. The responses were evoked by 100 ms stimulation with IAA vapor of increasing concentrations ranging from 10^{-5} to 10^{-1} M. EOG recordings were obtained from anterior (**A**) or posterior (**B**) portions of OE. Dose–response relationships of average peak EOG amplitudes from WT (black traces) or *Tmem16b* KO (blue traces) mice to IAA (**C-D,** n=12 for WT anterior and n=10 for WT posterior; n=11 for *Tmem16b* KO anterior and n=9 for *Tmem16b* KO; **p<0.01 *p<0.05 t-test with Bonferroni correction after mixed two way ANOVA or Heptanal (**E-F,** n=9 for WT anterior and n=11 for WT posterior; n=10 for *Tmem16b* KO anterior and n=10 for *Tmem16b* KO; *<0.05 Student's t-test) in the indicated OE location. Error bars represent sem.

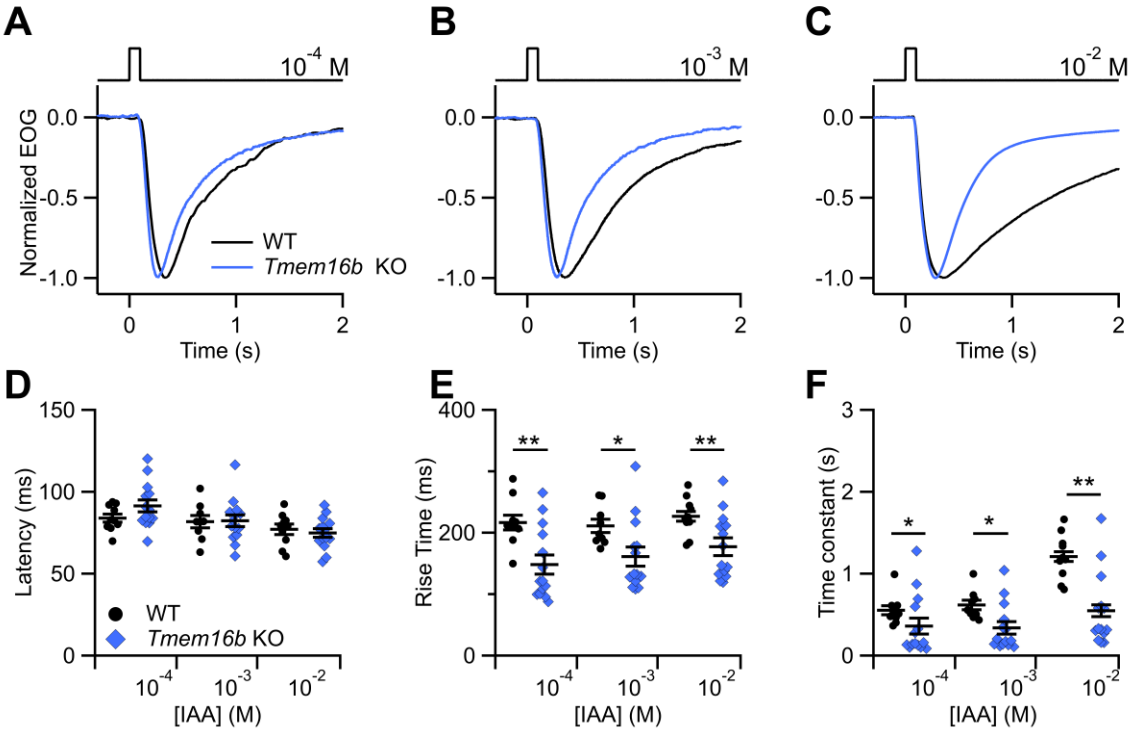


Figure 4. Kinetics of the odorant response in WT and *Tmem16b* KO mice. Representative normalized EOG recordings from WT (black traces) or *Tmem16b* KO (blue traces) mice. The responses were evoked by 100 ms stimulation of vapors of the indicated IAA solution concentration. (B) Scatter dot plot with average ± sem showing the values of latency (**D**), rise time (**E**) and time constant (**F**) in WT or *Tmem16b* KO mice at each odorant concentration (n=9 for WT at 10^{-3} M concentration and n=10 for WT at 10^{-2} and 10^{-1} M concentration, n=14 for *Tmem16b* KO at all the concentrations; *<p0.05 **p<0.01; for rise time 10^{-4} M and 10^{-3} M and for time constant 10^{-4}, 10^{-3} and 10^{-2} U test for latency at all concentrations and rise time 10^{-2} M Student's t test).

4.3 Olfactory adaptation in WT and *Tmem16b* KO mice

The odor-induced adaptation mechanism is used by the olfactory system to prevent the saturation of the cellular transduction machinery and it causes a shift of the dose response curve to higher odorant concentrations compared with the control state (Kurahashi and Menini, 1997; Reisert and Matthews, 1999).

In order to study the possible role of TMEM16B in OSN adaptation, we performed EOG recordings using double pulse experiments. We delivered two 100 ms-long odor pulses with interpulse intervals (IPI) ranging from 0.5 second to 5 seconds (Figure 5A, C). Since the response to the first odor pulse did not decay to baseline when the second pulse was applied, the recorded second response reflects a sum of the residual first response and the real response to the second pulse. In order to obtain the net second response peak amplitude we made a fit to the decay phase of the first response and subsequently subtracted the value of this trace at the peak time of the second response from the second pulse peak amplitude. To quantify the adaptation we calculated the ratio between the peak of second response and the first response ($2^{nd}/1^{st}$). At high odorant concentrations (10^{-3} M and 10^{-2} M), we found that responses from *Tmem16b* KO mice recover faster from adaptation than WT. At 10^{-3} M of IAA, the ratio $2^{nd}/1^{st}$ for IPI 0.5 s is 0.17 ± 0.02 for WT (n= 9) and 0.33 ± 0.02 for *Tmem16b* KO (n= 10), while for IPI of 1 s, the ratio $2^{nd}/1^{st}$ is 0.51 ± 0.02 for WT (n=9) and 0.38 ± 0.02 for KO (n=10; Figure 5). Similar results were obtained in different regions of the OE and using heptanal as stimulus (data not shown).

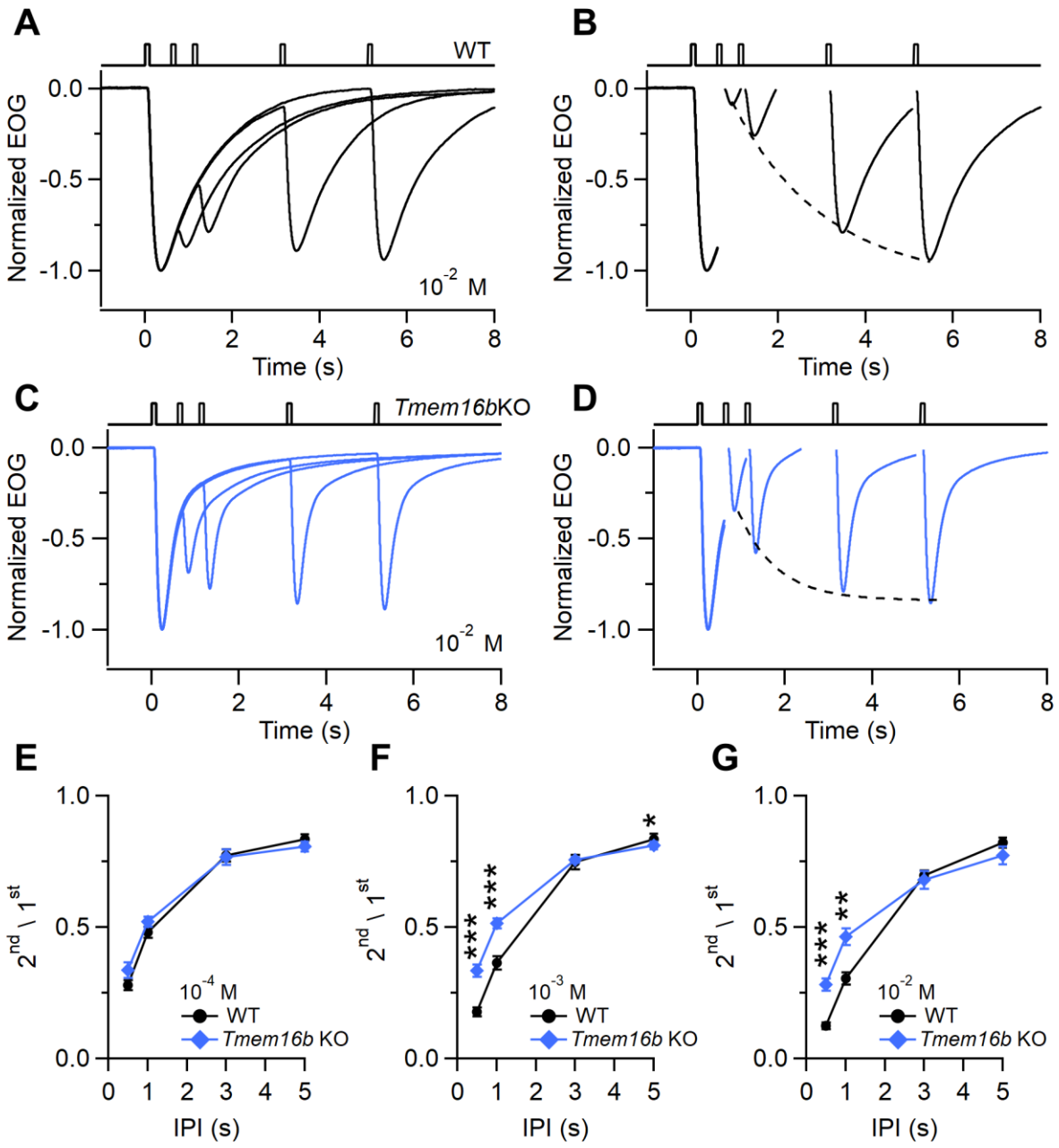


Figure 5. Double pulse odorant response in WT and *Tmem16b* KO mice. Representative normalized EOG double pulse responses from WT (**A**) and *Tmem16b* KO mice (**B**). OEs were stimulated with 100 ms-long pulses with different interstimulus intervals (0.5, 1, 3, 5 s) with vapor-phase of IAA at 10^{-2} M concentration. (**C-D**) Net responses to each stimulus for the recordings showed in (**A-B**). Dotted line represents the mono-exponential fit obtained with the peak responses to the second odor pulses. (**E-G**) Ratio of the second stimulus to the first ± sem at the indicated odorant concentration plotted versus the inter pulse interval (n= 9-10 for WT and n=8-10 for KO, * p<0.05; **p <0.01; *** p<0.001; for 10-2 M and 10-4 M at all IPI and 10-3 M IPI 5 and 0.5 s s we used Student's t test and for 10-3 M at IPI 10-1 M we used U test).

To test the effect of adaptation on dose response curves, we measured the EOG response to different vapor phase IAA solutions with concentrations ranging 10^{-5} to 10^{-1} M in control conditions and after 2 s of a conditioning odorant pulse at 10^{-3} M (Figure 6). In OEs from WT mice, the amplitude of the response at all odor concentration is significantly smaller after the conditioning odor pulse, whereas no significant difference was observed in OE from *Tmem16b* KO mice.

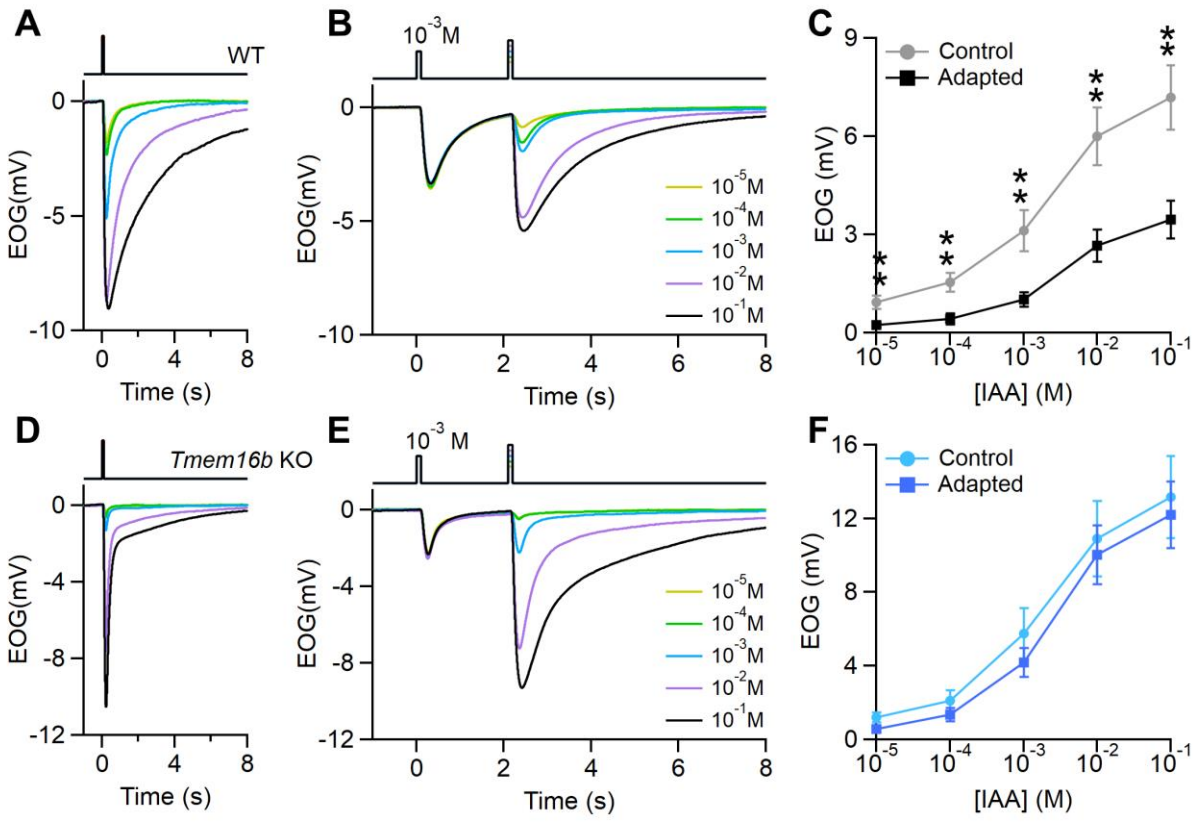


Figure 6. Dose response after a conditioning odorant pulse in WT and *Tmem16b* KO mice. Representative EOG dose response recordings from WT and *Tmem16B* KO mice in control conditions (**A,D**) or after 2 s of a conditioning odorant pulse at 10^{-3} M (**B,E**). Dose–response relationships of average peak EOG amplitudes from WT (**C**) or *Tmem16b* KO (**F**) mice in control condition and after a conditioning odorant pulse at 10^{-3} M (n= 6 for adapted response in WT and *Tmem16b* KO and n=12 for control WT and n=11 for control *Tmem16b* KO; ** $p < 0.01$ for WT mice we used Student's t test for all the concentration unless for 10^{-4} M we used U test; for *Tmem16b* KO we used for 10^{-2} and 10-1 M Student's t test and for 10^{-5}, 10^{-4} and 10^{-3} U test).

To investigate the role of TMEM16B in controlling adaption at the single-cell level, we recorded the action potentials evoked by odorant stimulation using loose-patch recordings. We used a double pulse protocol delivering two 1s-long odor pulses with interpulse intervals (IPI) ranging from 0.5 second to 12 seconds (Figure 7-8). As previously reported, OSNs from *Tmem16b* KO mice generate a significantly higher number of spikes after odorant stimulation (Pietra *et al.*, 2016). To compare the adaptation properties of different neurons, we calculated the ratio of the number of spikes of the second and the first stimulation, confirming that OSNs from *Tmem16b* KO mice recover faster from adaptation (Figure 8B).

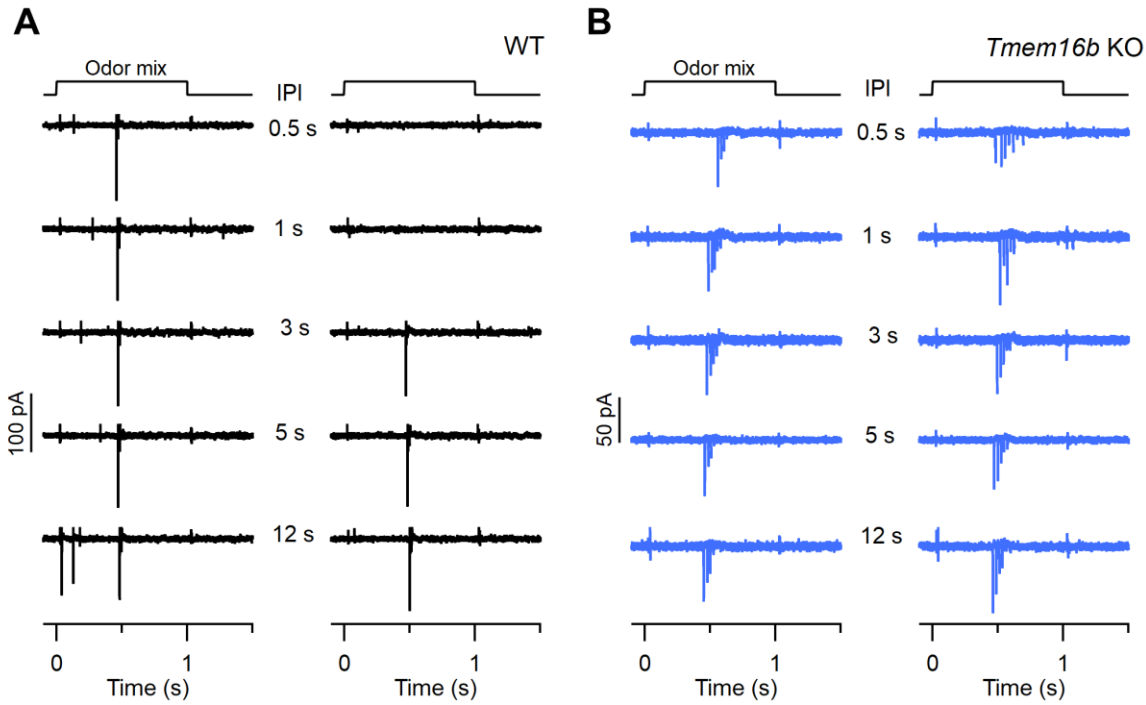


Figure 7. Odorant response in WT and *Tmem16b* KO mice. Representative loose-patch recordings of OSNs from WT (**A**) and Tmem16b KO (**B**) mice stimulated with an odor mix. Neurons were stimulated twice for 1 s with the indicated interstimulus interval (IPI). The opened/closed movement of the valves generates artifacts that is possible see in the figure.

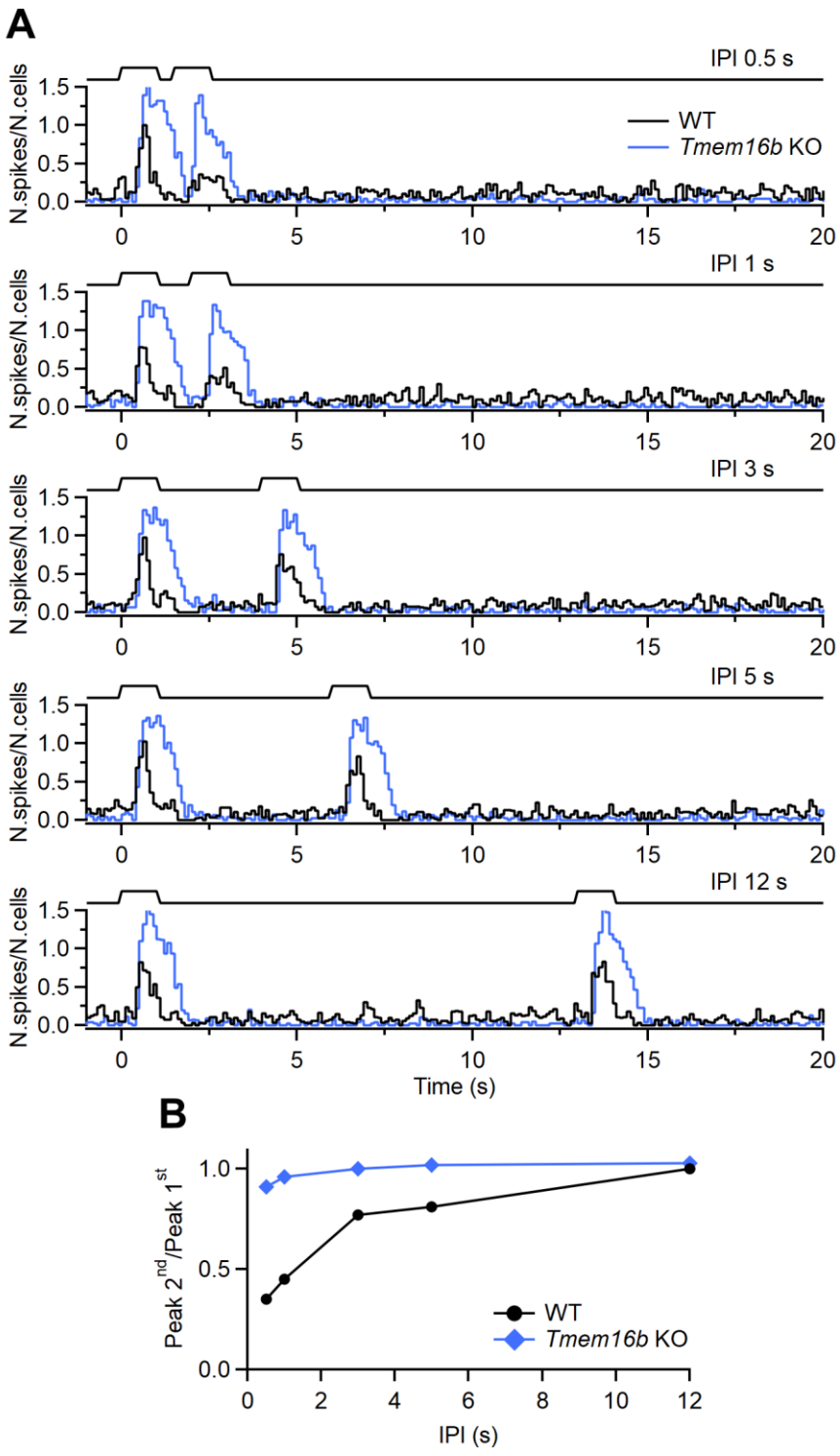


Figure 8. Double pulse odorant responses in WT and *Tmem16b* KO mice. (**A**) Peristimulus histograms showing the sum of number of spikes for all the cells normalized by the number of cells (bin= 100 ms). Neurons were stimulated twice for 1 s with the indicated interstimulus interval (IPI). (**B**) Ratio between number of spikes after the second and the first stimulation for different IPI.

5. Conclusions and discussion

In this thesis we investigated the role of TMEM16B in the mechanism of olfactory adaptation. The odorant bind to an odorant receptor, causes an increase in the intracellular concentration of cAMP and the activation of the CNG channels that induce a depolarizing influx of Na^+ and Ca^{2+} ions (Schild and Restrepo, 1998; Kleene, 2008). The high concentration of Ca^{2+} activates the Cl^- channels TMEM16B which amplify the transduction signal. OSNs support a high intracellular concentration of Cl^- (about 50 mM) that is similar to the concentration in the external environment (Reuter *et al.*, 1998). In these conditions, the opening of TMEM16B induces an outward current that enhances the depolarization of OSNs (Boccaccio and Menini, 2007). All the transduction machinery for odorant detection is localized in the cilia of OSNs.

In the olfactory system, adaptation is a fundamental process reducing the sensitivity to a stimulus to allow the detection of stimuli at increased intensities. OSNs adapt to repetitive odorant stimuli and it was shown that the main molecular mechanism for odorant adaptation occurs after the production of cAMP and is mediated by a negative feedback on cAMP-gated channels (Kurahashi and Menini, 1997).

5.1 Physiological role of TMEM16B in olfactory sensory neurons

By using electrophysiological experiments, we confirmed results of previous studies showing that the deletion of *Tmem16b* abolishes the contribution of chloride to the transduction current and that voltage-gated currents and membrane properties are not significantly different in OSNs from WT and *Tmem16b* KO mice (Figure 1; Billig *et al.*, 2011; Pietra *et al.*, 2016).
With extracellular loose patch recordings from OSNs, we measured the spontaneous spike activity and found that in the absence of TMEM16B, the mean frequency of the spontaneous action potential firing is lower than in WT and that the distribution of the ISI is shifted to higher values in *Tmem16b* KO compared to WT mice (Figure 2). Moreover, *Tmem16b* KO OSNs respond with a higher number of spikes upon stimulation with odorants- These data are in accordance with the results obtained by Pietra and colleagues (Pietra *et al.*, 2016).

In this work we also studied the responses of OSNs through EOG recordings by stimulating the olfactory epithelium with odorants in the vapor phase (Scott and Scott-Johnson, 2002). Comparison of EOG recordings from WT and *Tmem16b* KO mice have also been reported in 2011 by Billig and colleagues. They did not find differences comparing the amplitude of the response in WT and *Tmem16b* KO mice, but the results of their experiments showed a response of only few μV. Instead, in our experiments, the mean amplitude of the response is 10 mV in accordance with most previous studies (Zhao *et al.*, 1998; Song *et al.*, 2008; Cygnar *et al*., 2010; Coppola *et al.*, 2013; Antunes *et al*., 2014).

In our experiments we surprisingly found that the amplitude of the response is bigger in mice without the TMEM16B channel (Figure 3). Since EOGs measure the receptor potential a higher amplitude of the response is unexpected. Analyzing the response kinetics in detail, we found that the rise time and time constant of the recovery are shorter in *Tmem16b* KO mice (Figure 4). In agreement with our results, Neureither *et al*., (2017) reported that in *Tmem16b* KO mice, EOG recordings show a faster decay of the response, even if in their work the mean amplitude of the response is smaller compared to our experiments (only a few mV) (Neureither *et al.*, 2017). Moreover, it is worth noticing that the three different groups used different odorants to stimulate the olfactory epithelium.

We speculate that the response was faster in KO mice because of the lack of the amplification step mediated by TMEM16B and/or because TMEM16B mediates changes in ionic concentration of the mucus and its absence induces an increase of field response.

5.2 The role of TMEM16B in olfactory adaptation

Kurahashi and Menini in 1997 discovered that adaption is a process that mainly occurs downstream of the adenylyl cyclase and is regulated by a negative feedback by Ca^{2+}-CaM on the CNG channel. They performed electrophysiological experiments to investigate the role of the Ca^{2+} activated Cl^- channel in OSNs adaptation. They analyzed the falling phase of the response after an odorant stimulation in the presence of the Ca^{2+}-activated chloride channel blocker 4-acetamido-4'-isothiocyanato-stilbene-2,2'-disulphonic acid (SITS). Since they did not detect any

difference with and without the blocker, they concluded that the Ca^{2+} activated Cl^- channel is not involved in adaptation mechanism.

By using electrophysiological experiments, Boccaccio and colleagues (2006) reported other evidence that Ca^{2+}-activated Cl^- currents are not involved in the adaptation mechanism. In their experiments they changed the ionic conditions in order to avoid TMEM16B activation and found that adaptation is still present. They also activated the Ca^{2+} activated Cl^- channel through photolysis of caged Ca^{2+}, in which case they found that the currents after elicited pulse had similar amplitudes, suggesting that the Ca $^{2+}$-activated Cl^- channels are not involved in the adaptation process.

In our work using the genetic ablation of this channel we continued to investigate in detail the physiological role of TMEM16B in OSNs adaptation. We performed EOG and loose patch experiments and we delivered a protocol in which we presented odor twice with different interstimulus interval.

For the EOG recordings we quantified adaptation by calculating the ratio between the peak of the second response and the first response, and we found that at high odorant concentration the OE from *Tmem16b* KO recovered faster from adaptation (Figure 5). For loose patch experiments we analyzed the ratio of the number of spikes during the second and the first stimulation confirming that OSNs from *Tmem16b* KO mice recover faster from adaptation (Figure 8).

Differently from the results obtained by Kurahashi and Menini (1997) and by Boccaccio and colleagues (2006) our experiments suggest an involvement of TMEM16B in OSNs adaptation. There are some differences regarding these works. Kurahashi and Menini used dissociated OSNs from newts and the currents were recorded in the whole-cell voltage-clamp mode. Boccaccio *et al*., (2006), used dissociated OSNs from WT mice and the currents were recorded in the whole-cell voltage-clamp mode. In our work we used acute slices for *Tmem16b* KO and WT mice and we recorded in the extracellular loose patch configuration. In our configuration we recorded the action potentials, while they recorded the transduction currents in the whole-cell configuration. Another important difference is the length of the stimulation, our stimulation was longer compared to the stimulation performed in the other studies.

In our EOG experiments we also investigated the effect of a conditioning odorant pulse on a dose response curve in *Tmem16b* KO and WT mice. We found that in this condition, the amplitude of the response at all odor concentration in WT mice was significantly smaller. This suggests that the WT mice can discriminate better the two different stimuli while the signal in *Tmem16b* KO mice tend to be blurred.

This alteration can induce also behavioral deficit. It was shown that *Tmem16b* KO mice required more time to locate objects with unfamiliar odors until they learned to recognize them. In fact after training the differences between WT and *Tmem16b* KO mice disappeared (Neureither *et al*., 2017; Pietra *et al*., 2016).

To conclude, our experiments highlight the importance of the TMEM16B channel in the mechanisms that mediated OSN adaptation to repeated odorant pulses.

6. Manuscript under revision

6.1 Supporting cells of human olfactory epithelium co-express the lipid scramblase TMEM16F and ACE2 and may cause smell loss by SARS-CoV-2 Spike-induced syncytia.

Supporting Cells of the Human Olfactory Epithelium Co-express the Lipid Scramblase TMEM16F and ACE2 and May Cause Smell Loss by SARS-CoV-2 Spike-induced Syncytia.

Andres Hernandez-Clavijo[1,#], Kevin Y. Gonzalez-Velandia[1,#], Uday Rangaswamy[1], Giorgia Guarneri[1], Paolo Boscolo-Rizzo[2], Margherita Tofanelli[2], Nicoletta Gardenal[2], Remo Sanges[1], Michele Dibattista[3,*], Giancarlo Tirelli[2], Anna Menini[1,*]

[1]Neuroscience Area, SISSA, Scuola Internazionale Superiore di Studi Avanzati, Trieste, Italy [2]Department of Medical, Surgical and Health Sciences, Section of Otolaryngology, University of Trieste, Trieste, Italy

[3]Department of Basic Medical Sciences, Neuroscience and Sensory Organs, University of Bari A. Moro, Bari, Italy

[#]These authors contributed equally

*Corresponding authors:

Anna Menini

SISSA, Neuroscience Area

Via Bonomea 265,

Trieste, Italy

+39-0403787706

anna.menini@sissa.it

and

Michele Dibattista

Department of Basic Medical Sciences, Neuroscience and Sensory Organs,

University of Bari A. Moro,

Piazza Giulio Cesare 11.

Bari, Italy

michele.dibattista@uniba.it

Short Title: Human olfactory epithelium

Keywords: sustentacular cells, ANO6, human olfaction, scramblase

Abstract

Background/Aims: Quantitative and qualitative alterations in the sense of smell are well established symptoms of COVID-19. Some reports have shown that non-neuronal supporting (also named sustentacular) cells of the human olfactory epithelium co-express ACE2 and TMPRSS2 necessary for SARS-CoV-2 infection. In COVID-19, syncytia were found in many tissues but were not investigated in the olfactory epithelium. Some studies have shown that syncytia in some tissues are formed when SARS-CoV-2 Spike expressed at the surface of an infected cell binds to ACE2 on another cell, followed by activation of the scramblase TMEM16F (also named ANO6) which exposes phosphatidylserine to the external side of the membrane. Furthermore, niclosamide, an approved antihelminthic drug, inhibits Spike-induced syncytia by blocking TMEM16F activity. The aim of this study was to investigate if proteins involved in Spike-induced syncytia formation, i.e., ACE2 and TMEM16F, are expressed in the human olfactory epithelium. ***Methods:*** We analyzed a publicly available single-cell RNA-seq dataset from human nasal epithelium and performed immunohistochemistry in human nasal tissues from biopsies. ***Results:*** We found that ACE2 and TMEM16F are co-expressed both at RNA and protein levels in non-neuronal supporting cells of the human olfactory epithelium. ***Conclusion:*** Our results provide the first evidence that TMEM16F is expressed in human olfactory supporting cells and indicate that syncytia formation, that could be blocked by niclosamide, is one of the pathogenic mechanisms worth investigating in COVID-19 smell loss.

Introduction

The toll of the coronavirus disease 2019 (COVID-19) has been very high over the past two years. Since the beginning of the pandemic, various efforts have been made to identify the most common symptoms and among these the loss of chemosensory abilities has been identified as a predominant and frequently long-lasting symptom of this disease [1–6]. Although impairment in the sense of smell is common to other infectious respiratory diseases [7,8], it was surprising and unprecedented that both its onset and evolution were unrelated to other flu-like symptoms (or sometimes to any other symptom, as often smell loss was the only symptom) including nasal obstruction [5,9]. Indeed, an alteration in the sense of smell is used as part of routine screening for COVID-19 [10,11].

COVID-19 disease is caused by the severe acute respiratory syndrome coronavirus strain 2 (SARS-CoV-2), a positive-sense single strand RNA virus. The genome is composed of about 30 Kbp RNA and encodes for sixteen non-structural proteins, four structural proteins and eight accessory proteins [12]. Coronaviruses take their name from their electron micrographs showing several petal-shaped projections, called Spikes, that are reminiscent of the solar corona [13]. Spikes are glycoproteins protruding from the viral envelop and bind to their canonical human receptor Angiotensin Converting Enzyme 2 (ACE2) [14,15]. The fast pace of the research on the pathogenic mechanism of action of SARS-CoV-2 has given several clues on what happens when the virus enters in contact with host cells. The binding of the Spike protein with ACE2 determines virus-cell adhesion thus unleashing its fusion machinery to infiltrate the cell [16,17]. The Spike protein contains consensus sequences that could be further modified by host proteases furin and TMPRSS2. The furin is important to cleave the spike protein priming it for cell entry, then TMPRSS2 facilitates it by allowing a non-endosomal early entry of the virus [14,18,19].

It has been recently discovered that the SARS-CoV-2 Spike protein can cause fusion between cells and syncytia formation [17,20–27] and that a mutation in its receptor binding site impaired cell-to-cell fusion and syncytia formation [28]. For example, multinucleated pneumocytes were found in the lung of patients deceased for COVID-19 [20,29,30]. Recently, the TMEM16F protein, also named ANO6, has been shown to be involved in syncytia formation. TMEM16F is a calcium-activated scramblase and ion channel [31–34] that is responsible for exposing phosphatidylserine from the cytofacial to the exofacial leaflet of the plasma membrane and can therefore act as signaling molecule for cell-to-cell fusion [25,30,35,36]. In addition, the same mechanism has been proposed to enhance platelet pro-coagulant activity [22].

As the molecular mechanisms underlying the olfactory disfunction in COVID-19 are still largely unknown, we asked whether SARS-CoV-2 Spike protein could trigger syncytia formation in the human olfactory epithelium. The olfactory epithelium is a pseudo-stratified epithelium consisting of different cell types

(Figure 1 A) [37–39]. The functional units expressing odorant receptors are the bipolar olfactory sensory neurons which bear several apical cilia protruding in the nasal cavity and contain the molecular components for odorant transduction. These neurons are surrounded, basically enwrapped by supporting cells, also named sustentacular cells, a columnar-like type of cells. Stem cells (horizontal and globose basal cells) are located at the base of the olfactory epithelium [39–41]. These basal cells are pluripotent and replace both supporting cells and olfactory sensory neurons constituting a neurogenic niche able to regenerate the human olfactory epithelium [42]. Previous work has shown that supporting cells and basal cells, but not olfactory sensory neurons, express both ACE2 and TMPRSS2 that allow SARS-CoV-2 entry into these cells [43–45]-

To investigate if ACE2 and TMEM16F, the molecular components necessary for syncytia formation, are co-expressed in cells of the olfactory epithelium, we analyzed a single-cell RNA-seq (scRNA-seq) dataset from human nasal epithelium [42] and performed immunohistochemistry in human nasal tissues from biopsies. We found that ACE2 and TMEM16F are co-expressed both at RNA and protein levels in non-neuronal supporting cells. We propose that one of the pathogenic mechanisms behind smell loss could be syncytia formation of supporting cells initiated by Spike binding to ACE2 and mediated by TMEM16F.

Materials and Methods

Single-cell RNA sequencing data analysis

The single-cell RNA-seq dataset was downloaded from NCBI GEO: GSE139522 and wa related to the study by Durante et al. [42]. The dataset consists of single cell 3' RNAseq of the olfactory epithelium from 2 individuals and respiratory epithelium from other 2 individuals. Individuals involved in this study were aged between 41 and 52 years. Tissue for sequencing was obtained while undergoing transnasal endoscopic surgery. 10X Genomics Chromium platform and Illumina Nextseq 500 technology was used for sequencing. The data was analysed in R version 4.1.2 using the Seurat R package version 4.1.0 [46–48], a widely used toolkit for quality control, analysis and exploration of single cell RNA sequencing data. The procedures described in Durante et al. [42] with minimal modifications were used for analysing this dataset.

The raw gene-barcode matrix of all 4 patients were loaded into R using Read10X() function of Seurat. A Seurat object was created for each individual data using the CreateSeuratObject() function. PercentageFeatureSet() function was used to calculate the percentage of mitochondrial gene counts for each Seurat object. Cells that had UMI > 400, between 100-8000 expressed genes and mitochondrial content less than 10% were defined as high-quality cells and considered for downstream analysis. This filtering resulted in a total of 29628 cells across all 4 Seurat objects.

The filtered Seurat objects were merged using the merge() function provided by the Seurat package. Each individual data was separated using the SplitObject() function. The raw UMI count of the genes within each cell was normalized by the total number of UMI counts per cell, scaled to 10^4 and natural log transformed using the NormalizeData() function for each dataset. The top 5000 variable genes were identified for each dataset using FindVariableFeatures() function, with variance stabilizing transformation (vst) as the selection method. This was followed by identifying the anchor genes using the FindIntegrationAnchors() function with default parameters. It returned the top 5000 variable genes shared across the 4 datasets. The datasets were integrated into a single Seurat object using the IntegrateData() function with default parameters.

The integrated data was scaled and reduced to 30 principal components (PCs) using the ScaleData() and RunPCA() function of Seurat. These PCs were passed as input to the RunUMAP() function. Clustering was done using FindNeighbors() and FindClusters() functions using the 30 PCs and a resolution parameter of 0.5 which resulted in 27 Louvain clusters. The clustering results were visualized in a two-dimensional UMAP representation produced using the DimPlot() function. The clusters were annotated based on the expression of the canonical marker genes for different cell types as mentioned in Durante et al. The

AddModuleScore() and FeaturePlot() functions were used to visualize the expression of the canonical marker genes to annotate the clusters. Multiple clusters were annotated as one cell type when the expression of the marker genes for that cell type was highly expressed in multiple clusters. When the expression of marker genes for more than one cell type was found to be highly expressed in a single cluster, that cluster was annotated to contain multiple cell types. By doing so, 27 clusters were further reduced to 21 clusters. The following cell type pairs were identified within the same cluster: olfactory and respiratory HBCs (cluster 0), fibroblasts and stromal cells (cluster 1), macrophages and dendritic cells (cluster 11), mature and immature neurons (cluster 15). On the contrary, the following cell types were identified in more than one cluster: supporting cells (also named sustentacular cells cluster 3 and 10), pericytes (cluster 4 and 6), bowman's glands (cluster 12, 16 and 17), plasma cells (cluster 13 and 19) and olfactory HBCs/respiratory HBCs (cluster 0 and 26). The number of cells present in each cluster and cell type is contained in Supplementary Table 1 and 2.

Human nasal tissue

Samples from human nasal tissue were obtained at the Section of Otolaryngology of the Department of Medical, Surgical and Health Sciences, University of Trieste, Trieste, Italy, with the written informed consent of each patient for participation in this study, which was approved by the Ethics Committee on Clinical Investigation of the University of Trieste (nr 232/2016 and 110/2021).

Biopsies and nasal brushing were performed in the operating room from patients under general anesthesia at the end of the scheduled endoscopic sinonasal surgery. Two-three biopsy specimens were obtained from one nostril from the superior septum within the olfactory cleft and adjacent to the middle turbinate using a sickle knife and Blakesley forceps or cupped forceps. Samples were obtained from 8 patients (6 males and 2 females, age between 24 and 75 years). Both olfactory and respiratory epithelium were found in 2 biopsies, only olfactory epithelium in 2 biopsies, and only respiratory epithelium in 4 biopsies. Once collected, specimens were immediately fixed in paraformaldehyde (PFA) at 4% in PBS pH 7.4 for 4 to 10 hours at 4 °C. After fixation, the tissue was kept in PBS pH 7.4 at 4 °C, typically from 2 to 24 hours. Nasal brushings were performed with FLOQSwabs® (COPAN, Italy) swab sampling brush consisting of a molded plastic shaft and a tip coated with perpendicular short Nylon® fibers. The swab was gently moved back and forward and rotated in the olfactory cleft of the nostril opposite the one where the biopsy was taken. After nasal brushing, the swab tip was immersed in PFA at 4% in PBS pH 7.4 for 2 hours for cell fixation and then was kept in PBS pH 7.4 at 4 °C, typically from 2 to 24 hours. Although nasal brushings were taken from the olfactory cleft, we could not observe cells from the olfactory epithelium but only cells from the respiratory epithelium.

Immunohistochemistry and Immunocytochemistry

For cryoprotection of biopsies, the tissue was equilibrated overnight in 30% (w/v) sucrose in PBS at 4 °C. Then, the tissue was embedded in cryostat embedding medium (BioOptica) and immediately frozen at −80 °C. 16 µm sections were cut on a cryostat and mounted on Superfrost Plus Adhesion Microscope Slides (ThermoFisher Scientific). Sections were air-dried for 3 hours and used the same day or stored at -20 °C for later use. Cryostat embedding medium was removed from the tissue by incubating the slices in PBS for 15 minutes. The tissue was treated for 15 minutes with 0.5 % (w/v) sodium dodecyl sulfate (SDS) in PBS for antigen retrieval, then washed and incubated in blocking solution (5% normal donkey serum, 0.2% Triton X-100 in PBS) for 90 minutes and finally incubated overnight at 4 °C with the primary antibodies diluted in blocking solution. In the following day, the unbound primary antibodies were removed with PBS washes, then sections were incubated with Alexa Fluor conjugated secondary antibodies (1:500 dilution) in TPBS (0.2% Tween 20 in PBS) for 2 hours at room temperature, washed and mounted with Vectashield (Vector Laboratories) or FluoromontG (ThermoFisher). DAPI (5 mg/ml) was added to the solution containing secondary antibody to stain the nuclei. For nasal brushings, the tip of the swab was transferred into a 2 ml tube and treated for 10 minutes with 0.5 % (w/v) SDS in PBS for antigen retrieval, then the same procedure used for tissue slices was followed until washout of the secondary antibody. Cells were then detached from the swab by gentle agitation and by passing the swab through a 200 µl micropipette tip with the extreme end removed as in Scudieri et al. (2020) (Scudieri et al., 2020). Cells were collected and plated in a µ-Slide 8 Well Grid-500 (Ibidi, Germany) and observed under confocal microscopy Nikon A1R (Nikon, Japan). During immunocytochemical analysis from nasal brushings, we observed several respiratory cells but we did not detect any olfactory sensory neuron.

The following primary antibodies (dilution; catalogue number, company) were used: polyclonal goat anti-OMP (1:1000; 019-22291, Wako), monoclonal mouse anti-β Tubulin III (TUJ1) (1:200; 801202, BioLegend), monoclonal mouse anti-β Tubulin IV (BT4) (1:1000; T7941, Sigma), polyclonal rabbit anti-ERMN (1:200; NBP1-84802, Novus), polyclonal rabbit anti-KERATIN 5 (K5) (1:200; 905501, BioLegend), polyclonal goat anti-ACE2 (1:200; PA5-47488, Invitrogen), polyclonal rabbit anti-ACE2 (1:200; ab15348, Abcam), polyclonal rabbit anti-TMEM16F (1:200; provided by Lily Jan University of California, San Francisco, CA, USA; [49]).The following secondary antibodies were used: donkey anti-rabbit Alexa Fluor Plus 594 (1:500; A32754, Life Technologies), donkey anti-rabbit Alexa Fluor 488 (1:500; A21206, Life Technologies), donkey anti-goat Alexa Fluor 488 Plus (1:500; A32814, Life Technologies), donkey anti-mouse Alexa Fluor 594 (1:500, A-21203, Life Technologies), donkey anti-mouse Alexa Fluor 488 (1:500, A32766, Life Technologies). Control experiments, excluding primary antibodies, were performed for each immunolocalization and shown in supplementary Figure S2.

Immunostaining for human tissue was performed on all olfactory and respiratory epithelia available to confirm findings. We performed at least 2 independent human tissue replicates for each antibody tested. All attempts at replication were successful.

Image acquisition

Z-stack images were acquired using NIS-Elements Nikon software at 1024 ×1024 pixels resolution of each single image and analyzed with ImageJ software (National Institute of Health, USA). Max projections of Z-stacks or individual images within the stacks were used to display results. Figure assembly was performed on ImageJ (National Institutes of Health) using ScientiFig plugin [50]. No image modification was performed other than brightness and contrast adjust.

Results

In the hunt for a possible pathophysiological mechanism for SARS-CoV-2 induced smell loss, we sought to investigate whether TMEM16F, a calcium-dependent ion channel and scramblase, recently involved in SARS-CoV-2 spike-induced syncytia, is expressed in the human nasal tissues and whether its expression pattern resembles that of ACE2. We reasoned that if ACE2 and TMEM16F are co-expressed in the same cell type, then it may have the molecular components necessary to trigger syncytia formation.

Main cell types in the human olfactory and respiratory epithelium

By taking advantage of the available single-cell RNA sequencing (scRNA-seq) dataset of the human olfactory and respiratory epithelium of Durante et al. (2020) [42], we performed a standard analysis using uniform manifold approximation and projection (UMAP) and identified clusters of several cell types (Figure 1B). Cell types included olfactory sensory neurons, olfactory supporting cells and basal cells for the olfactory epithelium, while for the respiratory epithelium cell types included respiratory ciliated cells, secretory cells and basal cells. By immunohistochemistry, we used specific markers to identify some of these cells in biopsies of human nasal tissues obtained from patients undergoing endoscopic nasal surgery. For the respiratory epithelium, we used an antibody against β-tubulin IV (BT4), a marker of the cilia of respiratory ciliated cells [51]. For the olfactory epithelium, we used β-tubulin III (TUJ1) to stain neurons, the olfactory marker protein (OMP) to identify mature olfactory sensory neurons, keratin 5 (K5) for horizontal basal cells [51,52], and ERMN for supporting cells [44,53].

Figure 1C shows the boundary between the olfactory and the respiratory epithelium with mature olfactory sensory neurons marked by OMP (red) and the cilia of respiratory ciliated cells stained by β-tubulin IV (BT4, green). To distinguish between zones of olfactory and respiratory epithelium, we also visualized neurons using TUJ1 (Figures 1D-E). The transition zone between the two epithelia showed the passage from the olfactory neuroepithelium to the neuron-less respiratory epithelium. Basal cells were identified by keratin 5 and showed a pearl necklace-like staining pattern not only at the base of the olfactory but also of the respiratory epithelium (Figure 1D). To visualize supporting cells, we used ERMN a marker which labels the apical part of supporting cells. Figure 1E confirmed that ERMN apical expression pattern did not co-localize with that of the neuronal marker TUJ1, indicating that we could indeed use ERMN to exclusively visualize olfactory supporting cells.

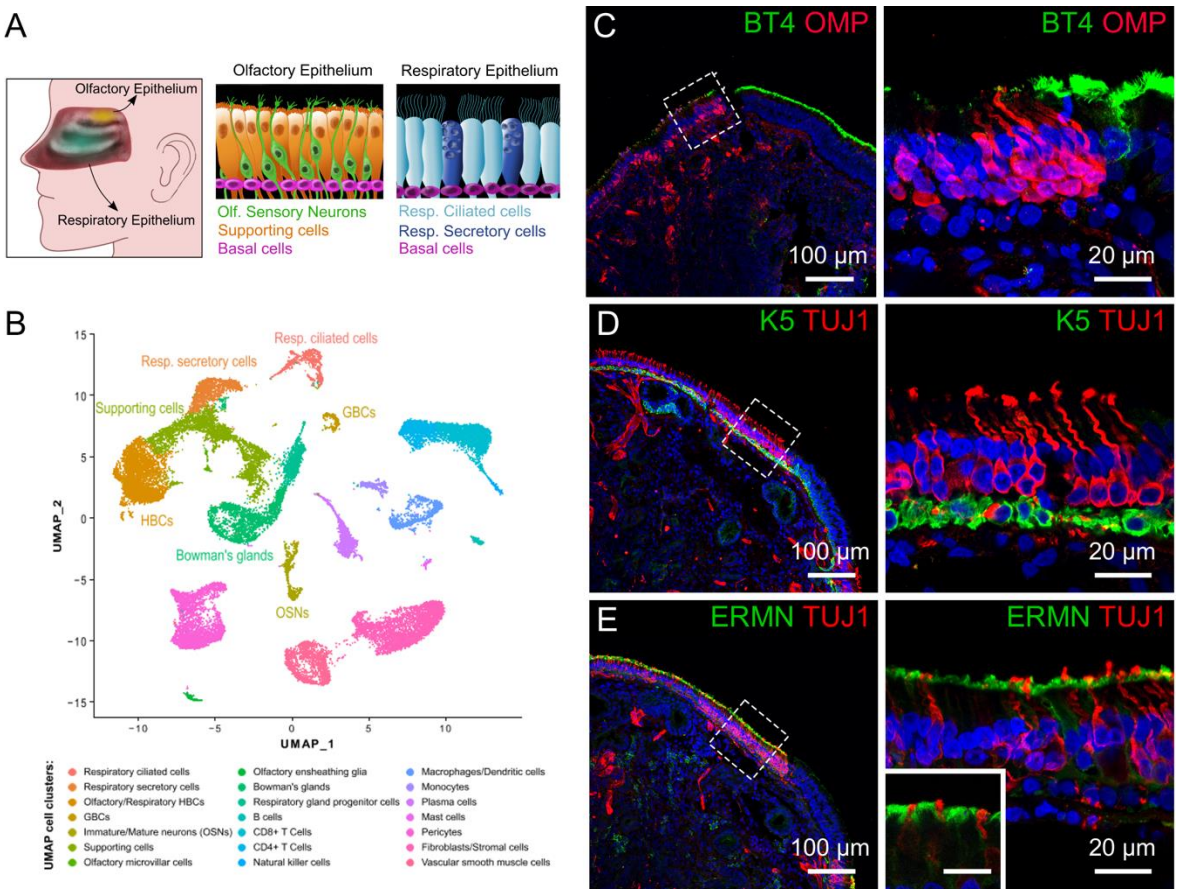


Fig. 1. Main cell types in the human olfactory and respiratory epithelium. (A) Schematic representation of the main cell types of the respiratory epithelium and olfactory epithelium. (B) Visualization of the clustering results from the scRNA-seq data produced in Durante et al. (2020) on a uniform manifold approximation and projection (UMAP) plot. The cell type annotation of each cluster is noted on the color key legend and labels. (C-E) Confocal images of sections of human nasal epithelium. β-tubulin IV (BT4) is a marker for the cilia of respiratory ciliated cells (green) and OMP for mature olfactory sensory neurons (red) (C). β-tubulin III (TUJ1) is a marker for neurons (red) and Keratin 5 (K5) for basal cells both in the respiratory and olfactory epithelium (green) (D). ERMN is a marker for the apical part of olfactory supporting cells (green) and does not co-localize with the neuronal marker TUJ1 (red) (E). Higher magnification images taken from the dashed squares are shown in the right columns (C-E). At low magnification (left panels in C-E), the transition zone between olfactory and respiratory epithelium is clearly observed. The respiratory epithelium can easily be distinguished by BT4 expression, while the olfactory epithelium is marked by OMP, TUJ1 or ERMN. Inset scale bar in the right panel in (E) is 10 µm. Cell nuclei were stained with DAPI (blue).

ACE2 transcript and protein expression

As ACE2 is relevant for SARS-CoV-2 Spike binding, we first identified which cells express *ACE2* transcript. In our UMAP analysis we could identify cells expressing *ACE2* in specific populations of the nasal tissue (Figures 2A-B). We observed *ACE2* expression in several olfactory supporting cells, horizontal basal cells, secretory and ciliated respiratory cells, whereas we could not identify *ACE2* expression in olfactory sensory neurons in the scRNA-seq data. We then evaluated the expression and localization of the ACE2 protein in the human nasal cavity by fluorescence immunohistochemistry. In the respiratory epithelium (apically stained by β-tubulin IV), ACE2 was expressed in many respiratory cells including basal cells lying the basal lamina (Figure 2C). Moreover, as nasal brushing produced many isolated respiratory cells (but not olfactory cells), we performed immunocytochemistry to clearly identify protein localization and found that most isolated ciliated respiratory cells (marked by β-tubulin IV) also expressed ACE2 (Figure 2D). However, we did not observe co-localization of ACE2 and the ciliary marker β-tubulin IV but a rather basolateral ACE2 expression and mostly mutually exclusive with β-tubulin IV*,* indicating that ACE2 is not expressed in the apical cilia. Transcriptomic analysis indicates that *ACE2* is also expressed in respiratory secretory cells (Figures 2A-B), which do not have an apical ciliary tuft. In our immunocytochemistry experiments several cells morphologically resembling secretory cells also expressed ACE2 but we did not further characterize them with specific markers (Figure 2C).

Figures 2E and F show that ACE2 staining in the olfactory epithelium was mutually exclusive with TUJ1, resembling the mutually exclusive expression of TUJ1 and ERMN (Figure 1E), thus validating the transcriptomic results that show expression of *ACE2* in supporting cells and lack of signal in olfactory neurons (Figures 2A-B). ACE2 was mainly concentrated in the apical half of the supporting cells and it surrounded the TUJ1 positive neuronal dendrites and knobs (Figures 2E-F). ACE2 was also localized to the basal part of the epithelium indicating that it is also expressed in olfactory basal cells (Figure 2E, see also Figures 4C-D).

In summary, we confirmed that ACE2 is expressed both in the human respiratory and olfactory epithelium where it is mainly found in supporting and basal cells but not in neurons.

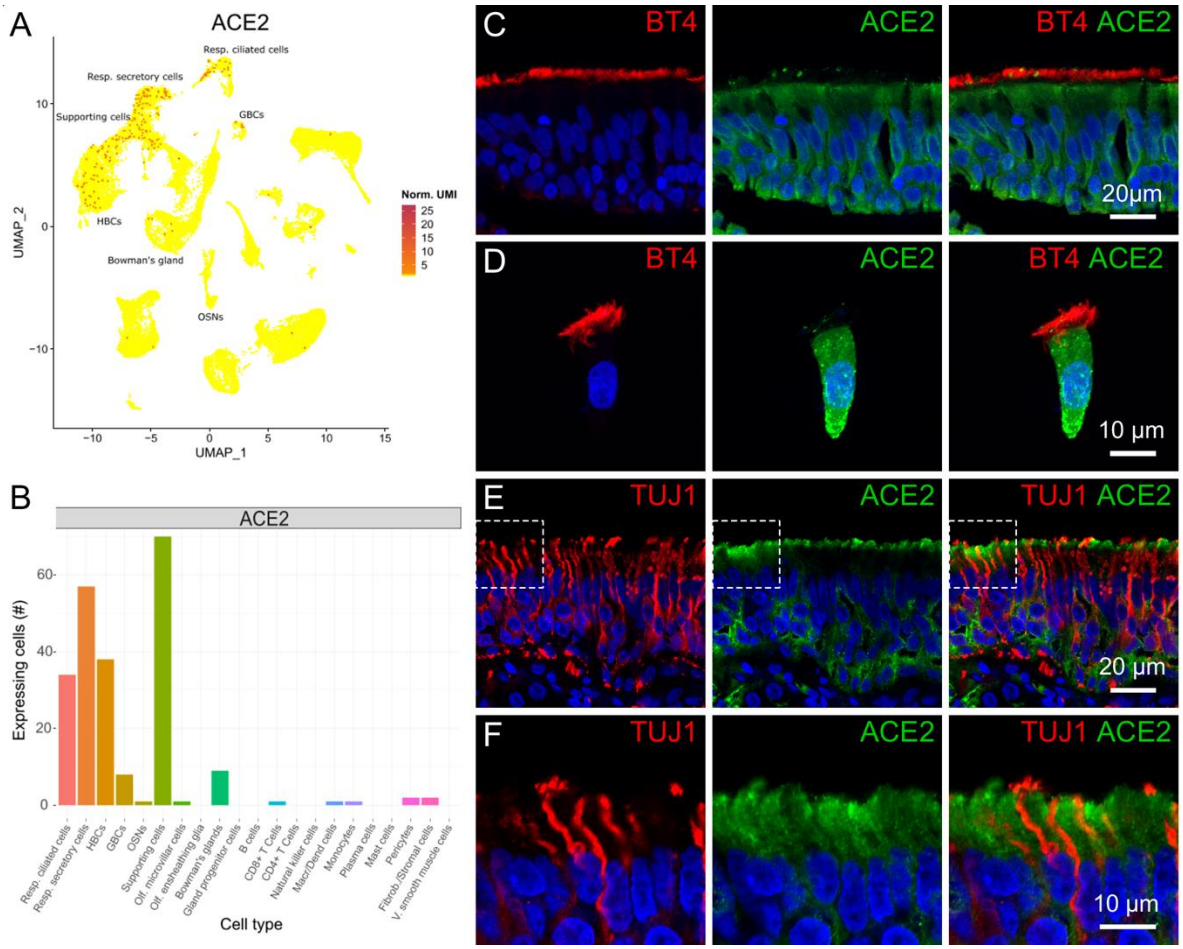


Fig. 2. ACE2 transcript and protein expression. (A) Normalized expression levels of *ACE2* shown on the UMAP plot. (B) Bar plot displaying the number of different cell types expressing *ACE2*. (C) Section of human respiratory epithelium immunostained for BT4 (red) and ACE2 (green). (D) A dissociated respiratory ciliated cell immunostained for BT4 (red) and ACE2 (green) showing that ACE2 is highly expressed in the cell except in the cilia. (E-F) Sections of human olfactory epithelium immunostained for TUJ1 (red) and ACE2 (green). Higher magnification images taken from the dashed squares in (E) are shown in (F). ACE2 is expressed in basal and supporting cells but not in neurons (F). Cell nuclei were stained with DAPI (blue).

TMEM16F transcript and protein expression

As TMEM16F has been shown to be involved in SARS-CoV-2 Spike-induced syncytia formation in several cells and tissues [20,35], we investigated the expression of TMEM16F and described for the first time the expression and localization of TMEM16F in the human respiratory and olfactory epithelium.

Transcriptomic analysis indicated that *TMEM16F* is expressed in several cell types of the nasal tissue (Figures 3A-B), especially in respiratory secretory and ciliated cells and in olfactory supporting cells. Immunohistochemistry confirmed the expression of TMEM16F in several cells of the respiratory epithelium (Figure 3C). In the olfactory epithelium, we also found staining of TMEM16F with higher intensity at the apical side (Figures 3D-E). Similarly to ACE2 (Figures 2E-F), TMEM16F did not co-localize with the neuronal marker TUJ1 indicating the lack of expression in olfactory sensory neurons (Figures 3D-E). Figure 3E clearly shows apical dendrite/knob regions of three neurons marked with TUJ1 but not stained for TMEM16F. The expression pattern of TMEM16F resembles that of ERMN that intensely stains the apical portion of supporting cells (Figures 1E and 3E). We also imaged tangential/oblique sections of the olfactory epithelium to better visualize the intriguing pattern of TMEM16F expression: Figure 3F shows that round/oval shaped structures marked by TMEM16F (green) surround the knobs of olfactory sensory neurons marked by TUJ1 (red), further showing the expression of TMEM16F in non-neuronal cells. Furthermore, the antibody against TMEM16F marked several glandular cells, most likely belonging to Bowman's glands, beneath the basal lamina of the olfactory epithelium (Figures 3D and 4C).

In summary, we showed that TMEM16F is expressed both in the human respiratory and olfactory epithelium where it mostly localizes in the apical region of supporting cells with a pattern similar to that of ERMN.

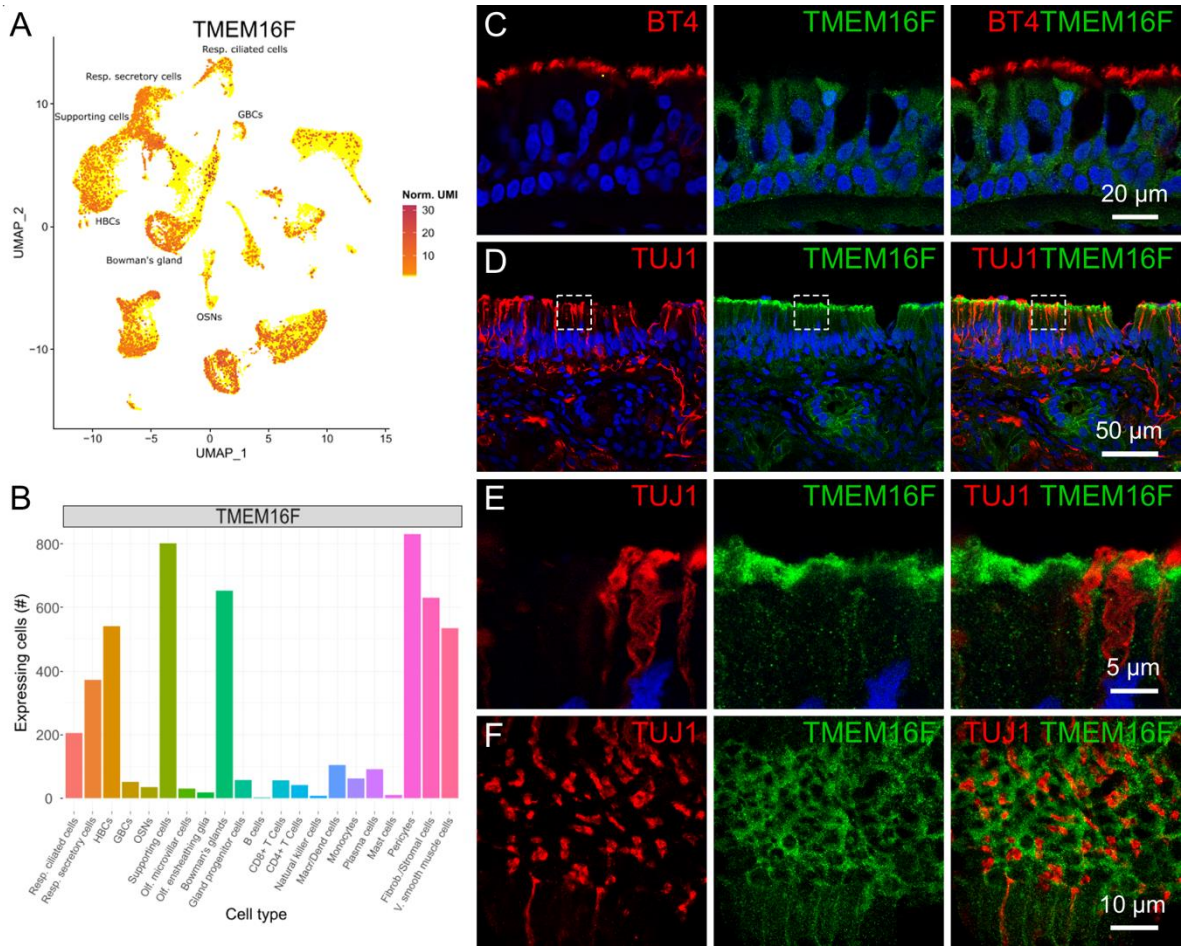


Fig. 3. TMEM16F transcript and protein expression. (A) Normalized expression levels of *TMEM16F* shown on the UMAP plot. (B) Bar plot displaying the number of different cell types expressing *TMEM16F*. (C) Section of human respiratory epithelium immunostained for BT4 (red) and TMEM16F (green). TMEM16F shows a faint but consistent expression in most cells of the respiratory epithelium. (D) Section of human olfactory epithelium immunostained for TUJ1 (red) and TMEM16F (green). TMEM16F is highly expressed in the apical region of the olfactory epithelium and in cells of secretory glands. (E) High magnification images of the apical region of the olfactory epithelium taken from the dashed squares in (D). TMEM16F stains the apical region of supporting cells and do not show co-localization with the neuronal marker TUJ1. The staining of TMEM16F at the apical region is similar to ERMN expression pattern shown in Figure 1E. (F) En-face view of a section of olfactory epithelium stained with TUJ1 (red) and TMEM16F (green). TMEM16F shows no co-localization with the neuronal marker TUJ1. Cell nuclei were stained with DAPI (blue). See also Figure S2.

TMEM16F and ACE2 co-expression in supporting cells of the olfactory epithelium

To better evaluate the co-expression levels of *ACE2* and *TMEM16F* in different cell types, we plotted the mean expression levels for each cell type (Figure 4A) and the number of cells expressing both transcripts (Figure 4B). Olfactory supporting cells, respiratory ciliated and secretory cells showed the highest correlated expression levels for *ACE2* and *TMEM16F*.

Immunohistochemistry experiments on the olfactory epithelium using ACE2 and TMEM16F antibodies showed the co-localization of the two proteins at the apical side of the epithelium. Figures 4C and D (left panels) clearly confirm ACE2 staining in the upper portion of the olfactory epithelium and in the basal side, similarly to results shown in Figure 2E obtained with a different antibody. TMEM16F also localized to the apical side of the olfactory epithelium, with some staining more distal than that of ACE2.

All together, these results strengthen the possibility that SARS-CoV-2 Spike protein could bind to ACE2 and produce the activation of TMEM16F in the same cell with subsequent cell-to-cell fusion. It has also been shown that interferon-induced transmembrane proteins inhibit Spike-induced cell-to-cell fusion whereas TMPRSS2 accelerates Spike-mediated syncytia and counteracts the inhibitory effect of the interferon-induced transmembrane proteins [21]. Here, we evaluated the co-expression levels of *TMPRSS2*, *ACE2* and *TMEM16F* in different cell types (Figures S1A-D) and found that olfactory supporting cells, respiratory ciliated and secretory cells show the highest correlated expression levels for the three genes, indicating that syncytia could be formed also if interferon is released by cells infected by SARS-CoV-2.

In summary, we showed that TMEM16F is co-expressed with ACE2 at the apical part of human olfactory supporting cells and could be contributing to cell-to-cell fusion induced by Spike binding to ACE2. Syncytia formation by supporting cells could cause olfactory dysfunctions.

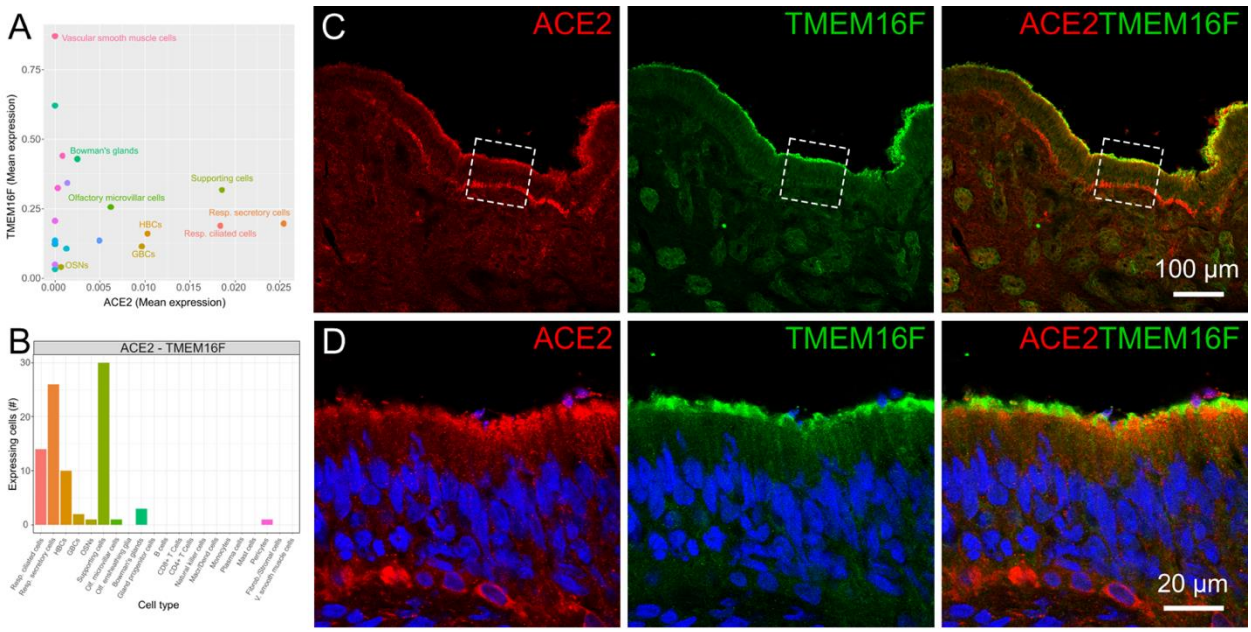


Fig. 4. TMEM16F and ACE2 co-expression in supporting cells of the olfactory epithelium**. (**A) Co-expression of *ACE2* and *TMEM16*F in the different cell clusters. Mean normalized expression levels are plotted. (B) Bar plot displaying the number of cells co-expressing *ACE2* and *TMEM16F* in each cluster. (C) Section of human olfactory epithelium immunostained for ACE2 (red) and TMEM16F (green). ACE2 and TMEM16F are co-expressed in the apical region of supporting cells of the olfactory epithelium. (D) High magnification images of the apical region of the olfactory epithelium taken from the dashed squares in (C). Cell nuclei were stained with DAPI (blue).

Discussion

It has recently been shown that SARS-CoV-2 pathogenic mechanisms include the formation of syncytia in several cellular models and in tissues biopsies from COVID-19 patients [20,21,24,25,30,54]. Some studies have shown that the molecular pathway that leads to syncytia formation after the binding of SARS-CoV-2 Spike to ACE2 involves TMEM16F [20,35,55]. As the molecular mechanisms underlying dysfunctions of the sense of smell in COVID-19 are still largely unknown, we sought to set a working hypothesis for SARS-CoV-2 pathogenesis in the olfactory epithelium that includes the possibility of syncytia formation. Our results provide the first demonstration that TMEM16F is co-expressed with ACE2 in the human olfactory epithelium at the apical part of olfactory supporting cells. Thus, the molecular machinery necessary to induce cell fusion upon binding of Spike is present in the supporting cells of the olfactory epithelium and may constitute a possible mechanism damaging the olfactory epithelium and producing dysfunctions in the sense of smell.

TMEM16F is a very intriguing transmembrane protein that functions both as calcium-activated lipid scramblase and ion channel [31–34,49,56]. TMEM16F as scramblase has been shown to promote platelet association and cell-to-cell fusion [20,49,57]. The activation of TMEM16F caused by the SARS-CoV-2 Spike protein has been shown to be relevant for COVID-19 pathogenesis. It prompts pro-coagulant activity in platelets via lipid scrambling promoting thrombin formation, thus causing SARS-CoV-2-induced thrombosis [22,35]. In the alveoli, TMEM16F promotes SARS-CoV-2-Spike mediated syncytia formation by exposing phosphatidylserine on the outer leaflet of plasma membrane [20,30,35,36]. At least two possible mechanisms have been hypothesized for the activation of TMEM16F by Spike [20,22,25]: TMEM16F could be directly activated upon binding of Spike to ACE2 in the same cell, or TMEM16F could be activated by an induced increase in intracellular calcium. Activation of the scramblase TMEM16F then causes phosphatidylserine insertion on the outer leaflet of the plasma membrane, which is the signal for cell-to-cell fusion.

Although olfactory impairments are well documented during and post COVID-19 [1–6] the pathophysiological mechanisms are still largely elusive. Contrary to other forms of olfactory dysfunction associated with respiratory viral infections [58], a nasal mucosal oedema obstructing the olfactory cleft and leading to a conductive loss could explain only a small fraction of the cases of smell alteration caused by COVID-19. In fact, nasal obstruction and an altered sense of smell have been observed to be frequently dissociated symptoms also during the acute phase of COVID-19 [9,59].

Supporting cells are the primary target of SARS-CoV-2 in the olfactory epithelium [43–45,60–62] and we have shown here that they co-express ACE2 and TMEM16F and could therefore form Spike-induced

syncytia that may contribute to a prolonged smell loss. Indeed, although olfactory sensory neurons do not appear to be directly affected by SARS-CoV-2, it is important to note that olfactory supporting cells do not simply surround the dendrites of olfactory sensory neurons but they enwrap the dendrites, especially when neurons become mature, forming a cell-in-cell structure with olfactory sensory neurons [53,63,64]. Thus, if supporting cells form syncytia, also the functionality of olfactory sensory neurons is likely to be compromised.

Another possible scenario involves TMEM16F working as a calcium-activated nonselective ion channel. Indeed, we have shown here that TMEM16F is localized in the distal apical part of supporting cells that is in contact with the mucus layer in the nasal cavity. The mucus composition is very important to maintain the ionic gradients involved in transducing odorant binding to the receptor in the cilia of olfactory sensory neurons into action potentials sent to the brain. Thus, if TMEM16F is activated as ion channel, it may modify the mucus ionic composition as it is permeable to various ions, including chloride, calcium and sodium [34,49,65–70]. In humans (as well as in mice), the cyclic nucleotide-gated channel A2 (CNGA2) has a crucial role in olfactory signal transduction [71,72] and a reduction of the inward transduction current carried by calcium and sodium ions through CNG channels of olfactory sensory neurons may decrease the odorant response [73–76]. In addition, in human olfactory sensory neurons the chloride current via the calcium-activated chloride channel TMEM16B/ANO2 [77,78] may participate in odorant transduction, and therefore an alteration of the chloride ion gradient that reduces the odorant-induced current, may decrease olfactory neurons sensitivity and ultimately cause smell impairments, as it occurs in mice [78–82].

Although some reports did not find signs of inflammatory response in the olfactory cleft [83,84], a recent study showed the presence of sustained inflammation in the olfactory epithelium and olfactory bulb [62]. It is known that interferon-induced transmembrane proteins inhibit Spike-induced cell-to-cell fusion but it has also been reported that TMPRSS2 counteracts this inhibitory activity by significantly increasing Spike protein syncytia formation [21,24,25]. Thus, human olfactory supporting cells have all the molecular components necessary to promote viral infection, replication and syncytia formation also in the presence of inflammation. In addition, several transcriptomic signatures implicate T-cell recruitment [62], but it has been shown that Spike-mediated syncytia can also internalize various T-cell lines causing their death by deterioration of their plasma membrane [25,30].

To our knowledge, syncytia were overlooked in the few published reports about respiratory and olfactory epithelium in COVID-19 patients and therefore, at present, there is no evidence of syncytia formation in nasal epithelia. However, the presence of syncytia has been demonstrated in air-liquid interphase cultures of cells brushed from the nose and infected with SARS-CoV-2 (Fig. 1 of Capraro et al., 2021 [85]). In agreement with previous studies indicating that the nasal respiratory epithelium is one of the primary targets of SARS-CoV-2 [86,87], we found that ACE2 is expressed in respiratory cells. In addition, we showed

that both TMEM16F and ACE2 are expressed in the respiratory epithelium, where they may promote cell-to-cell fusion. It should also be considered, though, that syncytia in various tissues were observed only in the severe stages of the disease in COVID-19 patients and may not be present in mild cases [20,88].

Conclusion

Our results provide the first evidence that TMEM16F and ACE2 are co-expressed in human olfactory supporting cells and indicate that the loss of smell in COVID-19 may be due also to syncytia formation. TMEM16F is a target for commercially available drugs, such as niclosamide [20,89], and some lipid-targeting drugs disrupt Spike-mediated membrane fusion [17]. Thus, it may be worth pursuing the possibility to target some of these drugs directly to the nasal epithelia to at least mitigate the olfactory impairments experienced during COVID-19.

Acknowledgements

We thank Dr. Lily Jan (UCSF) for providing the antibody against TMEM16F.

Author contributions

A.H.C, K.G.V. performed immunohistochemistry and confocal microscopy with the help of G.G., P.B.R., M.T., N.G. and G.T. collected human biopsies, U.R. and R.S performed scRNA-seq data analysis, A.M., M.D. and A.H.C. conceptualized the project and designed experiments, M.D. and A.M. wrote the manuscript with comments from all the other authors.

Funding

This work was funded by the Italian Ministry of Education, University and Research 2010599KBR (A.M.).

Statement of Ethics

Subjects have given their written informed consent and the study protocol has been approved by the Ethics Committee on Clinical Investigation of the University of Trieste (nr 232/2016 and 110/2021).

Disclosure Statement

The authors declare they have no conflict of interests.

References

[1] Boscolo-Rizzo P, Menegaldo A, Fabbris C, Spinato G, Borsetto D, Vaira LA, et al. Six-Month Psychophysical Evaluation of Olfactory Dysfunction in Patients with COVID-19. Chemical Senses 2021;46:bjab006. https://doi.org/10.1093/chemse/bjab006.

[2] Cecchetto C, Di Pizio A, Genovese F, Calcinoni O, Macchi A, Dunkel A, et al. Assessing the extent and timing of chemosensory impairments during COVID-19 pandemic. Sci Rep 2021;11:17504. https://doi.org/10.1038/s41598-021-96987-0.

[3] Giacomelli A, Pezzati L, Conti F, Bernacchia D, Siano M, Oreni L, et al. Self-reported Olfactory and Taste Disorders in Patients With Severe Acute Respiratory Coronavirus 2 Infection: A Cross-sectional Study. Clin Infect Dis 2020;71:889–90. https://doi.org/10.1093/cid/ciaa330.

[4] Iannuzzi L, Salzo AE, Angarano G, Palmieri VO, Portincasa P, Saracino A, et al. Gaining Back What Is Lost: Recovering the Sense of Smell in Mild to Moderate Patients After COVID-19. Chemical Senses 2020;45:875–81. https://doi.org/10.1093/chemse/bjaa066.

[5] Parma V, Ohla K, Veldhuizen MG, Niv MY, Kelly CE, Bakke AJ, et al. More Than Smell—COVID-19 Is Associated With Severe Impairment of Smell, Taste, and Chemesthesis. Chem Senses 2020;45:609–22. https://doi.org/10.1093/chemse/bjaa041.

[6] Spinato G, Fabbris C, Polesel J, Cazzador D, Borsetto D, Hopkins C, et al. Alterations in Smell or Taste in Mildly Symptomatic Outpatients With SARS-CoV-2 Infection. JAMA 2020;323:2089–90. https://doi.org/10.1001/jama.2020.6771.

[7] Cavazzana A, Larsson M, Münch M, Hähner A, Hummel T. Postinfectious olfactory loss: A retrospective study on 791 patients. The Laryngoscope 2018;128:10–5. https://doi.org/10.1002/lary.26606.

[8] Temmel AFP, Quint C, Schickinger-Fischer B, Klimek L, Stoller E, Hummel T. Characteristics of Olfactory Disorders in Relation to Major Causes of Olfactory Loss. Archives of Otolaryngology–Head & Neck Surgery 2002;128:635–41. https://doi.org/10.1001/archotol.128.6.635.

[9] Boscolo-Rizzo P, Borsetto D, Fabbris C, Spinato G, Frezza D, Menegaldo A, et al. Evolution of Altered Sense of Smell or Taste in Patients With Mildly Symptomatic COVID-19. JAMA Otolaryngology–Head & Neck Surgery 2020;146:729–32. https://doi.org/10.1001/jamaoto.2020.1379.

[10] Gerkin RC, Ohla K, Veldhuizen MG, Joseph PV, Kelly CE, Bakke AJ, et al. Recent Smell Loss Is the Best Predictor of COVID-19 Among Individuals With Recent Respiratory Symptoms. Chemical Senses 2021;46:bjaa081. https://doi.org/10.1093/chemse/bjaa081.

[11] Menni C, Valdes AM, Freidin MB, Sudre CH, Nguyen LH, Drew DA, et al. Real-time tracking of self-reported symptoms to predict potential COVID-19. Nat Med 2020;26:1037–40. https://doi.org/10.1038/s41591-020-0916-2.

[12] Wu F, Zhao S, Yu B, Chen Y-M, Wang W, Song Z-G, et al. A new coronavirus associated with human respiratory disease in China. Nature 2020;579:265–9. https://doi.org/10.1038/s41586-020-2008-3.

[13] Tyrrell DAJ, Almeida JD, Cunningham CH, Dowdle WR, Hofstad MS, McIntosh K, et al. Coronaviridae 1. Intervirology 1975;5:76–82. https://doi.org/10.1159/000149883.

[14] Hoffmann M, Kleine-Weber H, Schroeder S, Krüger N, Herrler T, Erichsen S, et al. SARS-CoV-2 Cell Entry Depends on ACE2 and TMPRSS2 and Is Blocked by a Clinically Proven Protease Inhibitor. Cell 2020;181:271-280.e8. https://doi.org/10.1016/j.cell.2020.02.052.
[15] Mittal A, Manjunath K, Ranjan RK, Kaushik S, Kumar S, Verma V. COVID-19 pandemic: Insights into structure, function, and hACE2 receptor recognition by SARS-CoV-2. PLOS Pathogens 2020;16:e1008762. https://doi.org/10.1371/journal.ppat.1008762.
[16] Lan J, Ge J, Yu J, Shan S, Zhou H, Fan S, et al. Structure of the SARS-CoV-2 spike receptor-binding domain bound to the ACE2 receptor. Nature 2020;581:215–20. https://doi.org/10.1038/s41586-020-2180-5.
[17] Sanders DW, Jumper CC, Ackerman PJ, Bracha D, Donlic A, Kim H, et al. SARS-CoV-2 requires cholesterol for viral entry and pathological syncytia formation. ELife 2021;10:e65962. https://doi.org/10.7554/eLife.65962.
[18] Hoffmann M, Kleine-Weber H, Pöhlmann S. A Multibasic Cleavage Site in the Spike Protein of SARS-CoV-2 Is Essential for Infection of Human Lung Cells. Molecular Cell 2020;78:779-784.e5. https://doi.org/10.1016/j.molcel.2020.04.022.
[19] Peacock TP, Goldhill DH, Zhou J, Baillon L, Frise R, Swann OC, et al. The furin cleavage site in the SARS-CoV-2 spike protein is required for transmission in ferrets. Nat Microbiol 2021;6:899–909. https://doi.org/10.1038/s41564-021-00908-w.
[20] Braga L, Ali H, Secco I, Chiavacci E, Neves G, Goldhill D, et al. Drugs that inhibit TMEM16 proteins block SARS-CoV-2 spike-induced syncytia. Nature 2021;594:88–93. https://doi.org/10.1038/s41586-021-03491-6.
[21] Buchrieser J, Dufloo J, Hubert M, Monel B, Planas D, Rajah MM, et al. Syncytia formation by SARS-CoV-2-infected cells. The EMBO Journal 2020;39. https://doi.org/10.15252/embj.2020106267.
[22] Cappelletto A, Allan HE, Crescente M, Schneider E, Bussani R, Ali H, et al. SARS-CoV-2 Spike protein activates TMEM16F-mediated platelet pro-coagulant activity 2021:2021.12.14.472668. https://doi.org/10.1101/2021.12.14.472668.
[23] Lazebnik Y. Cell fusion as a link between the SARS-CoV-2 spike protein, COVID-19 complications, and vaccine side effects. Oncotarget 2021;12:2476–88. https://doi.org/10.18632/oncotarget.28088.
[24] Navaratnarajah CK, Pease DR, Halfmann PJ, Taye B, Barkhymer A, Howell KG, et al. Highly Efficient SARS-CoV-2 Infection of Human Cardiomyocytes: Spike Protein-Mediated Cell Fusion and Its Inhibition. Journal of Virology 2021. https://doi.org/10.1128/JVI.01368-21.
[25] Rajah MM, Bernier A, Buchrieser J, Schwartz O. The Mechanism and Consequences of SARS-CoV-2 Spike-Mediated Fusion and Syncytia Formation. Journal of Molecular Biology 2021:167280. https://doi.org/10.1016/j.jmb.2021.167280.
[26] Theuerkauf SA, Michels A, Riechert V, Maier TJ, Flory E, Cichutek K, et al. Quantitative assays reveal cell fusion at minimal levels of SARS-CoV-2 spike protein and fusion from without. IScience 2021;24:102170. https://doi.org/10.1016/j.isci.2021.102170.
[27] Zhu N, Wang W, Liu Z, Liang C, Wang W, Ye F, et al. Morphogenesis and cytopathic effect of SARS-CoV-2 infection in human airway epithelial cells. Nat Commun 2020;11:3910. https://doi.org/10.1038/s41467-020-17796-z.
[28] Murae M, Shimizu Y, Yamamoto Y, Kobayashi A, Houri M, Inoue T, et al. The function of SARS-CoV-2 spike protein is impaired by disulfide-bond disruption with mutation at cysteine-488 and by thiol-reactive N-acetyl-cysteine and glutathione. Biochemical and

Biophysical Research Communications 2022;597:30–6. https://doi.org/10.1016/j.bbrc.2022.01.106.
[29] Bryce C, Grimes Z, Pujadas E, Ahuja S, Beasley MB, Albrecht R, et al. Pathophysiology of SARS-CoV-2: the Mount Sinai COVID-19 autopsy experience. Mod Pathol 2021;34:1456–67. https://doi.org/10.1038/s41379-021-00793-y.
[30] Zhang Z, Zheng Y, Niu Z, Zhang B, Wang C, Yao X, et al. SARS-CoV-2 spike protein dictates syncytium-mediated lymphocyte elimination. Cell Death Differ 2021;28:2765–77. https://doi.org/10.1038/s41418-021-00782-3.
[31] Feng S, Dang S, Han TW, Ye W, Jin P, Cheng T, et al. Cryo-EM Studies of TMEM16F Calcium-Activated Ion Channel Suggest Features Important for Lipid Scrambling. Cell Reports 2019;28:567-579.e4. https://doi.org/10.1016/j.celrep.2019.06.023.
[32] Kalienkova V, Clerico Mosina V, Paulino C. The Groovy TMEM16 Family: Molecular Mechanisms of Lipid Scrambling and Ion Conduction. Journal of Molecular Biology 2021;433:166941. https://doi.org/10.1016/j.jmb.2021.166941.
[33] Picollo A, Malvezzi M, Accardi A. TMEM16 proteins: unknown structure and confusing functions. J Mol Biol 2015;427:94–105. https://doi.org/10.1016/j.jmb.2014.09.028.
[34] Stabilini S, Menini A, Pifferi S. Anion and Cation Permeability of the Mouse TMEM16F Calcium-Activated Channel. International Journal of Molecular Sciences 2021;22:8578. https://doi.org/10.3390/ijms22168578.
[35] Rajah MM, Hubert M, Bishop E, Saunders N, Robinot R, Grzelak L, et al. SARS-CoV-2 Alpha, Beta, and Delta variants display enhanced Spike-mediated syncytia formation. The EMBO Journal 2021;40. https://doi.org/10.15252/embj.2021108944.
[36] Zaitseva E, Zaitsev E, Melikov K, Arakelyan A, Marin M, Villasmil R, et al. Fusion Stage of HIV-1 Entry Depends on Virus-Induced Cell Surface Exposure of Phosphatidylserine. Cell Host & Microbe 2017;22:99-110.e7. https://doi.org/10.1016/j.chom.2017.06.012.
[37] Andres KH. [The fine structure of the olfactory region of macrosmatic animals]. Z Zellforsch Mikrosk Anat 1966;69:140–54.
[38] Dibattista M, Pifferi S, Menini A, Reisert J. Alzheimer's Disease: What Can We Learn From the Peripheral Olfactory System? Frontiers in Neuroscience 2020;14.
[39] Graziadei PP, Graziadei GA. Neurogenesis and neuron regeneration in the olfactory system of mammals. I. Morphological aspects of differentiation and structural organization of the olfactory sensory neurons. J Neurocytol 1979;8:1–18. https://doi.org/10.1007/bf01206454.
[40] Huard JM, Schwob JE. Cell cycle of globose basal cells in rat olfactory epithelium. Dev Dyn 1995;203:17–26. https://doi.org/10.1002/aja.1002030103.
[41] Schwob JE, Jang W, Holbrook EH, Lin B, Herrick DB, Peterson JN, et al. Stem and progenitor cells of the mammalian olfactory epithelium: Taking poietic license: Stem and progenitor cells of the Mammalian OE. Journal of Comparative Neurology 2017;525:1034–54. https://doi.org/10.1002/cne.24105.
[42] Durante MA, Kurtenbach S, Sargi ZB, Harbour JW, Choi R, Kurtenbach S, et al. Single-cell analysis of olfactory neurogenesis and differentiation in adult humans. Nat Neurosci 2020;23:323–6. https://doi.org/10.1038/s41593-020-0587-9.
[43] Brann DH, Tsukahara T, Weinreb C, Lipovsek M, Berge KV den, Gong B, et al. Non-neuronal expression of SARS-CoV-2 entry genes in the olfactory system suggests mechanisms underlying COVID-19-associated anosmia. Science Advances 2020. https://doi.org/10.1126/sciadv.abc5801.

[44] Fodoulian L, Tuberosa J, Rossier D, Boillat M, Kan C, Pauli V, et al. SARS-CoV-2 Receptors and Entry Genes Are Expressed in the Human Olfactory Neuroepithelium and Brain. IScience 2020;23:101839. https://doi.org/10.1016/j.isci.2020.101839.
[45] Khan M, Yoo S-J, Clijsters M, Backaert W, Vanstapel A, Speleman K, et al. Visualizing in deceased COVID-19 patients how SARS-CoV-2 attacks the respiratory and olfactory mucosae but spares the olfactory bulb. Cell 2021;184:5932-5949.e15. https://doi.org/10.1016/j.cell.2021.10.027.
[46] Butler A, Hoffman P, Smibert P, Papalexi E, Satija R. Integrating single-cell transcriptomic data across different conditions, technologies, and species. Nat Biotechnol 2018;36:411–20. https://doi.org/10.1038/nbt.4096.
[47] Satija R, Farrell JA, Gennert D, Schier AF, Regev A. Spatial reconstruction of single-cell gene expression data. Nat Biotechnol 2015;33:495–502. https://doi.org/10.1038/nbt.3192.
[48] Stuart T, Butler A, Hoffman P, Hafemeister C, Papalexi E, Mauck WM, et al. Comprehensive Integration of Single-Cell Data. Cell 2019;177:1888-1902.e21. https://doi.org/10.1016/j.cell.2019.05.031.
[49] Yang H, Kim A, David T, Palmer D, Jin T, Tien J, et al. TMEM16F Forms a Ca2+-Activated Cation Channel Required for Lipid Scrambling in Platelets during Blood Coagulation. Cell 2012;151:111–22. https://doi.org/10.1016/j.cell.2012.07.036.
[50] Aigouy B, Mirouse V. ScientiFig: a tool to build publication-ready scientific figures. Nat Methods 2013;10:1048–1048. https://doi.org/10.1038/nmeth.2692.
[51] Holbrook EH, Wu E, Curry WT, Lin DT, Schwob JE. Immunohistochemical characterization of human olfactory tissue. Laryngoscope 2011;121:1687–701. https://doi.org/10.1002/lary.21856.
[52] Hahn C-G, Han L-Y, Rawson NE, Mirza N, Borgmann-Winter K, Lenox RH, et al. In vivo and in vitro neurogenesis in human olfactory epithelium. Journal of Comparative Neurology 2005;483:154–63. https://doi.org/10.1002/cne.20424.
[53] Liang F. Olfactory receptor neuronal dendrites become mostly intra-sustentacularly enwrapped upon maturity. Journal of Anatomy 2018;232:674–85. https://doi.org/10.1111/joa.12777.
[54] Bussani R, Schneider E, Zentilin L, Collesi C, Ali H, Braga L, et al. Persistence of viral RNA, pneumocyte syncytia and thrombosis are hallmarks of advanced COVID-19 pathology. EBioMedicine 2020;61. https://doi.org/10.1016/j.ebiom.2020.103104.
[55] Lin L, Li Q, Wang Y, Shi Y. Syncytia formation during SARS-CoV-2 lung infection: a disastrous unity to eliminate lymphocytes. Cell Death Differ 2021;28:2019–21. https://doi.org/10.1038/s41418-021-00795-y.
[56] Suzuki J, Umeda M, Sims PJ, Nagata S. Calcium-dependent phospholipid scrambling by TMEM16F. Nature 2010;468:834–8. https://doi.org/10.1038/nature09583.
[57] Baig AA, Haining EJ, Geuss E, Beck S, Swieringa F, Wanitchakool P, et al. TMEM16F-Mediated Platelet Membrane Phospholipid Scrambling Is Critical for Hemostasis and Thrombosis but not Thromboinflammation in Mice—Brief Report. Arteriosclerosis, Thrombosis, and Vascular Biology 2016;36:2152–7. https://doi.org/10.1161/ATVBAHA.116.307727.
[58] Hummel T, Rothbauer C, Barz S, Grosser K, Pauli E, Kobald G. Olfactory Function in Acute Rhinitisa. Annals of the New York Academy of Sciences 1998;855:616–24. https://doi.org/10.1111/j.1749-6632.1998.tb10632.x.

[59] Lechien JR, Chiesa-Estomba CM, De Siati DR, Horoi M, Le Bon SD, Rodriguez A, et al. Olfactory and gustatory dysfunctions as a clinical presentation of mild-to-moderate forms of the coronavirus disease (COVID-19): a multicenter European study. Eur Arch Otorhinolaryngol 2020;277:2251–61. https://doi.org/10.1007/s00405-020-05965-1.
[60] Baig AM, Khaleeq A, Ali U, Syeda H. Evidence of the COVID-19 virus targeting the CNS: tissue distribution, host–virus interaction, and proposed neurotropic mechanisms. ACS Chemical Neuroscience 2020.
[61] Cooper KW, Brann DH, Farruggia MC, Bhutani S, Pellegrino R, Tsukahara T, et al. COVID-19 and the Chemical Senses: Supporting Players Take Center Stage. Neuron 2020;107:219–33. https://doi.org/10.1016/j.neuron.2020.06.032.
[62] Frere JJ, Serafini RA, Pryce KD, Zazhytska M, Oishi K, Golynker I, et al. SARS-CoV-2 infection results in lasting and systemic perturbations post recovery. 2022. https://doi.org/10.1101/2022.01.18.476786.
[63] Morrison EE, Costanzo RM. Morphology of olfactory epithelium in humans and other vertebrates. Microscopy Research and Technique 1992;23:49–61. https://doi.org/10.1002/jemt.1070230105.
[64] Liang F. Sustentacular Cell Enwrapment of Olfactory Receptor Neuronal Dendrites: An Update. Genes (Basel) 2020;11. https://doi.org/10.3390/genes11050493.
[65] Grubb S, Poulsen KA, Juul CA, Kyed T, Klausen TK, Larsen EH, et al. TMEM16F (Anoctamin 6), an anion channel of delayed Ca2+ activation. Journal of General Physiology 2013;141:585–600. https://doi.org/10.1085/jgp.201210861.
[66] Henkel B, Drose DR, Ackels T, Oberland S, Spehr M, Neuhaus EM. Co-expression of Anoctamins in Cilia of Olfactory Sensory Neurons. Chem Senses 2015;40:73–87. https://doi.org/10.1093/chemse/bju061.
[67] Ousingsawat J, Wanitchakool P, Kmit A, Romao AM, Jantarajit W, Schreiber R, et al. Anoctamin 6 mediates effects essential for innate immunity downstream of P2X7 receptors in macrophages. Nat Commun 2015;6:6245. https://doi.org/10.1038/ncomms7245.
[68] Shimizu T, Iehara T, Sato K, Fujii T, Sakai H, Okada Y. TMEM16F is a component of a Ca2+-activated Cl− channel but not a volume-sensitive outwardly rectifying Cl− channel. American Journal of Physiology-Cell Physiology 2013;304:C748–59. https://doi.org/10.1152/ajpcell.00228.2012.
[69] Ye W, Han TW, He M, Jan YN, Jan LY. Dynamic change of electrostatic field in TMEM16F permeation pathway shifts its ion selectivity. ELife 2019;8:e45187. https://doi.org/10.7554/eLife.45187.
[70] Yu K, Whitlock JM, Lee K, Ortlund EA, Yuan Cui Y, Hartzell HC. Identification of a lipid scrambling domain in ANO6/TMEM16F. ELife n.d.;4:e06901. https://doi.org/10.7554/eLife.06901.
[71] Karstensen H g., Mang Y, Fark T, Hummel T, Tommerup N. The first mutation in CNGA2 in two brothers with anosmia. Clinical Genetics 2015;88:293–6. https://doi.org/10.1111/cge.12491.
[72] Sailani MR, Jingga I, MirMazlomi SH, Bitarafan F, Bernstein JA, Snyder MP, et al. Isolated Congenital Anosmia and CNGA2 Mutation. Sci Rep 2017;7:2667. https://doi.org/10.1038/s41598-017-02947-y.
[73] Kleene SJ. The Electrochemical Basis of Odor Transduction in Vertebrate Olfactory Cilia. Chem Senses 2008;33:839–59. https://doi.org/10.1093/chemse/bjn048.

[74] Boccaccio A, Menini A, Pifferi S. The cyclic AMP signaling pathway in the rodent main olfactory system. Cell Tissue Res 2021;383:429–43. https://doi.org/10.1007/s00441-020-03391-7.
[75] Pifferi S, Boccaccio A, Menini A. Cyclic nucleotide-gated ion channels in sensory transduction. FEBS Letters 2006;580:2853–9. https://doi.org/10.1016/j.febslet.2006.03.086.
[76] Dibattista M, Amjad A, Maurya DK, Sagheddu C, Montani G, Tirindelli R, et al. Calcium-activated chloride channels in the apical region of mouse vomeronasal sensory neurons. The Journal of General Physiology 2012;140:3–15. https://doi.org/10.1085/jgp.201210780.
[77] Olender T, Keydar I, Pinto JM, Tatarskyy P, Alkelai A, Chien MS, et al. The human olfactory transcriptome. BMC Genomics 2016;17:619. https://doi.org/10.1186/s12864-016-2960-3.
[78] Stephan AB, Shum EY, Hirsh S, Cygnar KD, Reisert J, Zhao H. ANO2 is the cilial calcium-activated chloride channel that may mediate olfactory amplification. PNAS 2009;106:11776–81. https://doi.org/10.1073/pnas.0903304106.
[79] Dibattista M, Pifferi S, Boccaccio A, Menini A, Reisert J. The long tale of the calcium activated Cl(-) channels in olfactory transduction. Channels (Austin) 2017:1–16. https://doi.org/10.1080/19336950.2017.1307489.
[80] Neureither F, Stowasser N, Frings S, Möhrlen F. Tracking of unfamiliar odors is facilitated by signal amplification through anoctamin 2 chloride channels in mouse olfactory receptor neurons. Physiological Reports 2017;5:e13373. https://doi.org/10.14814/phy2.13373.
[81] Pietra G, Dibattista M, Menini A, Reisert J, Boccaccio A. The Ca2+-activated Cl− channel TMEM16B regulates action potential firing and axonal targeting in olfactory sensory neurons. The Journal of General Physiology 2016;148:293–311. https://doi.org/10.1085/jgp.201611622.
[82] Zak JD, Grimaud J, Li R-C, Lin C-C, Murthy VN. Calcium-activated chloride channels clamp odor-evoked spike activity in olfactory receptor neurons. Sci Rep 2018;8:10600. https://doi.org/10.1038/s41598-018-28855-3.
[83] Galougahi MK, Ghorbani J, Bakhshayeshkaram M, Naeini AS, Haseli S. Olfactory Bulb Magnetic Resonance Imaging in SARS-CoV-2-Induced Anosmia: The First Report. Academic Radiology 2020;27:892–3. https://doi.org/10.1016/j.acra.2020.04.002.
[84] Vaira LA, Hopkins C, Sandison A, Manca A, Machouchas N, Turilli D, et al. Olfactory epithelium histopathological findings in long-term coronavirus disease 2019 related anosmia. The Journal of Laryngology & Otology 2020;134:1123–7. https://doi.org/10.1017/S0022215120002455.
[85] Capraro A, Wong SL, Adhikari A, Allan KM, Patel HR, Zhong L, et al. Ageing impairs the airway epithelium defence response to SARS-CoV-2. 2021. https://doi.org/10.1101/2021.04.05.437453.
[86] Chen G, Wu D, Guo W, Cao Y, Huang D, Wang H, et al. Clinical and immunological features of severe and moderate coronavirus disease 2019. J Clin Invest 2020;130. https://doi.org/10.1172/JCI137244.
[87] Sungnak W, Huang N, Bécavin C, Berg M, Queen R, Litvinukova M, et al. SARS-CoV-2 entry factors are highly expressed in nasal epithelial cells together with innate immune genes. Nature Medicine 2020:1–7.
[88] Koch J, Uckeley ZM, Lozach P. SARS-CoV-2 variants as super cell fusers: cause or consequence of COVID-19 severity? The EMBO Journal 2021;40. https://doi.org/10.15252/embj.2021110041.

[89] Cheng Y, Feng S, Puchades C, Ko J, Figueroa E, Chen Y, et al. Identification of a conserved drug binding pocket in TMEM16 proteins. Res Sq 2022:rs.3.rs-1296933. https://doi.org/10.21203/rs.3.rs-1296933/v1.

Supplementary Table 1. Clusters, cell numbers and cell type.

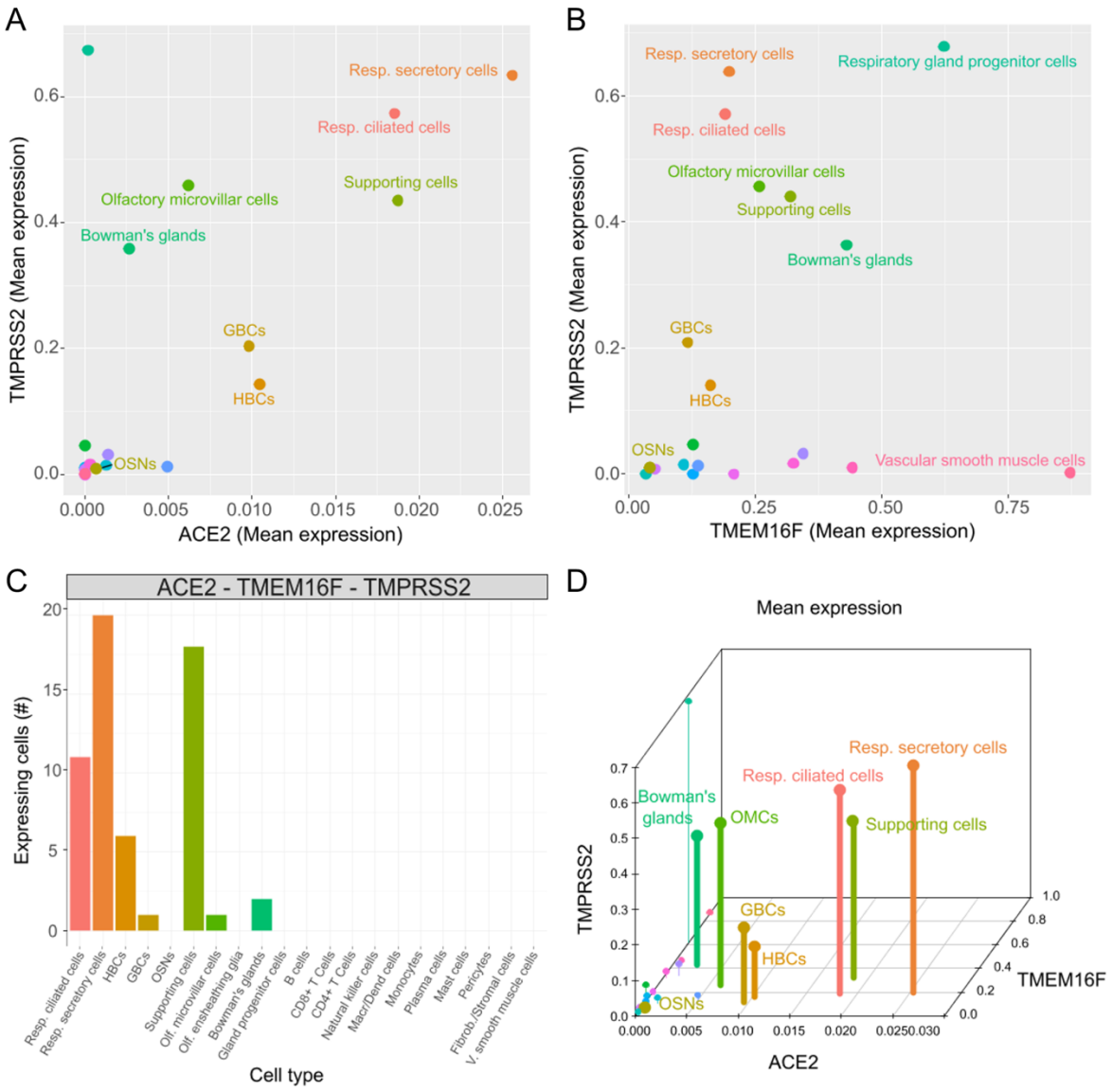
Cluster_number	Cell_count	Cell_type
0	3761	Olfactory HBCs/Respiratory HBCs
1	3668	Fibroblasts/Stromal cells
2	2178	CD8+ T Cells
3	2026	Supporting cells
4	1990	Pericytes
5	1697	Vascular smooth muscle cells
6	1269	Pericytes
7	1242	CD4+ T Cells
8	1210	Respiratory gland progenitor cells
9	1199	Respiratory secretory cells
10	1189	Supporting cells
11	1181	Macrophages/Dendritic cells
12	1176	Bowman's glands
13	1101	Plasma cells
14	856	Respiratory ciliated cells
15	805	Immature neurons/Mature neurons
16	581	Bowman's glands
17	471	Bowman's glands
18	365	Monocytes
19	315	Plasma cells
20	269	Natural killer cells

21	263	B cells
22	251	GBCs
23	246	Olfactory ensheathing glia
24	159	Mast cells
25	93	Olfactory microvillar cells
26	67	Olfactory HBCs/Respiratory HBCs

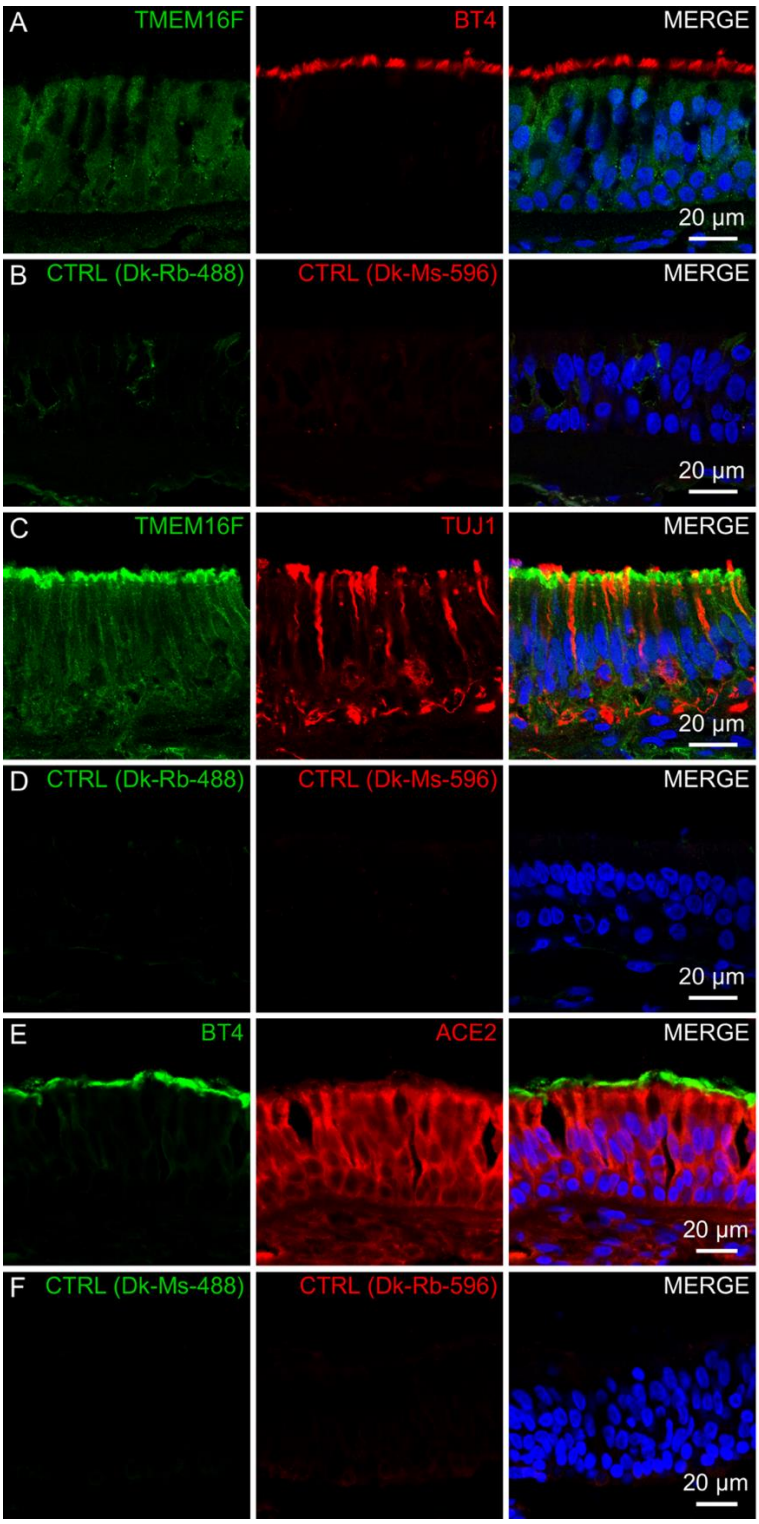
Supplementary Table 2. Overall cell count for each group of cell type.

Cell_type	Cell_count
Olfactory HBCs/Respiratory HBCs	3828
Fibroblasts/Stromal cells	3668
CD8+ T Cells	2178
Supporting cells	3215
Pericytes	3259
Vascular smooth muscle cells	1697
CD4+ T Cells	1242
Respiratory gland progenitor cells	1210
Respiratory secretory cells	1199
Macrophages/Dendritic cells	1181
Bowman's glands	2228
Plasma cells	1416
Respiratory ciliated cells	856
Immature neurons/Mature neurons	805
Monocytes	365
Natural killer cells	269
B cells	263
GBCs	251
Olfactory ensheathing glia	246
Mast cells	159

Olfactory microvillar cells	93



Supplementary Fig. S1. *TMEM16F*, *ACE2* and *TMPRSS2* co-expression in cells from human nasal epithelium. (A-B) Co-expression of *ACE2* and *TMPRSS2* (A) or *TMEM16F* and *TMPRSS2.* (B) in the different cell clusters. Mean normalized expression levels are plotted. (C) Bar plot displaying the number of cells co-expressing *ACE*2, *TMEM16F* and *TMPRSS2* by cluster. (D) 3D-bar plot displaying the co-expression of *ACE2*, *TMPRSS2* and *TMEM16F* by cell cluster. Mean normalized expression levels are plotted. The three genes are co-expressed in respiratory secretory cells, respiratory ciliated cells, olfactory supporting cells, olfactory microvillar cells, Bowman's gland cells, horizontal basal cells and globose basal cells clusters.



Supplementary Fig. S2. Control experiments for immunohistochemistry in the absence of primary antibodies. (A-B) Section of human respiratory epithelium immunostained for (A) TMEM16F (green) and BT4 (red) (same slice as in Figure 3C); and (B) negative control avoiding primary antibodies. (C-D) Section of human olfactory epithelium immunostained for (C) TMEM16F (green) and TUJ1 (red) (same slice as in

Fig.3D-F); and (D) negative control avoiding primary antibodies. (E-F) Section of human respiratory epithelium immunostained for (E) BT4 (green) and ACE2 (red) (same slice as in Figure 2C); and (B) negative control avoiding primary antibodies. Pseudocolor was modified in Figure 2C for easier visualization. Same brightness and contrast modification was applied to images from positive immunohistochemistry and its respective negative control. Nuclei were stained with DAPI (blue).

7. References

Adipietro, K. A., Mainland, J. D. and Matsunami, H. (2012) 'Functional evolution of mammalian odorant receptors', *PLoS Genetics*, 8(7). doi: 10.1371/journal.pgen.1002821.

Adomaviciene, A. *et al.* (2013) 'Putative pore-loops of TMEM16/anoctamin channels affect channel density in cell membranes', *Journal of Physiology*, 591(14), pp. 3487–3505. doi: 10.1113/jphysiol.2013.251660.

Agostinelli, E. *et al.* (2021) 'A role for stoml3 in olfactory sensory transduction', *eNeuro*, 8(2), pp. 1–12. doi: 10.1523/ENEURO.0565-20.2021.

Alvites, R. D. *et al.* (2018) 'The Nasal Cavity of the Rat and Mouse—Source of Mesenchymal Stem Cells for Treatment of Peripheral Nerve Injury', *Anatomical Record*, 301(10), pp. 1678–1689. doi: 10.1002/ar.23844.

Antunes, G., Sebastião, A. M. and Simoes De Souza, F. M. (2014) 'Mechanisms of regulation of olfactory transduction and adaptation in the olfactory cilium', *PLoS ONE*, 9(8). doi: 10.1371/journal.pone.0105531.

Baig, A. A. *et al.* (2016) 'TMEM16F-Mediated Platelet Membrane Phospholipid Scrambling Is Critical for Hemostasis and Thrombosis but not Thromboinflammation in Mice - Brief Report', *Arteriosclerosis, Thrombosis, and Vascular Biology*, 36(11), pp. 2152–2157. doi: 10.1161/ATVBAHA.116.307727.

Bannister, L. H. and Dodson, H. C. (1992) 'Endocytic pathways in the olfactory and vomeronasal epithelia of the mouse: Ultrastructure and uptake of tracers', *Microscopy Research and Technique*, 23(2), pp. 128–141. doi: 10.1002/jemt.1070230204.

Barrios AW, *et al.* (2014) . Anatomy, histochemistry, and immunohistochemistry of the olfactory subsystems in mice. Front Neuroanat.;8:63. doi: 10.3389/fnana.2014.00063.

Belluscio, L. *et al.* (1998) 'Mice deficient in G(olf) are anosmic', *Neuron*, 20(1), pp. 69–81. doi: 10.1016/S0896-6273(00)80435-3.

Berghard, A., Buck, B. and Cy, G. (1996) 'Sensory Transduction in Vomeronasal Neurons : Evidence for Gao , Gai2 , and Adenylyl Cyclase II as Major Components of a Pheromone Signaling Cascade', 76(3), pp. 909–916.

Bestle, D. *et al.* (2020) 'TMPRSS2 and furin are both essential for proteolytic activation of SARS-CoV-2 in human airway cells', *Life Science Alliance*, 3(9), pp. 1–14. doi: 10.26508/LSA.202000786.

Betto, G. *et al.* (2014) 'Interactions between permeation and gating in the TMEM16B/anoctamin2 calcium-activated chloride channel', *Journal of General Physiology*, 143(6), pp. 703–718. doi: 10.1085/jgp.201411182.

Bilinska, K. *et al.* (2020) 'Expression of the SARS-CoV-2 Entry Proteins, ACE2 and TMPRSS2, in Cells of the Olfactory Epithelium: Identification of Cell Types and Trends with Age', *ACS Chem. Neurosci*, 11, p. 1555−1562. doi: 10.1021/acschemneuro.0c00210.

Bilinska, K. and Butowt, R. (2020) 'Anosmia in COVID-19: A Bumpy Road to Establishing a Cellular Mechanism', *ACS Chemical Neuroscience*, 11(15), pp. 2152–2155. doi: 10.1021/acschemneuro.0c00406.

Billig, G. M. *et al.* (2011) 'Ca2+-activated Cl- currents are dispensable for olfaction', *Nature Neuroscience*, 14(6), pp. 763–769. doi: 10.1038/nn.2821.

Boccaccio, A. *et al.* (2006) 'Fast adaptation in mouse olfactory sensory neurons does not require the activity of phosphodiesterase', *Journal of General Physiology*, 128(2), pp. 171–184. doi: 10.1085/jgp.200609555.

Boccaccio, A. *et al.* (2019) 'Lifting the veils on TMEM16E function', *Channels*, 13(1), pp. 33–35. doi: 10.1080/19336950.2018.1557470.

Boccaccio, A. and Menini, A. (2007) 'Temporal development of cyclic nucleotide-gated and Ca2+-activated Cl- currents in isolated mouse olfactory sensory neurons', *Journal of Neurophysiology*, 98(1), pp. 153–160. doi: 10.1152/jn.00270.2007.

Boccaccio, A., Menini, A. and Pifferi, S. (2021) 'The cyclic AMP signaling pathway in the rodent main olfactory system', *Cell and Tissue Research*, 383(1), pp. 429–443. doi: 10.1007/s00441-020-03391-7.

Boehm, U., Zou, Z. and Buck, L. B. (2005) 'Feedback loops link odor and pheromone signaling with reproduction', *Cell*, 123(4), pp. 683–695. doi: 10.1016/j.cell.2005.09.027.

Bozza, T. *et al.* (2002) 'Odorant receptor expression defines functional units in the mouse olfactory system', *Journal of Neuroscience*, 22(8), pp. 3033–3043. doi: 10.1523/jneurosci.22-08-03033.2002.

Bradley, J. *et al.* (2004) 'Calmodulin permanently associates with rat olfactory CNG channels under native conditions', *Nature Neuroscience*, 7(7), pp. 705–710. doi: 10.1038/nn1266.Calmodulin.

Bradley, J., Reuter, D. and Frings, S. (2001) 'Facilitation of calmodulin-mediated odor adaptation by cAMP-gated channel subunits', *Science*, 294(5549), pp. 2176–2178. doi: 10.1126/science.1063415.

Braga, L. *et al.* (2021) 'Drugs that inhibit TMEM16 proteins block SARS-CoV-2 spike-induced syncytia', *Nature*, 594(July 2020). doi: 10.1038/s41586-021-03491-6.

Brann, D. H. *et al.* (2020) 'Non-neuronal expression of SARS-CoV-2 entry genes in the olfactory system suggests mechanisms underlying COVID-19 – associated anosmia', (July), pp. 1–20.

Brechbühl, J., Moine, F. and Broillet, M.-C. (2013) 'Mouse Grueneberg ganglion neurons share molecular and functional features with C. elegans amphid neurons', *Frontiers in Behavioral Neuroscience*, 7(December), pp. 1–12. doi: 10.3389/fnbeh.2013.00193.

Breipohl, W., Laugwitz, H. J. and Bornfeld, N. (1974) 'Topological relations between the dendrites of olfactory sensory cells and sustentacular cells in different vertebrates. An ultrastructural study.', *Journal of anatomy*, 117(Pt 1), pp. 89–94. Available at: http://www.ncbi.nlm.nih.gov/pubmed/4844653%0Ahttp://www.pubmedcentral.nih.gov/articlerender.fcgi?artid=PMC1231436.

Brunet, L. J., Gold, G. H. and Ngai, J. (1996) 'General anosmia caused by a targeted disruption of the mouse olfactory cyclic nucleotide-gated cation channel', *Neuron*, 17(4), pp. 681–693. doi: 10.1016/S0896-6273(00)80200-7.

Brunner, J. D. *et al.* (2014) 'X-ray structure of a calcium-activated TMEM16 lipid scramblase', *Nature*, 516(7530), pp. 207–212. doi: 10.1038/nature13984.

Bryche, B. *et al.* (2020) 'Massive transient damage of the olfactory epithelium associated with infection of sustentacular cells by SARS-CoV-2 in golden Syrian hamsters', *Brain Behavior and Immunity*. doi: 10.1016/j.bbi.2020.06.032.

Buck, L. and Axel, R. (1991) 'A novel multigene family may encode odorant receptors.', *Society of General Physiologists series*, 47, pp. 39–51.

Buck, L. B. (2000) 'The molecular architecture of odor and pheromone sensing in mammals', *Cell*,

100(6), pp. 611–618. doi: 10.1016/S0092-8674(00)80698-4.

Cappelletto, A. *et al.* (2021) 'SARS-CoV-2 Spike protein activates TMEM16F-mediated platelet pro-coagulant activity', 4(1), pp. 1–2. Available at: http://www.ejurnal.its.ac.id/index.php/sains_seni/article/view/10544%0Ahttps://scholar.google.com/scholar?hl=en&as_sdt=0%2C5&q=tawuran+antar+pelajar&btnG=%0Ahttps://doi.org/10.1016/j.jfca.2019.103237.

Caputo, A. *et al.* (2008) 'TMEM16A, a membrane protein associated with calcium-dependent chloride channel activity', *Science*, 322(5901), pp. 590–594. doi: 10.1126/science.1163518.

Chen, C. R. *et al.* (2014) 'Anatomy and Cellular Constituents of the Human Olfactory Mucosa: A Review', *Journal of Neurological Surgery, Part B: Skull Base*, 75(5), pp. 293–300. doi: 10.1055/s-0033-1361837.

Chess, A. *et al.* (1994) 'Allelic Inactivation Regulates Olfactory Receptor Gene Expression', *Cell*, 78, pp. 823–834.

Connelly, T., Savigner, A. and Ma, M. (2013) 'Spontaneous and sensory-evoked activity in mouse olfactory sensory neurons with defined odorant receptors', *Journal of Neurophysiology*, 110(1), pp. 55–62. doi: 10.1152/jn.00910.2012.

Coppola, D. M. *et al.* (2013) 'An electroolfactogram study of odor response patterns from the mouse olfactory epithelium with reference to receptor zones and odor sorptiveness', *Journal of Neurophysiology*, 109(8), pp. 2179–2191. doi: 10.1152/jn.00769.2012.

Cygnar, K. D., Stephan, A. B. and Zhao, H. (2010) 'Analyzing responses of mouse olfactory sensory neurons using the air-phase electroolfactogram recording', *Journal of Visualized Experiments*, (37), pp. 1–5. doi: 10.3791/1850.

Cygnar, K. D. and Zhao, H. (2009) 'Phosphodiesterase 1C is dispensable for rapid response termination of olfactory sensory neurons', *Nat Neurosci.*, 12(4), pp. 454–462. doi: 10.1038/nn.2289.Phosphodiesterase.

Dahl (1988) *Molecular Neurobiology of the Olfactory System*.

Dang, S. *et al.* (2017) 'Cryo-EM structures of the TMEM16A calciumactivated chloride channel', *Nature*, 552(7685), pp. 426–429. doi: 10.1038/nature25024.

Dauner, K. *et al.* (2012) 'Expression patterns of anoctamin 1 and anoctamin 2 chloride channels

in the mammalian nose', *Cell and Tissue Research*, 347(2), pp. 327–341. doi: 10.1007/s00441-012-1324-9.

Dibattista, M. *et al.* (2008) 'Hyperpolarization-activated cyclic nucleotide-gated channels in mouse vomeronasal sensory neurons', *Journal of Neurophysiology*, 100(2), pp. 576–586. doi: 10.1152/jn.90263.2008.

Dibattista, M. *et al.* (2012) 'Calcium-activated chloride channels in the apical region of mouse vomeronasal sensory neurons', *Journal of General Physiology*, 140(1), pp. 3–15. doi: 10.1085/jgp.201210780.

Dibattista, M. *et al.* (2017) 'The long tale of the calcium activated Cl− channels in olfactory transduction', *Channels*, 11(5), pp. 399–414. doi: 10.1080/19336950.2017.1307489.

Dibattista, M. and Reisert, J. (2016) 'The odorant receptor-dependent role of olfactory marker protein in olfactory receptor neurons', *Journal of Neuroscience*, 36(10), pp. 2995–3006. doi: 10.1523/JNEUROSCI.4209-15.2016.

Dibattista M, . *et al.* (2021) 'The functional relevance of olfactory marker protein in the vertebrate olfactory system: a never-ending story'. Cell Tissue Res.;383(1):409-427.doi: 10.1007/s00441-020-03349-9.

Escada, P. A., Lima, C. and Da Silva, J. M. (2009) 'The human olfactory mucosa', *European Archives of Oto-Rhino-Laryngology*, 266(11), pp. 1675–1680. doi: 10.1007/s00405-009-1073-x.

Falzone, M. E. *et al.* (2018) 'Known structures and unknown mechanisms of TMEM16 scramblases and channels', *Journal of General Physiology*, 150(7), pp. 933–947. doi: 10.1085/jgp.201711957.

Firestein, S. (2001) 'How the olfactory system makes sense of scents', *Nature*, 413(6852), pp. 211–218. doi: 10.1038/35093026.

Firestein, S., Zufall, F. and Shepherd, G. M. (1991) 'Single odor-sensitive channels in olfactory receptor neurons are also gated by cyclic nucleotides', *Journal of Neuroscience*, 11(11), pp. 3565–3572. doi: 10.1523/jneurosci.11-11-03565.1991.

Fluegge, D. *et al.* (2012) 'Mitochondrial Ca 2+ mobilization is a key element in olfactory signaling', *Nature Neuroscience*, 15(5), pp. 754–762. doi: 10.1038/nn.3074.

Fodoulian, L. *et al.* (2020) 'SARS-CoV-2 Receptors and Entry Genes Are Expressed in the Human Olfactory SARS-CoV-2 Receptors and Entry Genes Are Expressed in the Human Olfactory',

iScience. doi: 10.1016/j.isci.2020.101839.

Franceschini, V. *et al.* (2009) 'Human cord blood CD1331 stem cells transplanted to nod-scid mice provide conditions for regeneration of olfactory neuroepithelium after permanent damage induced by dichlobenil', *Stem Cells*, 27(4), pp. 825–835. doi: 10.1002/stem.11.

Frings, S. (2009) *Chloride-based signal amplification in olfactory sensory neurons*, *Physiology and Pathology of chloride transporters and channels in the nervous system*. Elsevier Inc. doi: 10.1016/B978-0-12-374373-2.00020-0.

Fung, T. S. and Liu, D. X. (2019) 'Human Coronavirus : Host-Pathogen Interaction', *Annual Review of Microbiology*, pp. 529–560.

Giannetti, N. *et al.* (1995) 'Immunocytochemical study of the differentiation process of the septal organ of Masera in developing rats', *Developmental Brain Research*, 84(2), pp. 287–293. doi: 10.1016/0165-3806(94)00195-6.

Graziadei (1973) 'CELL DYNAMICS IN THE OLFACTORY', *Tissue and Cell*, 5(November 1972).

Graziadei, P. P. C. and Graziadei, G. A. M. (1979) 'Neurogenesis and neuron regeneration in the olfactory system of mammals. I. Morphological aspects of differentiation and structural organization of the olfactory sensory neurons', *Journal of Neurocytology*, 8(1), pp. 1–18. doi: 10.1007/BF01206454.

Gyobu, S. *et al.* (2017) 'Characterization of the scrambling domain of the TMEM16 family', *Proceedings of the National Academy of Sciences of the United States of America*, 114(24), pp. 6274–6279. doi: 10.1073/pnas.1703391114.

Ha, G. E. *et al.* (2016) 'The Ca2+ -activated chloride channel anoctamin-2 mediates spike-frequency adaptation and regulates sensory transmission in thalamocortical neurons', *Nature Communications*, 7, pp. 1–13. doi: 10.1038/ncomms13791.

Haberly, L. B. (2001) 'Parallel-distributed processing in olfactory cortex: new insights from morphological and physiological analysis of neuronal circuitry', *Chemical Senses*, 26, pp. 551–576. Available at: papers2://publication/uuid/5291FD14-066F-4119-9796-B9C1CB1F5444.

Hahn, C. G. *et al.* (2005) 'In vivo and in vitro neurogenesis in human olfactory epithelium', *Journal of Comparative Neurology*, 483(2), pp. 154–163. doi: 10.1002/cne.20424.

Harkema, J. R., Carey, S. A. and Wagner, J. G. (2006) 'The Nose Revisited: A Brief Review of the

Comparative Structure, Function, and Toxicologic Pathology of the Nasal Epithelium', *Toxicologic Pathology*, 34(3), pp. 252–269. doi: 10.1080/01926230600713475.

Hartzell, H. C. *et al.* (2009) 'Anoctamin/TMEM16 family members are Ca2+-activated Cl-channels', *Journal of Physiology*, 587(10), pp. 2127–2139. doi: 10.1113/jphysiol.2008.163709.

Hengl, T. *et al.* (2010) 'Molecular components of signal amplification in olfactory sensory cilia', *Proceedings of the National Academy of Sciences of the United States of America*, 107(13), pp. 6052–6057. doi: 10.1073/pnas.0909032107.

Henriques, T. *et al.* (2019) 'TMEM16A calcium-activated chloride currents in supporting cells of the mouse olfactory epithelium', *Journal of General Physiology*, 151(7), pp. 954–966. doi: 10.1085/jgp.201812310.

Hikmet, F. *et al.* (2020) 'The protein expression profile of ACE 2 in human tissues', pp. 1–16.

Van Der Hoek, L. *et al.* (2004) 'Identification of a new human coronavirus', *Nature Medicine*, 10(4), pp. 368–373. doi: 10.1038/nm1024.

Hofmann, H. *et al.* (2005) 'Human coronavirus NL63 employs the severe acute respiratory syndrome coronavirus receptor for cellular entry', *Proceedings of the National Academy of Sciences of the United States of America*, 102(22), pp. 7988–7993. doi: 10.1073/pnas.0409465102.

Huang, F. *et al.* (2009) 'Studies on expression and function of the TMEM16A calcium-activated chloride channel', *Proceedings of the National Academy of Sciences of the United States of America*, 106(50), pp. 21413–21418. doi: 10.1073/pnas.0911935106.

Huang, F., Wong, X. and Jan, L. Y. (2012) 'International Union of Basic and Clinical', *Pharmacological Reviews*, 62(4), pp. 632–667. Available at: http://pharmrev.aspetjournals.org/content/62/4/632.short.

Huang, W. C. *et al.* (2012) 'Calcium-Activated Chloride Channels (CaCCs) Regulate Action Potential and Synaptic Response in Hippocampal Neurons', *Neuron*, 74(1), pp. 179–192. doi: 10.1016/j.neuron.2012.01.033.

Imai, T. (2014) 'Construction of functional neuronal circuitry in the olfactory bulb', *Seminars in Cell and Developmental Biology*, 35, pp. 180–188. doi: 10.1016/j.semcdb.2014.07.012.

Inhibitor, P. *et al.* (2020) 'SARS-CoV-2 Cell Entry Depends on ACE2 and TMPRSS2 and Is Blocked

by a Clinically Proven Article SARS-CoV-2 Cell Entry Depends on ACE2 and TMPRSS2 and Is Blocked by a Clinically Proven Protease Inhibitor', pp. 271–280. doi: 10.1016/j.cell.2020.02.052.

Ishii, T. *et al.* (2001) 'Monoallelic expresion of the odourant receptor gene and axonal projection of olfactory sensory neurones', *Genes to Cells*, pp. 71–78.

Jafek, W. (1982) 'The fine structure of the olfactory m u c o s a in m a n', 6.

Jian, L. *et al.* (2020) 'Perspective: COVID-19, implications of nasal diseases and consequences for their management', *Journal of Allergy and Clinical Immunology*, 146(1), pp. 67–69. doi: 10.1016/j.jaci.2020.04.030.

Jones, D. T. and Reed, R. R. (1989) 'Golf: An olfactory neuron specific-G protein involved in odorant signal transduction', *Science*, 244(4906), pp. 790–795. doi: 10.1126/science.2499043.

Kanageswaran, N. *et al.* (2015) 'Deep Sequencing of the Murine Olfactory Receptor Neuron Transcriptome', pp. 1–47. doi: 10.1371/journal.pone.0113170.

Kaneko, H. *et al.* (2004) 'Chloride accumulation in mammalian olfactory sensory neurons', *Journal of Neuroscience*, 24(36), pp. 7931–7938. doi: 10.1523/JNEUROSCI.2115-04.2004.

Kaneko, H., Nakamura, T. and Lindemann, B. (2001) 'Noninvasive measurement of chloride concentration in rat olfactory receptor cells with use of a fluorescent dye', *American Journal of Physiology - Cell Physiology*, 280(6 49-6), pp. 1387–1393. doi: 10.1152/ajpcell.2001.280.6.c1387.

Kato, A. and Touhara, K. (2009) 'Mammalian olfactory receptors : pharmacology , G protein coupling and desensitization', pp. 3743–3753. doi: 10.1007/s00018-009-0111-6.

Kaupp, U. B. and Seifert, R. (2002) 'Cyclic Nucleotide-Gated Ion Channels', *Physiol Rev*, pp. 769–824.

Khan, M. *et al.* (2021) 'Visualizing in deceased COVID-19 patients how SARS-CoV-2 attacks the respiratory and olfactory mucosae but spares the olfactory bulb', *Cell*. doi: 10.1016/j.cell.2021.10.027.

Kini, A. D. and Firestein, S. (2001) 'The molecular basis of olfaction', *Chimia*, 55(5), pp. 453–459.

Kleene, S. J. (1997) 'High-gain, low-noise amplification in olfactory transduction', *Biophysical Journal*, 73(2), pp. 1110–1117. doi: 10.1016/S0006-3495(97)78143-8.

Kleene, S. J. (2008) 'The electrochemical basis of odor transduction in vertebrate olfactory cilia', *Chemical Senses*, 33(9), pp. 839–859. doi: 10.1093/chemse/bjn048.

Kleene, S. J. and Gesteland, R. C. (1991) 'Calcium-activated chloride conductance in frog olfactory cilia', *Journal of Neuroscience*, 11(11), pp. 3624–3629. doi: 10.1523/jneurosci.11-11-03624.1991.

Kleene, Steven J. and Gesteland, R. C. (1991) 'Transmembrane currents in frog olfactory cilia', *The Journal of Membrane Biology*, 120(1), pp. 75–81. doi: 10.1007/BF01868593.

Klingenstein, M. *et al.* (2021) 'Evidence of SARS-CoV2 Entry Protein ACE2 in the Human Nose and Olfactory Bulb', pp. 155–164. doi: 10.1159/000513040.

Krautwurst, D. *et al.* (1998) 'Identification of Ligands for Olfactory Receptors', 95, pp. 917–926.

Kurahashi, T. and Menini, A. (1997) 'Mechanism of odorant adaptation in the olfactory receptor cell', *Nature*, pp. 725–729. doi: 10.1038/385725a0.

Kurahashi, T. and Yau, K. W. (1993) 'Co-existence of cationic and chloride components in odorantinduced current of vertebrate olfactory receptor cells', 363(May), pp. 71–74.

Lagostena, L. and Menini, A. (2003) 'Whole-cell recordings and photolysis of caged compounds in olfactory sensory neurons isolated from the mouse', *Chemical Senses*, 28(8), pp. 705–716. doi: 10.1093/chemse/bjg063.

Lau, Y. E. and Cherry, J. A. (2000) 'Distribution of PDE4A and G(oα) immunoreactivity in the accessory olfactory system of the mouse', *NeuroReport*, 11(1), pp. 27–32. doi: 10.1097/00001756-200001170-00006.

Leinders-Zufall, T. *et al.* (2004) 'MHC class I peptides as chemosensory signals in the vomeronasal organ', *Science*, 306(5698), pp. 1033–1037. doi: 10.1126/science.1102818.

Letko, M., Marzi, A. and Munster, V. (2020) 'Functional assessment of cell entry and receptor usage for SARS-CoV-2 and other lineage B betacoronaviruses', *Nature Microbiology*, 5(4), pp. 562–569. doi: 10.1038/s41564-020-0688-y.

Leung, C. T., Coulombe, P. A. and Reed, R. R. (2007) 'Contribution of olfactory neural stem cells to tissue maintenance and regeneration', *Nature Neuroscience*, 10(6), pp. 720–726. doi: 10.1038/nn1882.

Li, K. X. *et al.* (2019) 'TMEM16B regulates anxiety-related behavior and GABAergic neuronal signaling in the central lateral Amygdala', *eLife*, 8, pp. 1–20. doi: 10.7554/eLife.47106.

Li, R. C. *et al.* (2018) 'Ca2+-activated Cl current predominates in threshold response of mouse olfactory receptor neurons', *Proceedings of the National Academy of Sciences of the United*

States of America, 115(21), pp. 5570–5575. doi: 10.1073/pnas.1803443115.

Lin, L. *et al.* (2021) 'Syncytia formation during SARS-CoV-2 lung infection: a disastrous unity to eliminate lymphocytes', *Cell Death and Differentiation*, 28(6), pp. 2019–2021. doi: 10.1038/s41418-021-00795-y.

Lledo, P. M., Gheusi, G. and Vincent, J. D. (2005) 'Information processing in the mammalian olfactory system', *Physiological Reviews*, 85(1), pp. 281–317. doi: 10.1152/physrev.00008.2004.

Lodovichi, C. and Belluscio, L. (2012) 'Odorant receptors in the formation of the olfactory bulb circuitry', *Physiology*, 27(4), pp. 200–212. doi: 10.1152/physiol.00015.2012.

Lorenzon, P. *et al.* (2015) 'Circuit formation and function in the olfactory bulb of mice with reduced spontaneous afferent activity', *Journal of Neuroscience*, 35(1), pp. 146–160. doi: 10.1523/JNEUROSCI.0613-14.2015.

Lowe, G. and Gold, G. H. (1993) 'Nonlinear amplification by calcium-dependent chloride channels in olfactory receptor cells', *Nature*, 366(6452), pp. 283–286. doi: 10.1038/366283a0.

Lynch, J. W. and Barry, P. H. (1989) 'Action potentials initiated by single channels opening in a small neuron (rat olfactory receptor)', *Biophysical Journal*, 55(4), pp. 755–768. doi: 10.1016/S0006-3495(89)82874-7.

Ma, M. (2007) 'Encoding olfactory signals via multiple chemosensory systems', *Critical Reviews in Biochemistry and Molecular Biology*, 42(6), pp. 463–480. doi: 10.1080/10409230701693359.

Ma, M., Chen, W. R. and Shepherd, G. M. (1999) 'Electrophysiological characterization of rat and mouse olfactory receptor neurons from an intact epithelial preparation', *Journal of Neuroscience Methods*, 92(1–2), pp. 31–40. doi: 10.1016/S0165-0270(99)00089-8.

Mainland, J. D. *et al.* (2014) 'From molecule to mind: An integrative perspective on odor intensity', *Trends in Neurosciences*, 37(8), pp. 443–454. doi: 10.1016/j.tins.2014.05.005.

Malnic, B. *et al.* (1999) 'Combinatorial receptor codes for odors', *Cell*, 96(5), pp. 713–723. doi: 10.1016/S0092-8674(00)80581-4.

Malvezzi, M. *et al.* (2018) 'Out-of-the-groove transport of lipids by TMEM16 and GPCR scramblases', *Proceedings of the National Academy of Sciences of the United States of America*, 115(30), pp. E7033–E7042. doi: 10.1073/pnas.1806721115.

Mandiyan, V. S., Coats, J. K. and Shah, N. M. (2005) 'Deficits in sexual and aggressive behaviors in

Cnga2 mutant mice', *Nature Neuroscience*, 8(12), pp. 1660–1662. doi: 10.1038/nn1589.

Maue, R. A. and Dionne, V. E. (1987) 'Patch-clamp studies of isolated mouse olfactory receptor neurons', *Journal of General Physiology*, 90(1), pp. 95–125. doi: 10.1085/jgp.90.1.95.

Maurya, D. K. *et al.* (2015) 'Development of the olfactory epithelium and Nasal Glands in TMEM16A-/-and TMEM16A+/ +Mice', *PLoS ONE*, 10(6), pp. 1–20. doi: 10.1371/journal.pone.0129171.

Maurya, D. K. and Menini, A. (2014) 'Developmental expression of the calcium-activated chloride channels TMEM16A and TMEM16B in the mouse olfactory epithelium', *Developmental Neurobiology*, 74(7), pp. 657–675. doi: 10.1002/dneu.22159.

Meinhardt, J. *et al.* (2021) 'Olfactory transmucosal SARS-CoV-2 invasion as a port of central nervous system entry in individuals with COVID-19', *Nature Neuroscience*, 24(2), pp. 168–175. doi: 10.1038/s41593-020-00758-5.

de Melo, G. D. *et al.* (2021) 'COVID-19-related anosmia is associated with viral persistence and inflammation in human olfactory epithelium and brain infection in hamsters', *Science Translational Medicine*, 13(596), pp. 1–25. doi: 10.1126/scitranslmed.abf8396.

Menco, B. and Morrison, E. (2003) *Morphology of the Mammalian Olfactory Epithelium*, *Handbook of Olfaction and Gustation*. doi: 10.1201/9780203911457.ch2.

Menco, B. P. M. *et al.* (1992) 'Ultrastructural localization of olfactory transduction components: the G protein subunit Golfα and type III adenylyl cyclase', *Neuron*, 8(3), pp. 441–453. doi: 10.1016/0896-6273(92)90272-F.

Menco, B. P. M. *et al.* (1998) 'Ultrastructural localization of amiloride-sensitive sodium channels and Na+,K+-ATPase in the rat's olfactory epithelial surface', *Chemical Senses*, 23(2), pp. 137–149. doi: 10.1093/chemse/23.2.137.

Menco, B. P. M. and Jackson, J. E. (1997) 'Cells resembling hair cells in developing rat olfactory and nasal respiratory epithelia', *Tissue and Cell*, 29(6), pp. 707–713. doi: 10.1016/S0040-8166(97)80046-8.

Mendoza, A. S. (1993) 'Morphological studies on the rodent main and accessory olfactory systems: The regio olfactoria and vomeronasal organ', *Annals of Anatomy*, 175(5), pp. 425–446. doi: 10.1016/S0940-9602(11)80110-X.

Meng, X. *et al.* (2020) 'Since January 2020 Elsevier has created a COVID-19 resource centre with free information in English and Mandarin on the novel coronavirus COVID- 19 . The COVID-19 resource centre is hosted on Elsevier Connect , the company ' s public news and information', *American Journal of Otolaryngology*, (January), pp. 1–6.

Menini, A., Lagostena, L. and Boccaccio, A. (2004) 'Olfaction: From odorant molecules to the olfactory cortex', *News in Physiological Sciences*, 19(3), pp. 101–104. doi: 10.1152/nips.1507.2003.

Meredith, M. (2001) 'Human Vomeronasal Organ Function : A Critical Review of Best and Worst Cases', pp. 433–445.

Michalakis, S. *et al.* (2006) 'Loss of CNGB1 protein leads to olfactory dysfunction and subciliary cyclic nucleotide-gated channel trapping', *Journal of Biological Chemistry*, 281(46), pp. 35156–35166. doi: 10.1074/jbc.M606409200.

Milenkovic, V. M. *et al.* (2010) 'Evolution and functional divergence of the anoctamin family of membrane proteins', *BMC Evolutionary Biology*, 10(1). doi: 10.1186/1471-2148-10-319.

Mohrhardt, J. *et al.* (2018) 'Signal detection and coding in the accessory olfactory system', *Chemical Senses*, 43(9), pp. 667–695. doi: 10.1093/chemse/bjy061.

Mombaerts, P. *et al.* (1996) 'Visualizing an olfactory sensory map', *Cell*, 87(4), pp. 675–686. doi: 10.1016/S0092-8674(00)81387-2.

Mombaerts, P. (1999) 'Seven transmembrane proteins as odorant and chemosensory receptors', *Science*, 286(5440), pp. 707–711. doi: 10.1126/science.286.5440.707.

Mombaerts, P. (2004a) 'Genes and ligands for odorant, vomeronasal and taste receptors', *Nature Reviews Neuroscience*, 5(4), pp. 263–278. doi: 10.1038/nrn1365.

Mombaerts, P. (2004b) 'Odorant receptor gene choice in olfactory sensory neurons: The one receptor-one neuron hypothesis revisited', *Current Opinion in Neurobiology*, 14(1), pp. 31–36. doi: 10.1016/j.conb.2004.01.014.

Mombaerts, P. (2006) 'Axonal wiring in the mouse olfactory system', *Annual Review of Cell and Developmental Biology*, 22, pp. 713–737. doi: 10.1146/annurev.cellbio.21.012804.093915.

Montani, G. *et al.* (2006) 'Neuropeptide Y in the olfactory microvillar cells', *European Journal of Neuroscience*, 24(1), pp. 20–24. doi: 10.1111/j.1460-9568.2006.04878.x.

Moran, D. T., Carter Rowley, J. and Jafek, B. W. (1982) 'Electron microscopy of human olfactory epithelium reveals a new cell type: The microvillar cell', *Brain Research*, 253(1–2), pp. 39–46. doi: 10.1016/0006-8993(82)90671-0.

Morrison, E. E. and Costanzo, R. M. (1990) 'Morphology of the human olfactory epithelium', *Journal of Comparative Neurology*, 297(1), pp. 1–13. doi: 10.1002/cne.902970102.

Munger (2001) 'Central Role of the CNGA4 Channel Subunit in Ca2+ -Calmodulin– Dependent Odor Adaptation', *Bone*, 23(1), pp. 1–7. doi: 10.1126/science.1063224.Central.

Munger, S. D., Leinders-Zufall, T. and Zufall, F. (2009) 'Subsystem organization of the mammalian sense of smell', *Annual Review of Physiology*, 71, pp. 115–140. doi: 10.1146/annurev.physiol.70.113006.100608.

Nache, V. *et al.* (2005) 'Activation of olfactory-type cyclic nucleotide-gated channels is highly cooperative', *Journal of Physiology*, 569(1), pp. 91–102. doi: 10.1113/jphysiol.2005.092304.

Nagayama, S., Homma, R. and Imamura, F. (2014) 'Neuronal organization of olfactory bulb circuits', *Frontiers in Neural Circuits*, 8(SEP), pp. 1–19. doi: 10.3389/fncir.2014.00098.

Nakamura, T. and Gold, G. H. (1987) 'A cyclic nucleotide-gated conductance in olfactory receptor cilia', *Nature*, 325(6103), pp. 442–444. doi: 10.1038/325442a0.

Nakamura, T., Kaneko, H. and Nishida, N. (1997) 'Direct measurement of the chloride concentration in newt olfactory receptors with the fluorescent probe', *Neuroscience Letters*, 237(1), pp. 5–8. doi: 10.1016/S0304-3940(97)00794-5.

Nakashima, N. *et al.* (2020) 'Olfactory marker protein directly buffers cAMP to avoid depolarization-induced silencing of olfactory receptor neurons', *Nature Communications*, 11(1), pp. 4–5. doi: 10.1038/s41467-020-15917-2.

Neureither, F., Ziegler, K., *et al.* (2017) 'Impaired Motor Coordination and Learning in Mice Lacking Anoctamin 2 Calcium-Gated Chloride Channels', *Cerebellum*, 16(5–6), pp. 929–937. doi: 10.1007/s12311-017-0867-4.

Neureither, F., Stowasser, N., *et al.* (2017) 'Tracking of unfamiliar odors is facilitated by signal amplification through anoctamin 2 chloride channels in mouse olfactory receptor neurons', *Physiological Reports*, 5(15). doi: 10.14814/phy2.13373.

Ni, Y., Kuan, A. and Chen, T. (2014) 'Activation and Inhibition of TMEM16A Calcium-Activated

Chloride Channels', *Plos One*, 9(1), pp. 4–6. doi: 10.1371/journal.pone.0086734.

Nickell, W. T., Kleene, N. K. and Kleene, S. J. (2007) 'Mechanisms of neuronal chloride accumulation in intact mouse olfactory epithelium', *Journal of Physiology*, 583(3), pp. 1005–1020. doi: 10.1113/jphysiol.2007.129601.

Paulino, C. *et al.* (2017) 'Activation mechanism of the calcium-activated chloride channel TMEM16A revealed by cryo-EM', *Nature*, 552(7685), pp. 421–425. doi: 10.1038/nature24652.

Pedemonte, N. and Galietta, L. J. V. (2014) 'Structure and function of tmem16 proteins (anoctamins)', *Physiological Reviews*, 94(2), pp. 419–459. doi: 10.1152/physrev.00039.2011.

Pietra, G. *et al.* (2016) 'The Ca2+-activated Cl- channel TMEM16B regulates action potential firing and axonal targeting in olfactory sensory neurons', *Journal of General Physiology*, 148(4), pp. 1–19. doi: 10.1085/jgp.201611622.

Pifferi, S., Boccaccio, A. and Menini, A. (2006) 'Cyclic nucleotide-gated ion channels in sensory transduction', *FEBS Letters*, 580(12), pp. 2853–2859. doi: 10.1016/j.febslet.2006.03.086.

Pifferi, S., Dibattista, M. and Menini, A. (2009) 'TMEM16B induces chloride currents activated by calcium in mammalian cells', *Pflugers Archiv European Journal of Physiology*, 458(6), pp. 1023–1038. doi: 10.1007/s00424-009-0684-9.

Pifferi, S., Menini, A., and Kurahashi, T. (2010). Signal Transduction in Vertebrate Olfactory Cilia. In The Neurobiology of Olfaction, A. Menini, ed. (Boca Raton (FL): CRC Press/Taylor & Francis), pp. 203–223.

Pilpel, Y. and Lancet, D. (1999) 'The variable and conserved interfaces of modeled olfactory receptor proteins', *Protein Science*, 8(5), pp. 969–977. doi: 10.1110/ps.8.5.969.

Ponissery Saidu, S. *et al.* (2013) 'Channel properties of the splicing isoforms of the olfactory calcium-activated chloride channel Anoctamin 2', *Journal of General Physiology*, 141(6), pp. 691–703. doi: 10.1085/jgp.201210937.

Probst, W. C. *et al.* (1992) 'Sequence Alignment of the G-Protein Coupled Receptor Superfamily', *DNA and Cell Biology*, 11(1), pp. 1–20. doi: 10.1089/dna.1992.11.1.

Rajah, M. M. *et al.* (2021) 'Since January 2020 Elsevier has created a COVID-19 resource centre with free information in English and Mandarin on the novel coronavirus COVID- company ' s public news and information website . Elsevier hereby grants permission to make all its COVID-

19-r', *Journal of Molecular Biology*.

Rash, J. E. *et al.* (2005) 'Ultrastructural localization of connexins (Cx36, Cx43, Cx45), glutamate receptors and aquaporin-4 in rodent olfactory mucosa, olfactory nerve and olfactory bulb', *Journal of Neurocytology*, 34(3–5), pp. 307–341. doi: 10.1007/s11068-005-8360-2.

Reisert, J. *et al.* (2003) 'The Ca-activated Cl channel and its control in rat olfactory receptor neurons', *Journal of General Physiology*, 122(3), pp. 349–363. doi: 10.1085/jgp.200308888.

Reisert, J. *et al.* (2005) 'Mechanism of the excitatory Cl- response in mouse olfactory receptor neurons', *Neuron*, 45(4), pp. 553–561. doi: 10.1016/j.neuron.2005.01.012.

Reisert, J. (2010) 'Origin of basal activity in mammalian olfactory receptor neurons', *Journal of General Physiology*, 136(5), pp. 529–540. doi: 10.1085/jgp.201010528.

Reisert, J. and Matthews, H. R. (1999) 'Adaptation of the odour-induced response in frog olfactory receptor cells', *Journal of Physiology*, 519(3), pp. 801–813. doi: 10.1111/j.1469-7793.1999.0801n.x.

Reisert, J., Yau, K. W. and Margolis, F. L. (2007) 'Olfactory marker protein modulates the cAMP kinetics of the odour-induced response in cilia of mouse olfactory receptor neurons', *Journal of Physiology*, 585(3), pp. 731–740. doi: 10.1113/jphysiol.2007.142471.

Reisert, J. and Zhao, H. (2011) 'Response kinetics of olfactory receptor neurons and the implications in olfactory coding', *Journal of General Physiology*, 138(3), pp. 303–310. doi: 10.1085/jgp.201110645.

Ressler, K. J., Sullivan, S. L. and Buck, L. B. (1993) 'A zonal organization of odorant receptor gene expression in the olfactory epithelium', *Cell*, 73(3), pp. 597–609. doi: 10.1016/0092-8674(93)90145-G.

Reuter, D. *et al.* (1998) 'A depolarizing chloride current contributes to chemoelectrical transduction in olfactory sensory neurons in situ', *Journal of Neuroscience*, 18(17), pp. 6623–6630. doi: 10.1523/jneurosci.18-17-06623.1998.

Rock, J. R. and Harfe, B. D. (2008) 'Expression of TMEM16 paralogs during murine embryogenesis', *Developmental Dynamics*, 237(9), pp. 2566–2574. doi: 10.1002/dvdy.21676.

Ronnett, G. V. and Moon, C. (2002) 'G proteins and olfactory signal transduction', *Annual Review of Physiology*, 64(5), pp. 189–222. doi: 10.1146/annurev.physiol.64.082701.102219.

Ryba, N. J. P. and Tirindelli, R. (1997) 'A new multigene family of putative pheromone receptors', *Neuron*, 19(2), pp. 371–379. doi: 10.1016/S0896-6273(00)80946-0.

Saraiva, L. R. *et al.* (2015) 'Hierarchical deconstruction of mouse olfactory sensory neurons : from whole mucosa to single-cell', *Nature Publishing Group*, (December), pp. 1–17. doi: 10.1038/srep18178.

Schild, D. and Restrepo, D. (1998) 'Transduction mechanisms in vertebrate olfactory receptor cells', *Physiological Reviews*, 78(2), pp. 429–466. doi: 10.1152/physrev.1998.78.2.429.

Schreiber, R. *et al.* (2010) 'Expression and function of epithelial anoctamins', *Journal of Biological Chemistry*, 285(10), pp. 7838–7845. doi: 10.1074/jbc.M109.065367.

Schroeder, B. C. *et al.* (2008) 'Expression Cloning of TMEM16A as a Calcium-Activated Chloride Channel Subunit', *Cell*, 134(6), pp. 1019–1029. doi: 10.1016/j.cell.2008.09.003.

Schwob, J. E. *et al.* (2016) 'Stem and progenitor cells of the mammalian olfactory epithelium: Taking poietic license', *Journal of Comparative Neurology*, 525(4), pp. 1034–1054. doi: 10.1002/cne.24105.

Scott, J. W. and Scott-Johnson, P. E. (2002) 'The electroolfactogram: A review of its history and uses', *Microscopy Research and Technique*, 58(3), pp. 152–160. doi: 10.1002/jemt.10133.

Scudieri, P. *et al.* (2013) 'TMEM16A-TMEM16B chimaeras to investigate the structure-function relationship of calcium-activated chloride channels', *Biochemical Journal*, 452(3), pp. 443–455. doi: 10.1042/BJ20130348.

Song, Y. *et al.* (2008) 'Olfactory CNG Channel Desensitization by Ca2+/CaM via the B1b Subunit Affects Response Termination but Not Sensitivity to Recurring Stimulation', *Neuron*, 58(3), pp. 374–386. doi: 10.1016/j.neuron.2008.02.029.

Stephan, A. B. *et al.* (2009) 'ANO2 is the cilial calcium-activated chloride channel that may mediate olfactory amplification', *Proceedings of the National Academy of Sciences of the United States of America*, 106(28), pp. 11776–11781. doi: 10.1073/pnas.0903304106.

Stephan, A. B. *et al.* (2012) 'The Na + / Ca 2 + exchanger NCKX4 governs termination and adaptation of the mammalian olfactory response', *Nature Neuroscience*, 15(1). doi: 10.1038/nn.2943.

Stöhr, H. *et al.* (2009) 'TMEM16B, a novel protein with calcium-dependent chloride channel

activity, associates with a presynaptic protein complex in photoreceptor terminals', *Journal of Neuroscience*, 29(21), pp. 6809–6811. doi: 10.1523/JNEUROSCI.5546-08.2009.

Sungnak, W. *et al.* (2020) 'SARS-CoV-2 entry factors are highly expressed in nasal epithelial cells together with innate immune genes', 26(May). doi: 10.1038/s41591-020-0868-6.

Suzuki, J. *et al.* (2010) 'Calcium-dependent phospholipid scrambling by TMEM16F', *Nature*, 468(7325), pp. 834–840. doi: 10.1038/nature09583.

Suzuki, J. *et al.* (2013) 'Calcium-dependent phospholipid scramblase activity of TMEM 16 protein family members', *Journal of Biological Chemistry*, 288(19), pp. 13305–13316. doi: 10.1074/jbc.M113.457937.

Suzuki, Y., Takeda, M. and Farbman, A. I. (1996) 'Supporting cells as phagocytes in the olfactory epithelium after bulbectomy', *Journal of Comparative Neurology*, 376(4), pp. 509–517. doi: 10.1002/(SICI)1096-9861(19961223)376:4<509::AID-CNE1>3.0.CO;2-5.

Swaney, W. T. and Keverne, E. B. (2009) 'The evolution of pheromonal communication', 200, pp. 239–247. doi: 10.1016/j.bbr.2008.09.039.

Torre, V. *et al.* (1995) 'in Sensory Receptor Cells CT', *Receptor*, 75(December).

Trudeau, M. C. and Zagotta, W. N. (2003) 'Calcium/calmodulin modulation of olfactory and rod cyclic nucleotide-gated ion channels', *Journal of Biological Chemistry*, 278(21), pp. 18705–18708. doi: 10.1074/jbc.R300001200.

Vassar, R., Ngai, J. and Axel, R. (1993) 'Spatial segregation of odorant receptor expression in the mammalian olfactory epithelium', *Cell*, 74(2), pp. 309–318. doi: 10.1016/0092-8674(93)90422-M.

Vogalis, F., Hegg, C. C. and Lucero, M. T. (2005) 'Electrical coupling in sustentacular cells of the mouse olfactory epithelium', *Journal of Neurophysiology*, 94(2), pp. 1001–1012. doi: 10.1152/jn.01299.2004.

Wachowiak, M. (2011) 'All in a Sniff: Olfaction as a Model for Active Sensing', *Neuron*, 71(6), pp. 962–973. doi: 10.1016/j.neuron.2011.08.030.

Wang, L. *et al.* (2019) 'TMEM16B Calcium-Activated Chloride Channels Regulate Male Mice', *The Journal of Neuroscience*, 39(36), pp. 7102–7117.

Wang, Z. *et al.* (2006) 'Pheromone detection in male mice depends on signaling through the type

3 adenylyl cyclase in the main olfactory epithelium', *Journal of Neuroscience*, 26(28), pp. 7375–7379. doi: 10.1523/JNEUROSCI.1967-06.2006.

Weiss, S. R. (2020) 'Forty years with coronaviruses', *Journal of Experimental Medicine*, 217(5), pp. 2–5. doi: 10.1084/jem.20200537.

Wu, A. *et al.* (2020) 'Genome Composition and Divergence of the Novel Coronavirus (2019-nCoV) Originating in China', *Cell Host and Microbe*, 27(3), pp. 325–328. doi: 10.1016/j.chom.2020.02.001.

Wyatt, T. D. (2014) *Pheromones and Animal Behavior: Chemical Signals and Signature Mixes.* doi: 10.1109/Allerton.2013.6736599.

Xiao, Q., . *et al.* (2011) 'Voltage- and calcium-dependent gating of TMEM16A/Ano1 chloride channels are physically coupled by the first intracellular loop'. Proc. Natl. Acad. Sci. U. S. A. 108, 8891–8896.

Yan, C. *et al.* (1995) 'Molecular cloning and characterization of a calmodulin-dependent phosphodiesterase enriched in olfactory sensory neurons', 92(October), pp. 9677–9681.

Yang, Y. D. *et al.* (2008) 'TMEM16A confers receptor-activated calcium-dependent chloride conductance', 455(October), pp. 2–8. doi: 10.1038/nature07313.

Yoon, H., Enquist, L. W. and Dulac, C. (2005) 'Olfactory inputs to hypothalamic neurons controlling reproduction and fertility', *Cell*, 123(4), pp. 669–682. doi: 10.1016/j.cell.2005.08.039.

Yu, C. R. *et al.* (2004) 'Spontaneous Neural Activity Is Required for the Establishment and Maintenance of the Olfactory Sensory Map', *Neuron*, 42, pp. 553–566.

Di Zanni, E. *et al.* (2018) 'Gain of function of TMEM16E/ANO5 scrambling activity caused by a mutation associated with gnathodiaphyseal dysplasia', *Cellular and Molecular Life Sciences*, 75(9), pp. 1657–1670. doi: 10.1007/s00018-017-2704-9.

Zhang, X. and Firestein, S. (2002) 'The olfactory receptor gene superfamily of the mouse', *Nature Neuroscience*, 5(2), pp. 124–133. doi: 10.1038/nn800.

Zhang, Y. *et al.* (2017) 'Inferior Olivary TMEM16B Mediates Cerebellar Motor Learning', *Neuron*, 95(5), pp. 1103-1111.e4. doi: 10.1016/j.neuron.2017.08.010.

Zhang, Z. *et al.* (2021) 'SARS-CoV-2 spike protein dictates syncytium-mediated lymphocyte elimination', *Cell Death and Differentiation*, 28(9), pp. 2765–2777. doi: 10.1038/s41418-021-

00782-3.

Zhao, H. *et al.* (1998) 'Functional Expression of a Mammalian Odorant Receptor', 279(5348), pp. 237–242.

Zheng, J. and Zagotta, W. N. (2004) 'Stoichiometry and assembly of olfactory cyclic nucleotide-gated channels', *Neuron*, 42(3), pp. 411–421. doi: 10.1016/S0896-6273(04)00253-3.

Ziegler, C. G. K. *et al.* (2020) 'Article SARS-CoV-2 Receptor ACE2 Is an Interferon- Stimulated Gene in Human Airway Epithelial Cells and Is Detected in Specific Cell Subsets across Tissues SARS-CoV-2 Receptor ACE2 Is an Interferon- Stimulated Gene in Human Airway Epithelial Cells and Is ', pp. 1016–1035. doi: 10.1016/j.cell.2020.04.035.

Zou, X. *et al.* (2020) 'Single Cell RNA-seq Data Analysis Reveals the Potential Risk of SARS-CoV-2 Infection Among Different Respiratory System Conditions', 11(August), pp. 1–9. doi: 10.3389/fgene.2020.00942.

Zufall, F., Shepherd, G.M., and Firestein, S. (1991). 'Inhibition of the olfactory cyclic nucleotide gated ion channel by intracellular calcium'. Proc. R. Soc. Lond. B Biol. Sci. 246, 225–230.

Zufall, F. and Leinders-zufall, T. (1997) 'Identification of a Long-Lasting Form of Odor Adaptation that Depends on the Carbon Monoxide / cGMP Second- Messenger System', 17(8), pp. 2703–2712.

Zufall, F. and Leinders-Zufall, T. (2000) 'The cellular and molecular basis of odor adaptation', *Chemical Senses*, 25(4), pp. 473–481. doi: 10.1093/chemse/25.4.473.